Theory and Experimental Verification of the Longitudinal Instability of Cooled Coasting Beams at the Heavy Ion Storage Ring ESR

Inaugural-Dissertation
zur Erlangung des academischen Grades eines
Doktors der Naturwissenschaften

vorgelegt beim Dipartimento di Ingegneria Elettrica,
Università di Napoli Federico II

and

durchgeführt an der
Gesellschaft für Schwerionenforschung mbH, Darmstadt

von

Giovanni Rumolo

November
1999

Supervisors: Prof. Giovanni Miano
Prof. Dr. Ingo Hofmann

Contents

Introduction

The present interest in longitudinal and transverse instabilities of space charge dominated particle beams in synchrotrons and storage rings has been strongly stimulated by the **heavy ion fusion research project**, and the growing attention toward different high-current beams applications. The proposal of a European Study Group on an Ignition Facility [1, 2] is based on the large potential of high current accelerators for energy production [3]. Along with this proposal, a parallel development of driver design and beam dynamics experiments and computer simulation have become a crucial issue. The SIS/ESR (SchwerIonenSynchrotron/Experimentier-SpeicherRing – Heavy Ion Synchrotron/Experi-mental Storage Ring) facility at the **Gesellschaft für Schwerionenforschung (GSI-Darmstadt)** has proved to be a suitable tool to carry out such "accelerator tests": in particular, important progress has been possible with cooled high longitudinal phase space density beams in the ESR [2].

The issue of collective instabilities directly relates to the development of high current storage rings in a heavy ion fusion driver [4]. During storage of a coasting beam for several milliseconds, there is the concern that currents exceeding the "Keil-Schnell circle threshold" by a large factor might be subject to the longitudinal instability. The mechanism of this phenomenon can be qualitatively explained as a resonant interaction of the beam particles among themselves and with the surrounding environment [5, 6]. In fact, beam particles interact via the direct space charge field – as it is also possibly modified by the finite conductivity of the walls of the vacuum chamber – and through the electromagnetic fields induced in the environment surrounding the beam. When a small coherent (or even incoherent) disturbance occurs in the beam structure, longitudinal and transverse electromagnetic fields are induced, which will perturb the particles trajectories through the Lorentz force. In the highly relativistic case, these fields sensibly trail behind the "source" particles, and this explains the name of "wake fields" [7]. The fields, and in turn the beam perturbation, can self-amplify each other, such that an instability occurs resulting into beam degradation and loss.
The beam environment not only consists of a smooth stainless steel vacuum pipe, but also comprises ceramic and ferrite structures built inside the vacuum chamber, along with some other elements or irregularities such as clearing electrodes, bellows, pipe discontinuities, etc. These complex geometrical wall configurations with different material properties are responsible for generating non-uniform fields which can all contribute to the coherent beam instability.
The longitudinally unstable evolution of a beam can be seen and monitored by a pick-up as a modulation in the beam current profile, whose amplitude grows exponentially in time and comes to saturation after a few e-folding times. One of the most undesired effects of the longitudinal instability is the increase of the beam momentum spread, which according to the special application may reach up to an unacceptable level. For example, in drivers for heavy ion inertial fusion, beams with very small momentum spread are needed for the

final focusing.
One of the challenging questions in beam physics is whether a high-current machine must necessarily operate under conditions where the beam is linearly stable, or it might instead operate with a linearly unstable beam provided that either the instability saturates with an acceptable distortion in the beam distribution function or the residence time is short enough to limit the blow-up induced by the instability. Thus an understanding of nonlinear effects due to space charge, which arise after the initial perturbation has grown outside the range of validity of linear, small-amplitude analysis, is fundamental in the development of high power beam sources.
Beam instabilities were encountered early in the history of accelerators and colliders. It was noted that, beyond certain beam density thresholds, the space charge tends to blow up, and to degrade the beam. Nevertheless, so far there had been no experimental evidence of the occurrence of longitudinal instabilities in space charge dominated beams below transition energy, with low γ. Though the theory of instabilities is well established, the validity of the perturbative linear theory in this special case was never checked in further detail. The ISR (Intersecting Storage Ring) experiments on the longitudinal instability driven by an RF cavity were performed at relativistic energies [8] and compared with numerical simulation [9]. As space charge was negligible at those energies, the connected findings are not directly applicable to the situation in heavy ion fusion. Another experiment was done with protons at the energy of 70 MeV/u [10]: observation of microwave signals during stripping injection into the ISIS synchrotron gave evidence of some growth of an initial (linac) modulation, but no quantitative analysis of the effect was possible. Cooler rings experiments had shown that currents can exceed the "circle criterion" by a factor as large as 10, yet with the friction effect of the electron cooling continuously present [11].
A first cycle of dedicated measurements in order to excite longitudinal instabilities on a coasting beam has been carried out at the ESR – as the measurements that will be described and interpreted in this work. There it was possible to clearly observe the beam going unstable on the second harmonic under the effect of its interaction with a cavity tuned on the multiple $n = 2$ of its revolution frequency [2]. But still, no quantitative analysis was possible because of the lack of precise information about the cavity eigenfrequency during the measurements.
An alternative study of the space charge dominated regime entirely in time domain has recently been undertaken in a linear electron channel with resistive walls [12]. This experiment has confirmed the growth rate for the unstable slow wave and the damping rate for the stable fast wave obtained from the linear cold fluid theory. The fully developed nonlinear stages of the instability have been less extensively investigated up to the present study. Saturation, decoherence effects, and energy-spread overshoot have been predicted by simulating numerically a high energy coasting beam interacting with a resonant RF cavity in the absence of space charge effects [9].

This PhD work essentially reports about the latest cycle of measurements made at the ESR, aiming at proving and interpreting the longitudinal instability of intense and electron cooled ion coasting beams below transition, which interact with a narrow-band impedance (in our case, a slightly detuned cavity). The main ideas, and novelties with respect to all the experiments previously done on the same subject, have been:

- to excite the longitudinal instability on a space charge dominated beam (intense and cooled down to a very low momentum spread via electron cooling) by means of an RF cavity inside a storage ring (the ESR was our tool for the investigation of this issue);

- to dispose of a precise control of the cavity eigenfrequency, such that it was always possible to know how big a cavity impedance was acting on the beam at the different stages, and consequently how quick an instability should have been expected out of such an impedance. Unfortunately, this option needed an active feedback control through a small external voltage oscillating in the cavity, which had to be taken into account for a correct interpretation of the results of the measurements.

The experimental environment of GSI, in which the measurements have taken place, and the project of a heavy ion inertial fusion driver, which has basically triggered this renewed enthusiasm towards the question of beam instabilities, are widely described in **Chapter 1**. High intensity operation of the SIS and ESR is unanimously recognized as a common goal for the GSI experimental program in general, and a heavy ion fusion program in particular. Therefore a careful investigation of the possible drawbacks that arise when dealing with high currents becomes a crucial point for successful further machines development.

Chapter 2 contains the full revised linear theory of longitudinal instabilities for coasting beams. The longitudinal coupling impedance is introduced in order to model the interaction between beam and surrounding environment. By using the impedance formalism the kinetic equation is solved with a perturbative approach starting from a coasting beam equilibrium. Stability criteria in the impedance plane are given for some momentum distribution functions of the beam.

After having laid the basis for an understanding of the phenomena connected with an unstable interaction beam-beam-cavity in the ESR, in **Chapter 3** the experiment is presented, and the data acquisition is discussed. All experimental observations are carefully noted, both those related to the linear phase of the instability, which are completely explained by means of the small-amplitude analytical theory, and those characteristic of the nonlinear phase that require further investigation.

Chapter 4 contains a full comparison between theory, experiment and computer simulations for the linear phase of the instability dynamics. The rise times extrapolated from each of these three approaches are confronted, and found out to be in very good agreement. In particular, the problem of the finite voltage at the cavity gap, which was present as the ESR measurements were carried out, is addressed from the theoretical point of view, and implemented numerically.

In the early stage of the instability, the beam behaves as a non-neutral plasma and its dynamics can be therefore described using a fluid approach. Such a model, which can explain phenomena like wave steepening and production of higher harmonics, is developed in **Chapter 5**. The description starts from the Vlasov equation for the longitudinal dynamics already used in Chapter 3, and integrates it in the velocity space with the classical method of the distribution function moments. The fluid model is of course applied to the ESR measurements, so that comparisons between the results obtained from the different approaches (fluid, kinetic, and particle-in-cell simulations with the PATRIC code) and the data observed at the ESR may be drawn. These comparisons make clear how far the proposed macroscopic model provides a correct description of the beam dynamics and what nonlinear effects it can thoroughly explain.

Chapter 6 casts a first attempt insight into the late stage of a longitudinally unstable evolution, where nonlinear resonant particle-wave interactions become important. By making use of numerical simulations based on a Fokker-Planck direct integrator, the influence of electron cooling and space charge are discussed, as well as the evolution of the momentum spread is calculated. A general view on the long term dynamics of the longitudinal distribution function of an intense particle beam which is subject to a cavity driven instability is qualitatively discussed (with and without space charge, with and without electron cooling).

The longitudinal stability of an ion beam that undergoes laser cooling has become of great interest since the proposal for a heavy ion fusion driver has been presented, because the option of using this unconventional technique, which would improve the beam quality to meet the final focusing requirements, appears promising. When applying laser cooling to high current beams, though, one has to pay attention because the beam distribution function gets strongly deformed during the process of cooling, and this might give rise to instabilities of the type two-streams. A kinetic modeling of an ion beam undergoing laser cooling is presented in **Chapter 7**. Furthermore, the stability of such a beam is also studied by means of a quasi-linear approach. Eventually, the implementation of laser cooling in the codes for the longitudinal dynamics is explained and employed to check the small-amplitude analysis as well as to simulate the high-current laser cooling experiment planned at the ESR.

In summary, the present work relates about experimental and theoretical investigation on electron-cooled coasting beams – with the issues connected to the actual measurement techniques, as well – and moves the first steps into the stability study of a laser cooled beam as promising option to be used in the design of a heavy ion fusion driver.

Chapter 1

High current beam studies and heavy ion inertial fusion

Thermonuclear fusion of hydrogen isotopes to helium appears to be a sufficiently clean and abundant long-term energy source of mankind. The climatic effects of CO_2 as recognized to-day, have led many Governmental Authorities to envisage the replacement of fossil fuel by new energy sources, this quite apart from the limitation of existing reserves.
Since the beginning of heavy ion inertial fusion research at GSI (Gesellschaft für Schwerionenforschung - Institute for the Research on Heavy Ions) in the early 80's, it has been clear that its challenging accelerator issues would have much in common with the high-current development of the future GSI accelerator facility. In heavy ion fusion the aim has been set to achieve the necessary beam power for the heaviest ions to ignite fusion pellets with DT fuel for energy production. For this ambitious long-term goal and the more near-term GSI development, mutual benefit is expected from the fact that in both cases basically non-relativistic energy beams are needed, for which space charge effects play an important role with respect to intensity thresholds and effective control of phase space dilution. Furthermore, it is also clear that the operating experience of already existing high-intensity synchrotrons would be an essential learning platform (though not sufficient) to answer the issues of a heavy ion fusion driver – nearly lossless ring injection under space charge conditions, control of longitudinal and/or transverse instabilities, crossing of resonances by space charge, RF bunching and final focusing, adequate diagnostics tools.
High intensity operation of the SIS (SchwerIonenSynchrotron) and ESR (ExperimentierSpeicherRing) is unanimously recognized as a common goal for the GSI experimental program in general, and a heavy ion fusion program - at modest scale - in particular. The latter would be composed of:

- **Plasma physics target experiments** with cylindrical targets to be heated to temperatures between 10 and 50 eV by means of the highest possible beam intensities or phase space densities available from the SIS/ESR. In the Inertial Fusion Program, this activity essentially addresses questions connected with the converters and the beam-target interface.

- **Beam physics experiments** in the SIS and ESR to obtain an adequate understanding of instabilities and space charge induced resonances, and assist in identifying appropriate measures for their control.

- **Development of computer simulation** to interpret measurements and allow extrapolations to future parameters. Particle-in-cell codes (both transverse and longitudinal dynamics), direct integrators of the kinetic equations on a phase space grid, and a map-based 2-dimensional code for the transverse plane have been developed and applied to different issues related to the beam evolution in space charge dominated regime.

1.1 The experimental environment

The GSI operates a quite complex accelerator structure for heavy ions, which consists of the linear accelerator UNILAC (UNIversal Linear ACcelerator), the synchrotron for heavy ions SIS, and the experimental storage ring ESR. As the knowledge of the experimental environment is indispensable for the understanding of accelerator physics experiments, in this section we will essentially describe the accelerator facility, and we will lay the stress on some among its special features. The measurements presented in this work have been carried out at the ESR. Hence, a more detailed description of the ESR will be given in the following, with its most important properties and technical parameters, insofar as they will be needed for a full comprehension of this work.

1.1.1 Accelerator facilities at GSI

Since 1975 GSI has been operating an accelerator facility for ions having masses spanning between ^{4}He and ^{238}U. The heavy ions synchrotron SIS and the experimental storage ring ESR have been put into operation since 1990 as a first upgrade of the structure. Fig. 1.1 shows a global overview of the accelerator facility of GSI.

The ions that must be accelerated are produced first in one of the ion sources (Penning, Chordis, or Mevva depending upon the desired ion species) from one of the two injectors. After a first bending section for charge and mass separation, the ions are injected into the UNILAC. The first part of the UNILAC consists now of a new 36 MHz high current injector (made up of RFQ's - Radio Frequency Quadrupoles), which should be able to produce an accelerating voltage 2.5 times stronger than the one formerly obtained with the Wideroe structures on the same path length. The energy of the ions at the end of this section must be $\sim$ 1.4 MeV/u, before they get further ionized through a stripping foil. The advantages of the new high current injector with respect to the former Wideroe structure are essentially:

- More particles can be accelerated through this section because lower charge state ions can be brought up to the desired energy level, being the accelerating voltage up to 2.5 times bigger (the ion sources always produce lower charge state ions in larger amounts);
- Any space charge inconvenience across this section is limited thanks to the lower charge state of the transported ions, in spite of their higher number.

The pre-accelerated ions will be then converted to a higher charge state by means of a stripping foil, and subsequently injected into the following Alvarez-accelerator, which works at a frequency of 108 MHz (4$\times$27 MHz). The final energy of the UNILAC is normally 11.4 MeV/u, but it may as well be differently set by simply choosing a different phase relation between the fields oscillating in subsequent HF-cavities. After 110 m acceleration, the beam is according to necessity injected into one of the three low energy experimental areas, or it is bent into the transfer channel towards the Schwer-Ionen-Synchrotron SIS.

The linear accelerator UNILAC works as injector machine for the heavy ion synchrotron SIS (circumference 217 m, energies reached up to 2.1 GeV/u for ions with $Q/A = 0.5$).

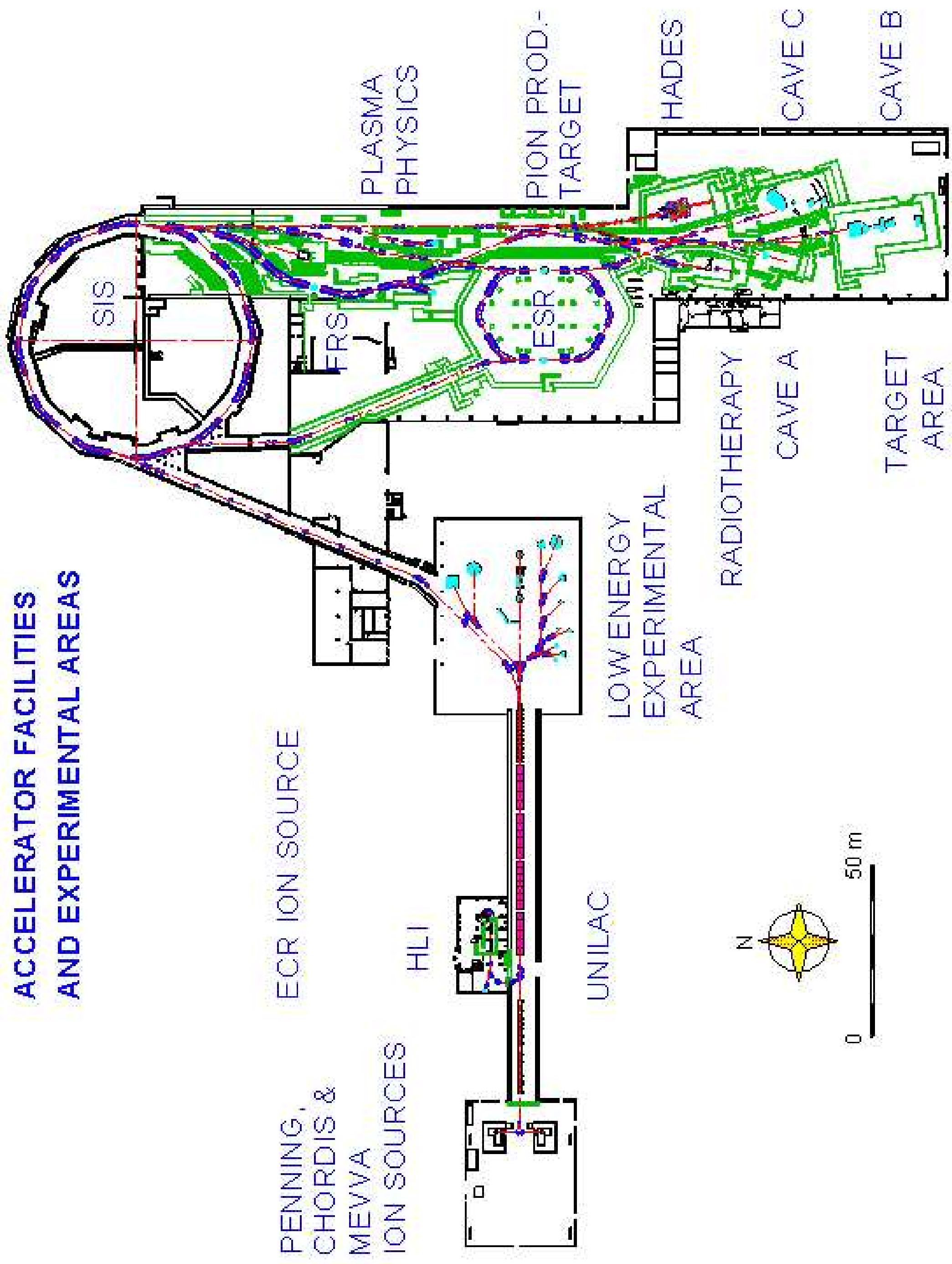

Figure 1.1: Global overview on the GSI accelerator complex.

In fact, the ions that have reached the energy level of 11.4 MeV/u either are shot into the SIS over one single revolution (single-turn injection), or they get accumulated therein over several revolutions (multi-turn injection). The injection energy is sufficient to get the light ions (up to Z$\simeq$ 28) fully stripped by means of a "Stripping Target" situated before the injection point; heavier ions are not completely ionized at this stage. In the SIS the ions are eventually accelerated to the beam energies which are required for the respective experiment. The magnetic rigidity of the SIS is $B\rho = 18$ Tm, and thus the maximum energy that can be reached is limited to 2.1 GeV/u for lighter particles, whereas it strongly depends upon ion mass and its charge state for heavier not fully ionized particles (for instance, 1 GeV/u can be reached for U^{73+}).

After acceleration and extraction from the SIS, it is possible to finally guide the beam to one of the different experimental areas, or inject it into the storage ring ESR, or send it to the treatment area for the heavy ion therapy for cancers [13]. According to the application, the beam can be extracted from the SIS either quickly (within one revolution), or slowly (over some seconds). There exist two possibilities of beam transfer from the SIS to the ESR or to the experimental areas: either the beam goes directly, or it is guided through the fragment separator FRS [14]. There the fragments coming from a production target can be selected according to their masses or charges, in order to produce in this way beams of exotic particles. Along the line which connects the SIS to the ESR, one more Cu Stripping-Target of medium thickness (0.01 to 0.1 g/cm^2) is also installed, which is able to strip off all the electrons even from heavier ion sorts if the energy of the beam is high enough.

In the ESR [15], ions suitable for experiments in the fields of atomic or nuclear physics, as well as for beam physics measurements and observations, can be stored for quite long times. Besides an electron cooler, a Gas-Jet-Target and a Nd:YAG-laser beam are also available there. Details about the ESR and its characteristics will be given in the next subsection 2.1.2. After being stored in the ESR, the beam can eventually be re-injected from the ESR to SIS for further acceleration, or it might as well ejected and directed to the experimental areas.

1.1.2 The Experimental Heavy Ion Storage Ring ESR

The layout of the ESR with its major components is shown schematically in Fig. 1.2 and the most important ring parameters are listed in Table 2.1. With respect to detailed information on design considerations and technical parameters described in Ref. [16], only a brief overview on characteristic features of the ESR is given here:

- The maximum *magnetic bending power of* $B \times \rho = 10$ Tm makes the ESR capable to accept fully stripped uranium ions at a maximum *specific ion energy of* 560 MeV/u. At present, the beam energy is limited for electron-cooled ion beams to values $\leq$ 400 MeV/u, because the maximum accelerating voltage at the electron cooler is restricted to about 210 keV.

- The *large momentum acceptance* $(\Delta p/p)_{\max}$ *of about 2.5%* (in the usual ion optical mode) makes the ring well suited for beam accumulation by applying the RF-stacking technique [17] as well as for accepting multi-component beams containing ions of rather different magnetic stiffness [17] – very useful for Schottky mass spectrometry [18].

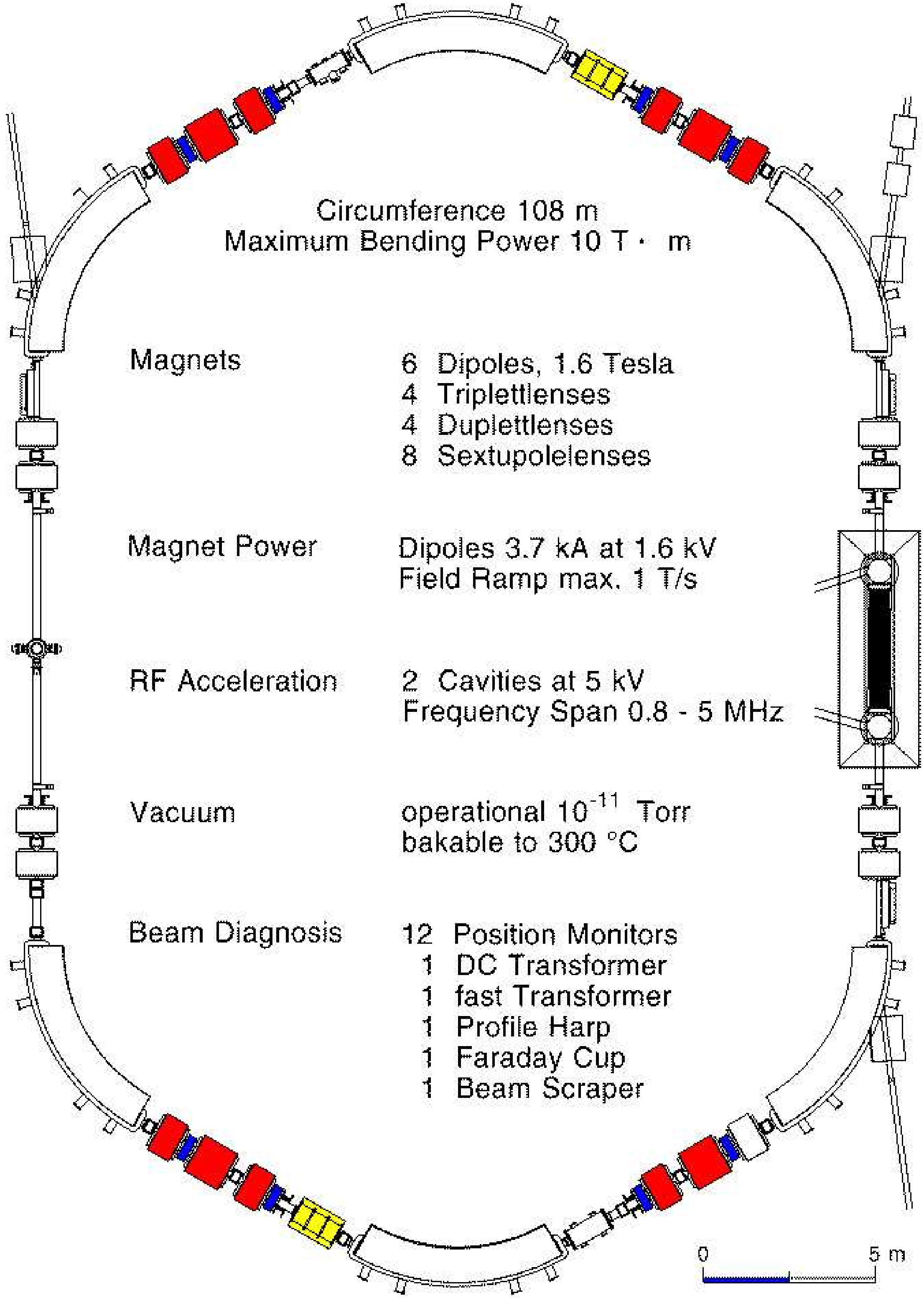

Figure 1.2: Overview of the heavy ion storage ring ESR and list of its main components.

Circumference	108.36 m
Magnetic rigidity	0.5 – 10 Tm
Ion species	C^{+6} to U^{92+}, radioactive beams
Energy range	3.0 – 560 MeV/u for U^{92+}
	3.0 – 840 MeV/u for ions with $Q/A = 0.5$
Maximum beam current	20 mA
Horizontal betatron tune	$Q_x \simeq 2.31$
Vertical betatron tune	$Q_y \simeq 2.30$
Transition point	$\gamma_t \simeq 2.7$
Full momentum acceptance	$(\Delta p/p_0)_{\max} \approx 2.5\%$
Bending magnets:	
Number × angle	6×60^o
Bending radius	6.25 m
Used aperture ($h \times v$)	220×70 mm^2
Quadrupole magnets:	
Families × no.	10×2
Field gradient	0.31 – 6.1 T/m
Used aperture ($h \times v$)	300×120 mm^2
Sextupoles (families × no.)	2×4
Working pressure in the pipe	5×10^{-11} mbar

Table 1.1: Overview on technical and physical parameters for the ESR.

- *Large transverse acceptances* in connection with the large $(\Delta p/p)_{\max}$ are, in addition, helpful for efficient injection and storage of "hot" secondary beams of nuclear fragments delivered by the FRS.

- *Electron cooling* is routinely applied at the ESR [19] for beam cooling in the longitudinal as well as transverse directions. Because the electron cooling time amounts to up to several minutes for "hot" fragment beams delivered by the FRS, additional *stochastic pre-cooling* is foreseen to speed up the cooling. Commissioning of the stochastic cooling system has recently started [21].

- A *supersonic gas jet* of about 4 mm diameter crossing the circulating ion beam in vertical direction is applied as *internal target* [22]. At maximum jet density of approximately 1×10^{13} cm^{-3} luminosity values between 10^{27} cm^{-2} s^{-1} for secondary (fragment) beams and 10^{30} cm^{-2}s^{-1} can be attained. The internal target was used for example in the experiments described in Ref. [18] to produce projectile-near nuclear fragments by projectile-fragmentation reactions.

- The average *ultra-high vacuum pressure is typically* 5×10^{-11} mbar (without internal target operation). *Beam life-times of up to several hours* are achieved, depending on the charge state of the stored ions and the electron cooler current. The beam loss rates are determined by radiative recombination between ions and cooler electrons rather than by interaction with residual gas atoms.

- Extremely *sensitive non-destructive beam diagnostics* is available with Schottky diagnosis and BTF (Beam Transfer Function) measurements. The ESR Schottky diagnosis system [23] is sensitive to a single stored highly charged ion.

The ESR is arranged as a doubly mirror symmetric stretched hexagon with a design circumference of 108.36 m, half the circumference of the SIS. The two long straight sections are provided for electron cooling – possibly laser cooling – and internal experiments around the internal target apparatus. The *six 60°-bending magnets* are fed in series by a single power supply. The bending field can be varied by 1 T/s from 0.08 T at 170 A excitation current to 1.6 T at 3600 A. The beam focusing is performed by *20 quadrupole magnets* arranged in *4 triplets* (two in either of the arcs) and *4 doublets* (two in either of the two long straight sections). Highly flexible ion optics is achieved by means of 10 independently controlled quadrupole power supplies. In terms of synchrotron lattice parameters, the ring may be operated either far below transition (i.e. $\gamma_{\mathrm{t}} < \gamma$) with maximum momentum acceptance, or at $\gamma_{\mathrm{t}} = \gamma$ with essentially reduced $(\Delta p/p)_{\mathrm{max}}$. As we can see from Fig. 1.2, the ESR has two cavities that can be used for beam bunching. These are cavities loaded with ferrite, such as to be able to sustain even relatively low frequency fields for the beam bunching at low harmonic numbers. The presence of the cavities is fundamental for the understanding of our work, since they can be source of passive interaction with the circulating beam, and they may cause instabilities. In the ordinary ESR operation, one of the two cavities is constantly kept short circuited, whereas only the other one is constantly used for bunching purposes: indeed, for a more detailed study of the self-bunching too, as follows in the next chapters of this work, just the effect of one cavity has been used.

1.2 Possible scenario for the GSI upgrade

In this section we discuss the accelerator development which is integrated into an overall high-intensity upgrade of the GSI accelerator complex.
The requirements of the proposed accelerators for plasma physics and the long-term goal of inertial fusion have been defined as:

1. An increase by at least one order of magnitude in the specific power deposition in a plasma target above the 1-2 TW/g. This would lead to a significant increase of the plasma temperature with large volumes (mm-size) heated by heavy ions. The expected temperatures in the 50 eV region would open an interesting regime of plasma physics dominated by hydrodynamics and dense plasma effects. Radiation physics gradually comes into play between 50 and 100 eV, with efficient transfer into radiation occurring for temperatures above 100 eV.

2. A milestone in the development of an accelerator on the path towards inertial fusion application, capable of producing bunched beams of several tens of kJ energy. As a comparison, the HIDIF-study of an ignition facility (see next section) has considered 144 bunches of 20 kJ energy per bunch stored in a set of storage/accumulator rings [4].

The study of hot dense matter generated by heavy ion beams is an alternative to laser produced plasmas with application to the field of basic science (properties of dense ionized matter, strongly coupled plasmas, astrophysical applications) as well as inertial confinement fusion. A characteristic of heavy ion heating is the volume energy deposition in matter of solid density, whereas lasers predominantly deposit their energy on the surface up to the critical energy. It is believed that this specific feature lends itself to quite different experimental conditions and ranges of parameters which warrant extra investments and efforts in the context of the GSI future plans. The physics program should address the following issues:

- Interaction of heavy ions with dense plasmas including stopping and atomic physics issues.
- Elementary processes in plasmas (with astrophysical applications), such as high pressure physics, phase transitions, hydrodynamics, equation of state and opacity measurements.
- Inertial fusion related questions connected with converters and beam-target interface.

It is evident that high current beams need producing and storing in circular machines before they can be focused onto a target. This need naturally raises all the issues connected with the storage of high currents in rings (see next section).
As option for the next-facility, we shall briefly discuss here a high rep-rate booster plus accumulator/cooler ring (AR) (Fig. 1.3). In this option a high charge state ion beam is assumed and accelerated in the rapid cycling booster synchrotron (this could be the SIS speeded up to 1 Hz). In order to achieve a performance better than that of the SIS, it is clearly necessary to have some kind of stacking procedure in the following accumulator/cooler ring, which avoids the usual phase space dilution. The following possibilities are considered:

- A non-Liouvillian stacking of 5-10 batches from the booster into the AR using foil stripping of Xe^{47+} at 1.1 GeV/u [24]; a similar procedure has recently been proposed for the TWAC-project at ITEP assuming 1000-turn stacking over 15 min [25]. Careful optimization of the ion (charge state, mass) with respect to foil interaction and foil heating needs to be done, but preliminary calculations look promising.
- A barrier bucket stacking of 5–10 batches of U^{28+} (limited by intensity and life time effects) from the booster, and removing the phase space dilution by electron cooling; this requires experimental verification of electron cooling at intensities as high as 10^{12}.

In the first case the necessary linac current with the new high-current injector can be expected to be 14 emA of Xe^{47+} (with 8 pmA of Xe^{2+} from a Cordis-source, stripped to 1.2 pmA at 1.4 MeV/u and to 0.3 pmA at 11 MeV/u). This is stacked at 11 MeV/u (10$\times$ multiturn, already reaching the space charge limit) into the synchrotron (assumed with radius 35 m). The resulting 9.1×10^{10} ions would be accelerated to 1100 MeV/u and merged into a single bunch of 2.1 kJ. For a bunching factor $B_{\mathrm{f}} = 0.4$ the resulting tune shift is 0.017. If 10 such batches can be stacked by foil stripping in the AR, the tune shift of the final Xe^{54+} bunch adopts the value $\Delta Q_{\mathrm{h,v}} \approx 0.22$. For the non-Liouvillian action in the AR it would be preferable to have as high as possible a rep-rate for the booster synchrotron in order to avoid phase space blow-up (by space charge effects) during the accumulation process. For a rep-rate of 16 Hz the stacking of 10 batches would require 0.6 sec, which appears reasonable for the estimated tune shift $\Delta Q_{\mathrm{h,v}} \approx 0.22$ at the end of the stacking process. The final compression from 500 ns (after stacking) to 35 ns pulse length would, however, lead to a significant space charge effect, which needs further detailed study in order to check the realistically attainable compression.
The critical issues that need investigating are essentially connected with the foil heating

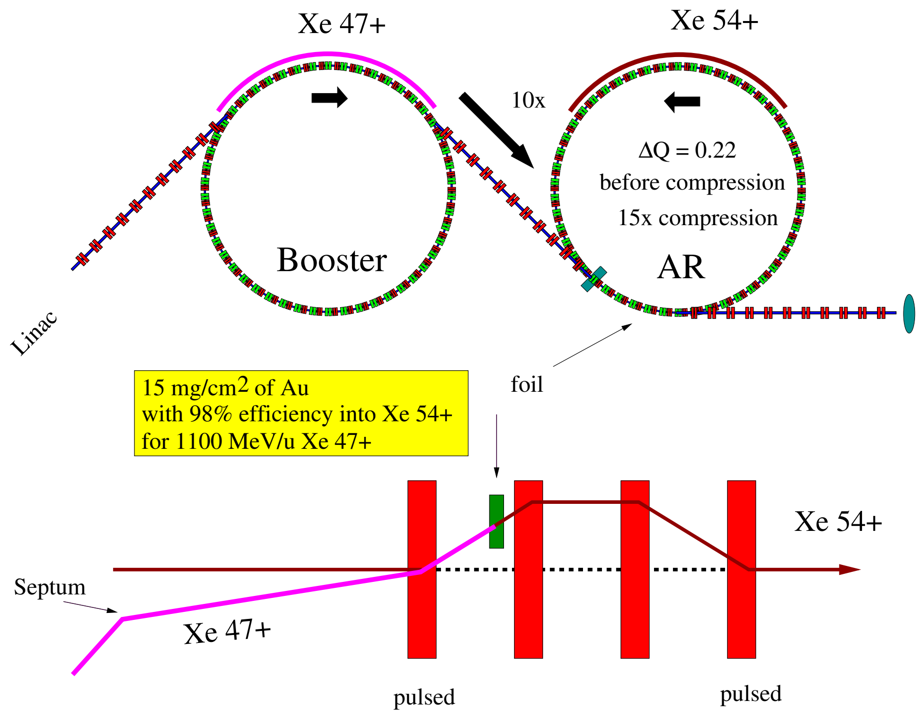

Figure 1.3: Schematic view of non-Liouvillian foil stacking with electron cooling stacking option.

(since the desired large specific energy deposition in the target means high energy deposition in the foil, as well), and with the beam intensity correlated degradation of emittance and momentum spread over the stacking process (due to space charge and intra-beam scattering).

1.3 Heavy ion driven ignition facility

In energy strategies for the next century considered in a global frame (Rio 1992) and within the European Community (Decision by the Council of Ministers for Energy and Environment, 1990), a stabilization or, if possible, a decrease of CO_2 pollution is foreseen. However, both the potential of energy savings and the replacement potential by renewable non-fossil energies are limited.

Research on controlled fusion, initiated already in the fifties, has followed two distinct approaches, that is a quasi-continuous process where the required plasma is confined by strong magnetic fields, *Magnetic Confinement Fusion*, and a process based upon successive micro-explosions where the necessary conditions are created in the implosion of a hydrogen filled pellet triggered by high power irradiation, *Inertial Confinement Fusion*. Both laser and particle beams can be used to explore the physics of inertial confinement fusion. With respect to energy production in a reactor, there is a world-wide consensus to-day that energetic heavy ion beams are a most promising solution to the driver problem. An attractive feature of ICF in general is the separation of driver and fusion reaction chamber. While both approaches to fusion have been investigated world-wide, means and efforts in Europe have gone into the development of large installations for magnetic confinement,

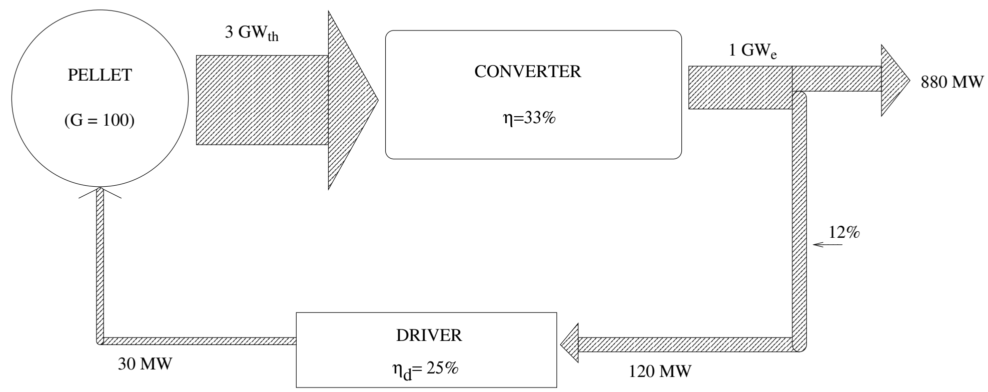

Figure 1.4: Efficiency consideration for a heavy ion ICF power plant.

such as Tokamaks and Stellarators. The progress of inertial fusion research was severely impaired by constraints of classification due to the military relevance of pellet implosion and radiation hydrodynamics. It is only since the end of 1993 that substantial parts of pellet physics results are being declassified. Nowadays, the feasibility in principle of both approaches is no longer in doubt, but a comparison of the technical merits and cost aspects of both approaches must be considered before a choice can be made for future fusion power generating plants.
In the period end 1994/early 1995, a number of European laboratories decided to set up a collaboration in the field of Heavy-Ion Driven Inertial Fusion (HIDIF Collaboration - the achronym stands for Heavy Ion Driven Ignition Facility). It is the aim of this interlaboratory "study group" to work out a conceptual design for an inertial fusion "Ignition Facility", where beams of single-charge heavy ions (typically $A = 200$) would be used to investigate target high temperature plasma physics, and eventually drive DT pellets to low-gain fusion burn. It is worth noting that the accelerator issues of HIDIF have a considerable overlap with the high current issues of the GSI facility (GSI is the coordinating member of the collaboration).

1.3.1 Basic Principles

Installations for ICF consist of three basic constituents: a *reactor chamber*, in which a pellet with a few milligrams of D-T fuel is ignited; a *driver* providing powerful beams (photons, light or heavy ions) to drive the pellet implosion; a *beam guidance system* linking the driver to the reactor chamber. Energy production by ICF requires the use of targets containing a few milligrams of a deuterium-tritium mixture, which can achieve an energy multiplication (target gain) $G > 10/\eta$, η being the driver efficiency (see Fig. 1.4). In order to achieve the ignition of the DT fuel, we know that according to the Lawson criterion the fusion product $n\tau T$ must approximately equal 5×10^{15} cm^{-3} sec keV (n being the ion density of the hydrogen plasma, τ its confinement time, and T its ion temperature): the implosion of the fuel is necessary in order to get the condition for the ignition satisfied, and thus a good quality of the implosion is needed. In ICF it is customary to measure the quality of confinement by means of the product of the mass density and radius of the burning fuel, ρR. The needed energy gain can be attained by simultaneously achieving central fuel ignition and $\rho R \approx 3$g/cm^2, implying compression of the fuel to about 200–300 g/cm^2, or more than 1000 times the liquid density. Typically,

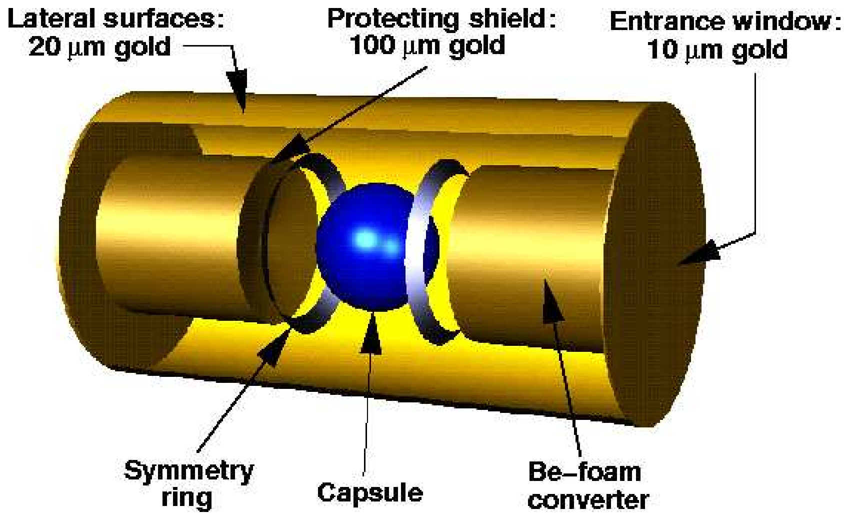

Figure 1.5: Indirectly driven reference target proposed for HIDIF. The heavy ion beams are converted into x-rays by two Be converters. The fusion capsule implosion is driven by the symmetrized radiation (courtesy of R. Ramis).

this requires transferring a specific energy of about 50 kJ/mg to the fuel. As a consequence of implosion symmetry and hydrodynamic stability considerations, the primary approach to heavy ion fusion is indirect drive. This scheme makes use of a target with cylindrical or spherical hohlraum, in which the fusion capsule implosion is driven by the symmetrized radiation (see Fig. 1.5). Extended simulations suggest that an energy gain $G \approx 50$–100 can be achieved by delivering on target E =3–6 MJ of 6-10 GeV heavy ion beams, focused within 6 ns (maximum required pulse length) on two opposite spots with radius $r \approx 1.7$ mm. In the following the two-converter target concept by Ramis has been modified to a high-gain ($G = 100$) version requiring 5 MJ energy and spot radius of 5 mm and pulse length of the main pulse of 10 ns, possibly even slightly longer. A spherical hohlraum with 6 MJ and $G = 78$ was developed by Basko employing a P4 illumination geometry with beams in 4 cones at $\pm 20^o$ and $\pm 60^o$, and a focal spot of 6 mm. Of course, the loosening of the conditions on the focal spot and the final pulse length are extremely important as they determine a lower complexity of the driver that must be used to guide the beamlets to the target. The requirements on the final momentum spread become less stringent. The peak power needed at the target is of the order of 300–500 TW; efficient x-ray production demands specific power deposition $P \approx 10^4$ TW/g in the elements that convert the beam energy into radiation. Attainment of such values of P is the main challenge to the accelerator, and constrains the ion range R, its energy E_0, the particle current I, and the focal spot area F according to:

$$P = \frac{E_0 I}{RF} \; . \tag{1.1}$$

The choice of R and F is based on the requirement that transport and focusing of the beams should be possible by conventional quadrupoles and beams propagating in vacuum. This suggests to use the heaviest ions ($A \approx 200$), with a kinetic energy 5–10 GeV ($\beta_0 \approx 0.2$–0.3), which in low-Z matter have a range of $R = 0.04$–0.1 g/cm^2.

Two alternative accelerator concepts for heavy ion fusion are presently under study. In Europe most of the efforts have focused on the RF linac/storage ring approach, which is the basis of the proposal in Ref. [1]. In the United States, the induction linear accelerator is being developed at the Lawrence Berkeley Laboratory [26].

The RF linear accelerator provides the necessary kinetic energy of the ions. The pulse current is raised to the level of kiloamperes by several steps of current multiplication in storage and buncher rings. The transport limits for high currents in vacuum are mostly well understood, and in any case they are still object of theoretical and experimental detailed studies, as the problem of instabilities is in this work. Hence, there is high confidence that after final bunch compression to typically few nanoseconds, a current of 50 kA can still be transported to the reactor chamber over long distances through magnetic focusing channels that maintain the beam quality. A possible scenario for the driver is discussed in the next subsection.

1.3.2 The driver Accelerator Architecture

The HIDIF driver has a number of characteristic features, which are summarized in the following:

- charge state +1 to reduce space charge effects;
- three ions species (for telescoping) are accelerated in the same linac and stored in different rings;
- 16 ion sources of each species;
- four funneling stages for RFQ's and DTL's and one main high-current DTL linac up to 10 GeV, and a total pulse current of 400 mA (optionally IH structure);
- one set of storage rings with super-conducting dipoles;
- simultaneous two-plane multi-turn injection into storage rings to minimize septum losses;
- multi-turn injection into RF barrier buckets;
- after filling of all storage rings, adiabatic pre-bunching within rings;
- final bunch compression (fast) in induction bunchers with multiple beam lines to obtain the required 6 ns pulse length;
- final switch-yard including delay lines and merging of different ion species for telescoping and synchronous arrival at target;
- conventional focusing using super-conducting quadrupoles in matrix array;
- vacuum transport through target chamber.

The envisaged linac peak current of 400 mA and the gaps between different barrier buckets as well as the switching of the linac beam to different storage rings and to different ion species leads to a total pulse duration of 1.5 ms [4], which is also the duration of the RF power cycle. As a result, the average linac current in this period is 192 mA.
The scenario is modular in the sense that the total energy can be upgraded by using further storage rings (requiring a longer beam pulse from the linac) and a larger number

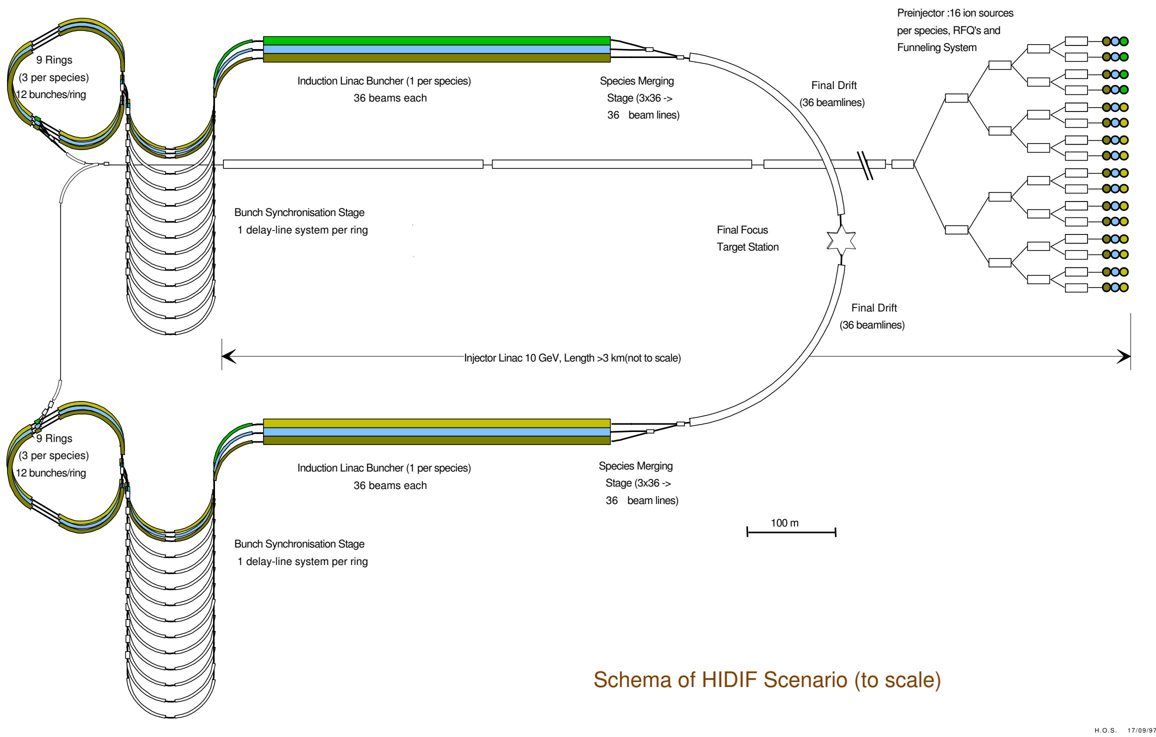

Figure 1.6: HIDIF layout for reference energy of 3 MJ.

of final beam lines. In the present scenario, we assume 12 bunches per storage ring, which is equivalent to a stored energy of 250 kJ per ring.

The full scenario is shown in Fig. 1.6 for the reference case with 3 MJ requiring a total of 12 storage rings. Single-charged ions of three atomic species are accelerated in the same linear accelerator to identical momenta, and stored and bunched in a set of 4 storage rings per species. The bunches are synchronized by delaying them in sets of delay lines (one set per storage ring) so that they coincide per species in time at the entry into the induction bunchers. Each bunch will at this stage travel on a separate trajectory, each induction buncher carrying 24 beam lines in parallel. In the final transport towards the target, one bunch of each of the three species will be deflected into a common beam line. The number of beam lines converging on the reaction vessel is now 48, which is reduced by a factor of three with respect to a single ion species scenario. The length of the final transport is determined by the condition that the bunches impinge on the target with minimum length (fast bunch rotation in longitudinal phase space); the relative timing of the species at ejection from the storage rings must be such that the three species arrive simultaneously at the target.

The issue of space charge makes it necessary to model key issues by means of computer simulations and/or by carrying out experimental investigations and checks on the existing machines. Linac studies for acceleration of beams above 10 MeV/u have been made, showing that the conditions for current, emittance and momentum spread ($\epsilon = 1.2$ mm mrad and $(\Delta p/p_0)_{\mathrm{FWHM}} \leq 0.1\%$) can be satisfied. The problem of the lossless injection of the space charge dominated linac beam into the storage rings with a large factor of current

multiplication (≈ 100) is crucial, and therefore presently investigated. The successive filling of several storage rings requires a debunched beam to be held for 10^2–10^3 revolutions at an intensity where it is normally considered to go unstable due to resonance crossing, or to the ring and space charge impedances. The latter is the issue that is carefully considered throughout this work. Check of the linear theory and interpretation of the nonlinear phase for longitudinally unstable evolutions are given in the next chapters in order to be able to gain a deeper knowledge of this kind of mechanisms and the way they modify the beam structure (their action is anyway never destructive because it does not lead to beam losses but only to a degradation of the beam quality – which might be undesirable or tolerable). Other problem areas concern the final focusing (minimization of geometrical and chromatic aberrations in the lenses for the final transport to the reaction chamber, special care that the beamlets do not feel excessive mutual repulsion due to their low energy), and the target physics as well as the reaction chamber design.
For an Ignition Facility driver, hereafter follows a summarizing list of the issues that need in general addressing:

- Control of phase space dilution and beam loss due to resonances, instabilities or mismatch.
- Alignment, impedance corrections, shaping of phase space distributions and other measures to avoid beam quality reduction below the reactor requirements.
- Effect of dilution or beam loss on diagnostics, operational reliability and beam performance at the target.
- Verification of the assumed high efficiency (25%) and operational reliability.
- Test of certain components, like superconducting dipole magnets, kickers, septa, etc. under reactor driver conditions.
- Test of alternative concepts for final focusing (pulsed lenses, matrix lenses, plasma lenses).
- Pulse shaping to match the high-gain targets (timing of beams, shaping of individual beams by RF-manipulation)
- Study of non-Liouvillian techniques (i.e., circumventing the invariance of phase space by changing the charge state of the ion, electron or laser cooling) in order to improve the final phase space density.

Chapter 2

Linear theory of longitudinal instabilities in coasting beams

The performance of most machines is limited by coherent instabilities. This is one of the most important collective effects that prevent the current from being increased above a certain threshold without the beam quality getting inevitably spoilt. An intense cooled beam (high intensity contained in a small phase volume) is practically always unstable. A small density perturbation, which can be due either to previous beam manipulations or even to simple statistical noise (related to the discrete nature of the beam current), can exponentially grow and drive the whole beam into an unstable process. In phase space the beam blows up and becomes hot.

In this chapter a model for describing longitudinal instabilities is fully developed in the case of small amplitude perturbations on coasting beams. This constitutes the necessary theoretical background to allow the understanding of the measurements analyzed and discussed in the next chapters.

2.1 The issue of the longitudinal instabilities

The study of coherent longitudinal instabilities of coasting particle beams below transition has recently received new attention in connection with research on high-current circular machines considered for heavy ion inertial fusion and other applications. In high current storage rings, the longitudinal instability develops if a resistive impedance component is present and the axial momentum spread decreases below a certain threshold value [5, 6]. The longitudinal instability may cause an unacceptable increase in the beam momentum spread. This instability can be suppressed via Landau damping if the longitudinal momentum spread is sufficiently high. Unfortunately, this can conflict with other requirements. For example, in drivers for heavy ion fusion, beams with small momentum spread are needed for final focusing and thus the actual limitation coming from the longitudinal instability is a key design issue [2]. One of the challenging questions in beam physics is whether a high-current machine must necessarily operate under conditions where the beam is linearly stable: it could be acceptable to operate with a linearly unstable beam provided that either the instability saturates with an acceptable distortion in the distribution function, or the residence time in the machine is short enough to limit the growth induced by the instability [27]. Therefore, a full understanding of both linear and non-linear effects due to intense space charge – the latter arising after the initial perturbation has grown outside the range of validity of the small-amplitude analysis – is fundamental in the development of high power beam sources.

Insofar as this kind of applications are considered, experimental and theoretical study of the longitudinal instability is to be carried out on heavy ion space charge dominated beams, which are typically at non-relativistic energies: the main difference, compared with the case of high energy beams, consists in the large coupling impedance introduced by space charge, which is typically of the order of kOhms and causes a far more critical dependence of the beam dynamics on the resistive part of the global impedance.

The longitudinal instabilities of coasting beams have been studied extensively within the framework of linearized kinetic theory over several decades [5, 6]. Experimentally, plenty of relevant work has been done at the ISR (Intersecting Storage Ring) [8] and in other machines above the transition energy, where space charge effects are anyway negligible. A detailed study of the space charge dominated regime has only recently been undertaken in a linear electron channel with resistive walls [12]. This experiment has confirmed the growth rate for the unstable slow wave and the damping rate for the stable fast wave obtained from linear cold fluid theory. The fully developed nonlinear stages of the instability have been less extensively investigated to date. Saturation, decoherence effects, and energy-spread overshoot have been predicted by simulating numerically a high energy coasting beam interacting with a resonant RF cavity [9] in the absence of space charge effects.

In the ESR, experiments with Ca^{20+} and C^{6+} have been done, aiming at a careful investigation of the transition from stable regime to instability for a high-current beam. Preliminary observations and results were already drawn out in 1996, after the first measurements with a Ca^{20+} beam had taken place. Out of these data, one could clearly see the beam current signal blow up, and distinguish the linear phase of the exponentially increasing amplitude from the subsequent instability saturation [28]. A more quantitative analysis was not possible then because of a lack of more precise information about the cavity eigenfrequency as the beam was caused to become unstable on the second harmonic due to the cavity contribution to the global longitudinal impedance. With the data recorded in the beam time of February 1997, a more accurate investigation has been made possible by a good knowledge of the working conditions during the data acquisition. Thanks to that, the RF cavity-driven longitudinal instability of a cooled, coasting C^{+6} intense beam below transition energy ($\gamma \simeq 1.36$), with $I_0 \cong 0.3$ mA and $(\Delta p/p_0)_{\mathrm{FWHM}} = 1.1 \cdot 10^{-5}$, has been studied in great detail [29, 30] (see next chapters). Measurements were taken for several and known values of the machine's longitudinal coupling impedance.
The way longitudinal instability changes the profile of the beam line density along the ring is shown in Fig. 2.1 (the plotted data come from these latest ESR measurements). At the early stage of the instability, one mostly observes a sinusoidal modulation signal, whose amplitude grows exponentially as predicted by the linear kinetic theory (see, for example, Fig. 2.1a, which shows the beam current along the ring for a cavity impedance $\dot{Z}_{\mathrm{cav}} = 1096 + \mathrm{i}437\ \Omega$). When the perturbation reaches large amplitude, significant higher order harmonics are produced, leading to a steepening of the density profile as well as to saturation of the instability growth (Fig. 2.1b). The effects of the instability in the velocity space are not easy to deduce experimentally, because the Schottky diagnosis becomes much more difficult to use when a coherent signal appears on the beam current. Nevertheless, the momentum distribution evolution can be investigated via numerical simulation and results will be briefly discussed in Chapter 7.

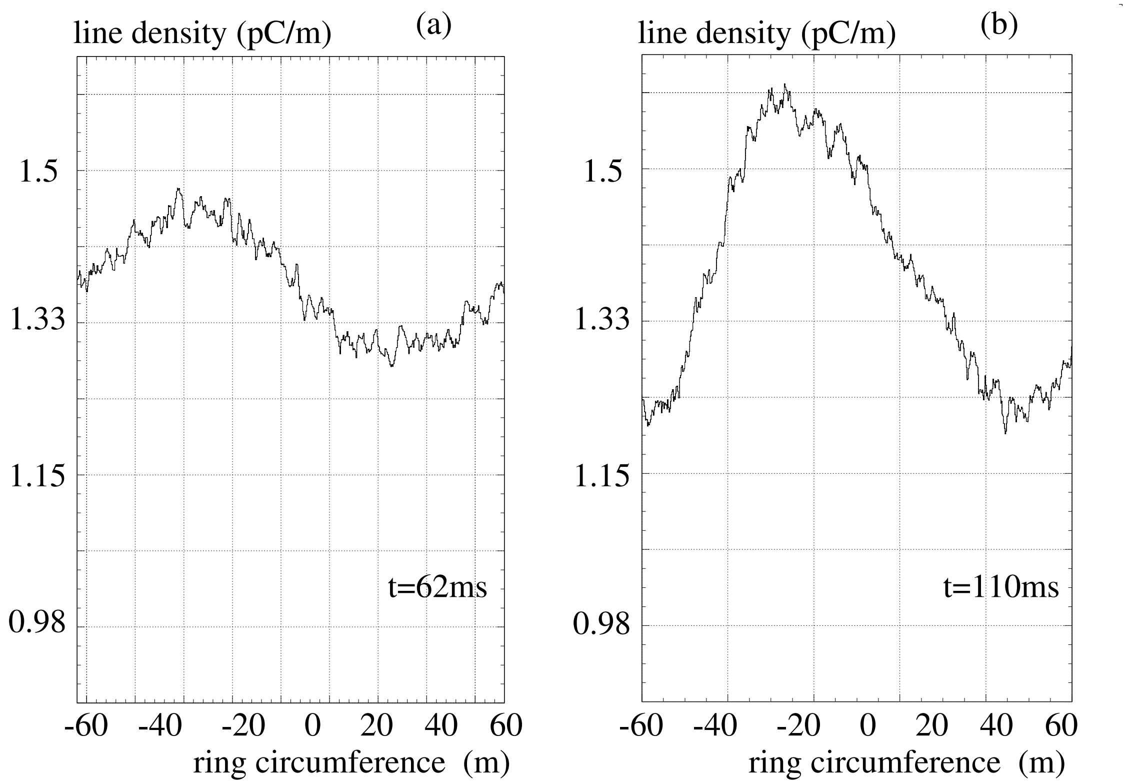

Figure 2.1: Charge line density along the ESR at two different instants when the cavity was detuned with $\Delta f = 6.7$ kHz and the beam current was $I_0 = 0.28$ mA.

2.2 Longitudinal dynamics of a coasting beam under the action of its self-field

2.2.1 The Vlasov equation

Here we will essentially review the kinetic description for the longitudinal motion of a coasting beam interacting with itself and the environment when one takes into account relativistic and dispersive effects in a self-consistent way. In the following (Sec. 3 of this chapter, Sec. 4 of next chapter, and the whole chapters 6 and 7) this model will be widely used as a starting point to derive information about the different stages in the evolution of an arbitrary coasting beam under the action of its self-fields.

Let us consider a coasting beam moving in a circular machine, (i.e., a storage ring or a circular accelerator), with nominal longitudinal velocity U_0, particle momentum p_0, particle kinetic energy ϵ_0, and nominal circular "equilibrium" orbits having radius r_0; $C_0 = 2\pi r_0$ is the circumference length. In the following we use the symbols θ and r for the azimuthal and radial coordinates, respectively (see Fig. 2.2). Furthermore, ω will denote the angular frequency, $\omega = \dot{\theta}$; with $\omega_0 = U_0/r_0$ is the nominal angular frequency. We neglect the coupling between longitudinal and transverse motion of the particles, and assume that the generic particle is always on a circular equilibrium orbit. The cross sectional distribution of the particles in the beam is assumed to be constant (or, at least, a known function $Q(x, y)$ of the cross sectional coordinates), also independent of azimuth; we are thus neglecting betatron oscillations except insofar as they contribute to the cross sectional distribution. For a given bending field the radius r of the orbit of the generic particle depends on its energy ϵ, $r = r(\epsilon)$; the revolution frequency ω of the particle depends also on its energy ϵ, as specified by the frequency dispersion of the ring $\omega = \omega(\epsilon)$ (as explained in Ref. [31]).

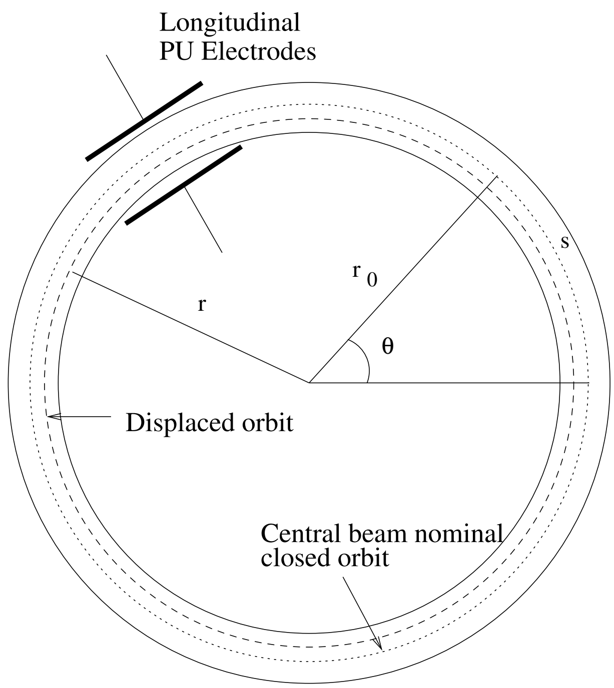

Figure 2.2: Coordinates system along the beam orbit in the storage ring.

A deviation $\Delta\epsilon$ in energy from the nominal energy ϵ_0 causes an increase Δr of the orbit radius given by

$$\frac{\Delta r}{r_0} = \frac{\alpha}{\beta_0^2}\frac{\Delta\epsilon}{\epsilon_0} \ ,$$

where $\beta_0 = U_0/c$ and α (momentum compaction factor) is a property of the guiding field and is typically much smaller than unity. The change $\Delta\omega$ in the revolution frequency is

$$\frac{\Delta\omega}{\omega_0} = -\frac{\eta}{\beta_0^2}\frac{\Delta\epsilon}{\epsilon_0} \ ,$$

where $\eta = 1/\gamma_{\mathrm{t}}^2 - 1/\gamma_0^2$ is the slip factor, $\gamma_{\mathrm{t}} = 1/\sqrt{\alpha}$ is the transition gamma and $\gamma_0 = (1-\beta_0^2)^{-1/2}$ [31]. Below the transition energy $m_0c^2\gamma_t$, the slip factor is negative and the revolution frequency increases with energy. High current storage rings like ESR operate below transition energy, namely $\gamma_0 < \gamma_{\mathrm{t}}$; thus for these machines the slip factor is negative and no negative mass instability is to be expected.

The equations for the longitudinal motion of the single particle in a circular structure can be written in terms of the variables (θ, ϵ) – the azimuthal co-ordinate along the ring circumference and the single particle energy – as

$$\left\{ \begin{array}{l} \dfrac{\mathrm{d}\theta}{\mathrm{d}t} = \omega(\epsilon) \\[2ex] \dfrac{\mathrm{d}\epsilon}{\mathrm{d}t} = qE[\theta, r(\omega); t] r\omega \end{array} \right. \ , \tag{2.1}$$

where $E = E(\theta, r; t)$ is the longitudinal electric field due to applied focusing, space charge, and to the interaction of the beam with the surroundings, and q is the electric charge of the particle. The variables θ and ϵ are not conjugate variables.
Now we make the following ansatz: in the neighborhood of the nominal orbit, the longitudinal component of the electric field depends on the radial coordinate r as $1/r$, namely

$$E(r, \theta; t) = -\frac{\phi(\theta; t)}{2\pi r} \quad , \tag{2.2}$$

where the "potential" function ϕ is independent of the radius. Under the assumption of long wavelength perturbations (compared with the characteristic transverse dimension) the expression (2.2) describes with sufficient accuracy the distribution of the longitudinal component of the electric field in an actual ring.
We introduce a new variable conjugate to θ defined as

$$w(\epsilon) = 2\pi \int_{\epsilon_0}^{\epsilon} \frac{\mathrm{d}\epsilon}{\omega(\epsilon)} \tag{2.3}$$

and the equations for $\theta(t)$ and $w(t)$ are

$$\begin{cases} \dfrac{\mathrm{d}\theta}{\mathrm{d}t} = \omega(w) \\ \\ \dfrac{\mathrm{d}w}{\mathrm{d}t} = -q\phi(\theta; t) \end{cases} \quad . \tag{2.4}$$

Therefore, if we introduce a distribution function for the beam in longitudinal phase space (θ, w), say $g = g(\theta, w; t)$, this will be a solution of the kinetic equation

$$\frac{\partial g}{\partial t} + \omega(w)\frac{\partial g}{\partial \theta} - q\phi(\theta; t)\frac{\partial g}{\partial w} = 0 \; . \tag{2.5}$$

We neglect here collisional phenomena because they do not play a considerable role on the time scale of the instability we are interested in. Finally, we want to reformulate this kinetic description of the beam in terms of a position-velocity phase space. Consequently, we introduce the variables s and v

$$\begin{aligned} s &= r_0\theta \\ v &= r_0\omega \end{aligned} \tag{2.6}$$

and let $f(s, v; t)$ be the distribution function of the beam in the (s, v)-phase space. The distribution function $f(s, v; t)$ is related to the distribution function $g(\theta, w; t)$ through the transformation

$$f(s, v, t) = \frac{1}{r_0^2}\left|\frac{\mathrm{d}w}{\mathrm{d}\omega}\right| g(\theta, w, t) \; . \tag{2.7}$$

Under the assumption of a small relative energy spread of the beam particles, we may replace ω by ω_0 in the integral (2.3) and the frequency dispersion of the ring may be approximated as

$$\omega(\Delta\epsilon) \cong \omega_0 + \kappa_0 \Delta\epsilon \; , \tag{2.8}$$

where $\Delta\epsilon = \epsilon - \epsilon_0$, $\kappa_0 = -\eta\omega_0/(\beta_0^2\epsilon_0)$, $\epsilon_0 = m_0 c^2 \gamma_0$ and m_0 is the rest mass of the particles. Using these approximations we obtain

$$w(\epsilon) \cong 2\pi(\epsilon - \epsilon_0)/\omega_0 \; , \tag{2.9}$$

and $f \cong (2\pi/r_0^2|\kappa_0|\omega_0)g$. Therefore the distribution function $f(s, v; t)$ satisfies the Vlasov equation

$$\frac{\partial f}{\partial t} + v\frac{\partial f}{\partial s} - \frac{q}{m^*}\frac{\phi(s, t)}{2\pi r_0}\frac{\partial f}{\partial v} = 0 \; . \tag{2.10}$$

To derive Eq. (2.10) we have used the relation $p_0 = \beta_0^2 \epsilon_0 / U_0$ and we have introduced the "effective" particle mass

$$m^* \stackrel{\text{def}}{=} -\frac{p_0}{U_0 \eta} \ . \tag{2.11}$$

Note that below transition m^* is positive because the slip factor η is negative. Finally, we have to specify the form of the driving term ϕ present in the Vlasov equation (2.10). In general $\phi(s,t)$ is made up of two independent contributions: an external voltage acting on the beam, which can represent either an oscillating bunching field associated with an RF cavity or a residual field detuned with respect to the beam revolution frequency, and a self-voltage coming from the interaction of the beam with the beam itself and with the surrounding environment. In the following, we shall describe the latter contribution with the impedance formalism (see next subsection) and neglect the possible presence of external applied voltages (except for Section 5.4).

2.2.2 Longitudinal field created by the beam: the longitudinal coupling impedance

Given the periodicity of the structure to which we refer, both $\phi(s,t)$ and the beam current along the ring, defined as

$$I(s,t) = q \int_{-\infty}^{\infty} v f(s,v,t) \, \mathrm{d}v \ , \tag{2.12}$$

are certainly periodic in the space coordinate s of period C_0. Thus we can expand both of them in Fourier series:

$$\begin{aligned} \phi(s,t) &= \textstyle\sum_n \phi_n(t) \exp(\mathrm{i} n \frac{s}{r_0}) \\ I(s,t) &= \textstyle\sum_n I_n(t) \exp(\mathrm{i} n \frac{s}{r_0}) \end{aligned} \tag{2.13}$$

Assuming that the response of the environment to the beam excitation is linear and time-invariant, one can think of the self-induced voltage as functional linear relation between the current that generates it, $I(s,t)$, and a single particle wake field, which can be precisely calculated according to how the environment is modeled [7]. The relation between the beam current spatial spectrum and the spatial Fourier transform of the self-induced voltage is therefore

$$\phi_n(t) = \sum_m z_{nm}(t) * I_m(t) \ , \tag{2.14}$$

which in frequency domain becomes

$$\tilde{\phi}_n(\omega) = \sum_m \dot{Z}_{nm}(\omega) \cdot \tilde{I}_m(\omega) \ , \tag{2.15}$$

where the $\dot{Z}_{nm}(\omega)$ simply represent the Fourier transform of $z_{nm}(t)$.
In order to conveniently re-write this relation, we first need to make a few observations about the structure of the n-th harmonic current spectrum that appears in (2.15). First of all, it is possible to show that $\tilde{I}_n(\omega)$ exactly corresponds to the n-th harmonic of the time signal detected by a longitudinal pick-up monitor located at an arbitrary section along the ring circumference. As the proof of this statement is quickly carried out in the following for a single particle signal, its validity can be immediately extended to beams of many particles non-interacting with each other (when the interaction amongst particles becomes not negligible, the motion of each of them changes because of that, and a different description is required [32]). We consider one single particle having charge q and moving

along a circular orbit with radius r_0 (particle velocity v_0), and a pick up signal monitor placed somewhere along its path. The signal delivered by the PU electrodes is

$$I^{\mathrm{PU}(1)}(t) = q \sum_n \delta(t - nT_0) \ , \tag{2.16}$$

whereas the beam current along the ring is written as:

$$I^{(1)}(s,t) = qv_0 \sum_m \delta[s - s(t) - 2\pi m r_0] = qv_0 \sum_m \delta[s - v_0 t - 2\pi m r_0] \ . \tag{2.17}$$

In the above formulae T_0 is the particle revolution period, $T_0 = 2\pi/\omega_0 = 2\pi r_0/v_0$. Fourier transforming (2.16), we obtain:

$$\tilde{I}^{\mathrm{PU}(1)}(\omega) = q\frac{\omega_0}{2\pi} \sum_n \delta\left(\omega - n\frac{\omega_0}{2\pi}\right) \ . \tag{2.18}$$

Expansion in Fourier series of the current signal (2.17) with respect to the periodic variable s yields

$$I^{(1)}(s,t) = \sum_n I_n^{(1)}(t) \exp(\mathrm{i}ns/r_0) \ , \tag{2.19}$$

where the coefficients $I_n^{(1)}(t)$ can be evaluated as:

$$I_n^{(1)}(t) = \frac{qv_0}{2\pi r_0} \int_0^{2\pi r_0} \sum_m \delta(s - v_0 t - 2\pi m r_0) \exp(-\mathrm{i}ns/r_0)\mathrm{d}s = \frac{qv_0}{2\pi r_0} \exp(-\mathrm{i}nv_0 t/r_0) \ . \tag{2.20}$$

At this point it is straightforward to obtain:

$$\tilde{I}_n^{(1)}(\omega) = \frac{q\omega_0}{2\pi} \delta\left(\omega - n\frac{\omega_0}{2\pi}\right) \ , \tag{2.21}$$

and from here, after comparison with the spectrum of the pick-up signal, Eq. (2.18):

$$\tilde{I}^{\mathrm{PU}(1)}(\omega) = \sum_n \tilde{I}_n^{(1)}(\omega) \ . \tag{2.22}$$

This proves that $\tilde{I}_n(\omega)$ in Eq. (2.15) can be regarded as the n-th harmonic of a signal detected by a pick-up monitor. But such a signal can be easily evaluated and besides, it is known from experiments: it has a very narrow band centered around the frequency $n\omega_0$ (one or two narrow peaks, according to whether the beam is space charge dominated or not – see, for instance, Fig. 2.3 with simulated spectra around the 5th harmonic both for a beam made up of non-interacting particles and for a space charge dominated beam); its width is directly related to the beam momentum spread, or to other relevant parameters like the space charge impedance (this is the principle on which the whole Schottky diagnosis is based) [32]; and it is in general, at least up to very high harmonic numbers, far smaller than the band-width of any impedance acting on that harmonic — even narrow-band cavity impedances. The reason why the current spectrum has narrow bands centered at $n\omega_0$ is the following: a spatial perturbation with harmonic number n in the beam frame produces a signal oscillating in time at frequency nv_0/r_0 in the laboratory frame, where v_0 is the beam mean velocity.

For example, one might consider the ESR beam with which our measurements have been carried out: the beam momentum spread was around 10^{-5}, causing a spread in the revolution frequencies of $\simeq 8$ Hz, whereas the cavity impedance acting on the first harmonic is just a few kHz wide (in Fig. 2.4 one can see the measured Schottky spectrum as well as the calculated one [30]). On higher order harmonics there was the space charge reactance alone acting, or broad band impedances at any rate (see following subsections), which are enough smeared along the frequency axis, that they can be reasonably approximated as constant in the close neighborhood of each multiple of ω_0.

We first seek to divide the contributions to the self-induced potential into a part due to the uniform, not varying in space, structure surrounding the beam (the vacuum chamber, carrying along thus the space charge plus the effect of the finite conductivity of the pipe), and a part due to the concentrated discontinuities, like RF-cavities (see Fig. 2.5):

$$\phi(s,t) = \phi^{(\mathrm{unif})}(s,t) + \phi^{(\mathrm{cav})}(s,t) \ . \tag{2.23}$$

To do that, we need to assume that these self-produced fields do not influence each other: in other words, the space charge field does not see the discontinuities, and the field induced in the cavity cannot propagate in the beam pipe because it is below cut-off. Because of the space invariance of the structure considered when calculating the "smooth" part of the field, we expect that $z_{nm}(t) = z_n^{(\mathrm{unif})}(t)\delta_{nm}$ and thus the relation between the spatial Fourier coefficients of the expansion in the space variable s will be of the kind:

$$\phi_n^{(\mathrm{unif})}(t) = z_n^{(\mathrm{unif})}(t) * I_n(t) \quad \Rightarrow \quad \tilde{\phi}_n^{(\mathrm{unif})}(\omega) = \dot{Z}_n^{(\mathrm{unif})}(\omega)\tilde{I}_n(\omega) \ . \tag{2.24}$$

In the next subsections indeed, we figure out the expression of the space charge impedance, and there it will be proved that $z_{(\mathrm{sc})n} = z_{\mathrm{sc}}(n)\delta(t)$, such that the space charge induced field appears in the form:

$$\phi_{(\mathrm{sc})}(s,t) = \sum_n z_{\mathrm{sc}}(n) I_n(t) \exp\left(\mathrm{i}n\frac{s}{r_0}\right) \ . \tag{2.25}$$

Furthermore, for low harmonic numbers, the resistive wall impedance introduced by the finite conductivity of the beam pipe depends only upon ω, $\dot{Z}_{(\mathrm{RW})n}(\omega) \to \dot{Z}_{\mathrm{RW}}(\omega)$, and in the frequency domain (2.24) becomes:

$$\tilde{\phi}_{(\mathrm{RW})n}(\omega) = \dot{Z}_{\mathrm{RW}}(\omega)\tilde{I}_n(\omega) \approx \dot{Z}_{\mathrm{RW}}(n\omega_0)\tilde{I}_n(\omega) \ ,$$

having considered the shape of the $\tilde{I}_n(\omega)$, as discussed above.

It is clear as a consequence, that the global self-induced field due to space charge and to the resistivity of the beam pipe can be written as:

$$\phi_{\mathrm{unif}} = \sum_n \dot{Z}(n\omega_0) I_n(t) \exp\left(\mathrm{i}n\frac{s}{r_0}\right) \ , \tag{2.26}$$

having defined $\dot{Z}(n\omega_0) \stackrel{\mathrm{def}}{=} z_{\mathrm{sc}}(n) + \dot{Z}_{\mathrm{RW}}(n\omega_0)$.
When the contribution of the RF-cavity is taken into account, we assume that the field produced in there depends solely on the beam current at that particular location, and can be written as (Fig. 2.5):

$$\phi_{\mathrm{cav}}(s,t) = I(s=0,t) * z_{\mathrm{cav}}(t)\Pi_\Delta(s) \ , \tag{2.27}$$

where $\Pi_\Delta(s)$ is a function whose value is $(2\pi r_0)/\Delta$ in the interval $(0,\Delta)$ – Δ being the length of the cavity, $\Delta \ll r_0$ – on the s axis, and 0 everywhere else. As we know from the

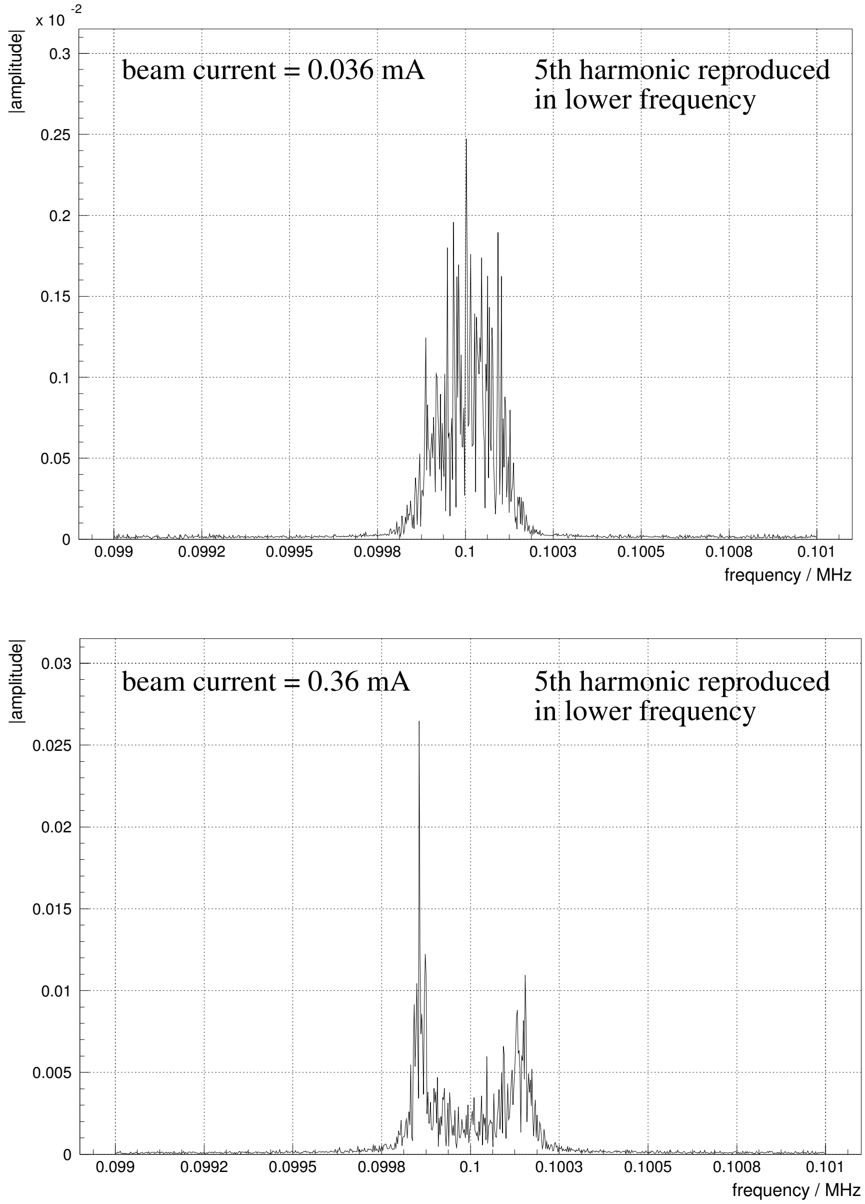

Figure 2.3: Simulated Schottky spectra from a C^{+6} beam with a momentum spread close to 10^{-5} and energy 340 MeV/u: the signal is taken around the 5th harmonic of the revolution frequency, but it is reproduced in lower frequency due to the bigger time step chosen for both simulations. In the above spectrum the beam current was chosen to be 0.036 mA and consequently space charge effects are not dominant and also the momentum spread is directly related to the width of the Schottky band; in the spectrum below, on the other hand, the current was one order of magnitude higher, and both slow and fast wave are sensibly excited via space charge, with consequent deformation of the spectrum, which becomes double-peaked.

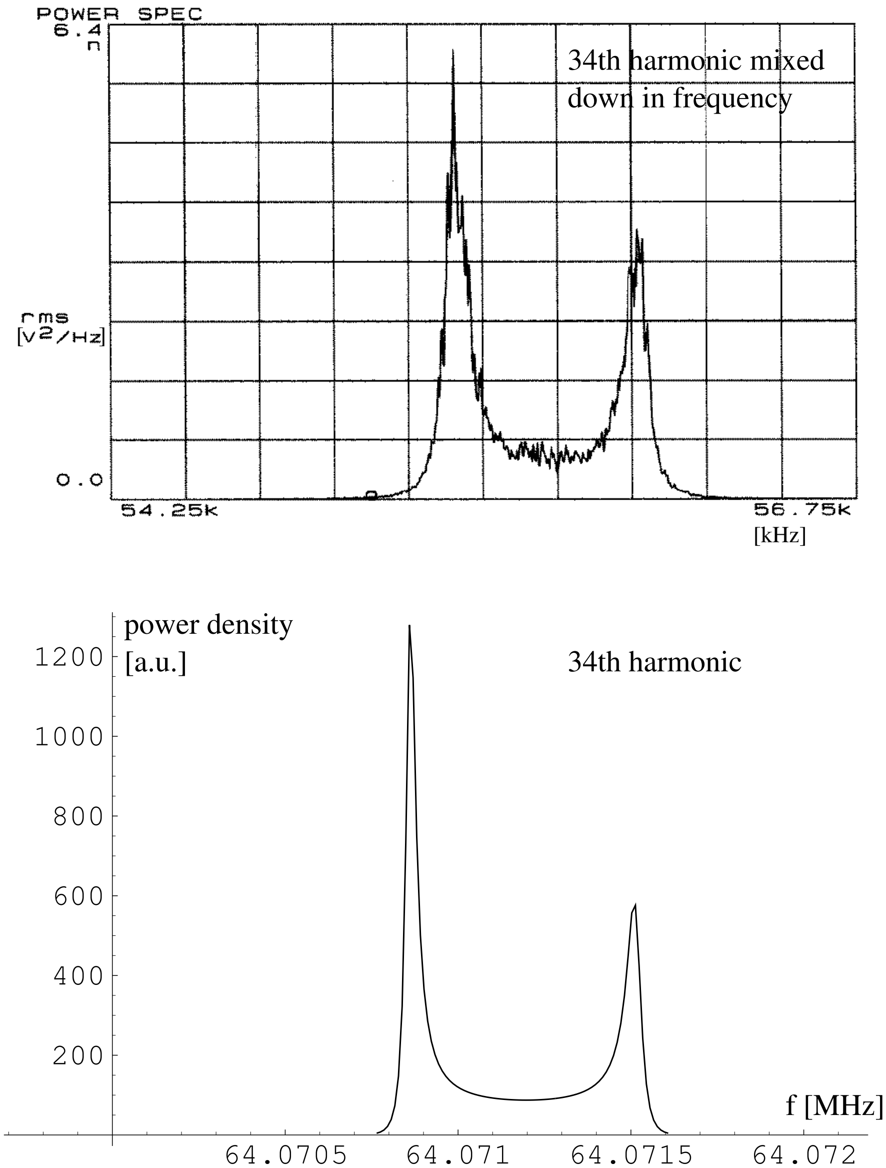

Figure 2.4: Schottky spectra from an ESR C^{+6} beam around the 34th harmonic of its revolution frequency. Above: measured signal. Below: evaluated signal [36].

previous considerations, the current at the location $s = 0$ can be written as sum of different time signals having each a band centered around $m\omega_0$, and in addition the function Π_Δ can be expanded in Fourier series. This yields:

$$\phi_{\mathrm{cav}}(s,t) = \left[\sum_m I_m(t) * z_{\mathrm{cav}}(t)\right] \sum_n \alpha_n \exp\left(\mathrm{i}n\frac{s}{r_0}\right) \tag{2.28}$$

Since the $I_m(t)$ go as $\exp(-\mathrm{i}m\omega_0\, t)$, the total field will be a superposition of different waves having phase velocities $(m/n)r_0\omega_0$. Amongst them, we only choose those that are in phase with the beam, that means those having phase velocities $v_0 = r_0\omega_0$, as the ones that can significantly affect the beam dynamics because their effect does not average to

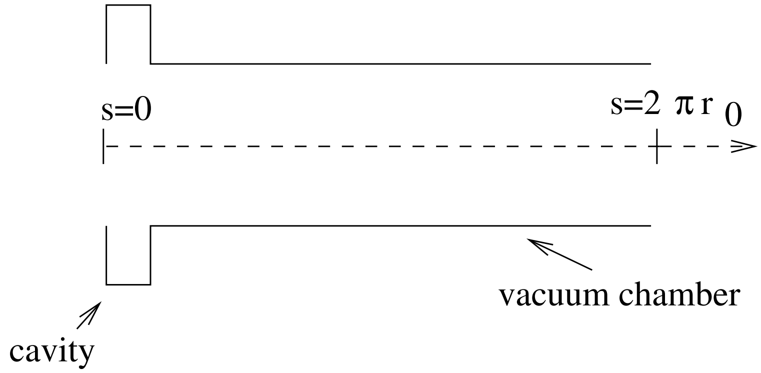

Figure 2.5: Schematic view of the accelerator environment as it influences the beam dynamics through the self-induced fields.

zero: this requires the condition $m = n$ to be verified. Thus, the effective self-induced RF-cavity field will eventually appear as:

$$\phi_{\text{cav}}(s,t) \approx \sum_n \alpha_n [I_n(t) * z_{\text{cav}}(t)] \exp\left(\mathrm{i}n\frac{s}{r_0}\right) \ , \tag{2.29}$$

which, for low harmonic numbers ($n \ll 2\pi r_0/\Delta$), can be again put into the form

$$\sum_n [I_n(t)\dot{Z}_{\text{cav}}(n\omega_0)] \exp\left(\mathrm{i}n\frac{s}{r_0}\right) \ , \tag{2.30}$$

since the Fourier transformed coefficients of the expansion (2.29) are $\tilde{\phi}_{(\text{cav})n}(\omega) = \tilde{I}_n(\omega)\dot{Z}_{\text{cav}}(\omega) \approx \tilde{I}_n(\omega)\dot{Z}_{\text{cav}}(n\omega_0)$, and moreover $\alpha_n \approx \alpha_0 = 1$.
This diversion has been necessary to conclude that one does not commit a major mistake when, limiting oneself to considering the kinds of beam interactions above discussed, one re-writes (2.14) as

$$\phi_n(t) \simeq \dot{Z}(n\omega_0) I_n(t) \ , \tag{2.31}$$

which yields

$$\phi(s,t) = \sum_n \dot{Z}(n\omega_0) I_n(t) \exp(\mathrm{i}ns/r_0) \ , \tag{2.32}$$

where

$$\dot{Z}(n\omega_0) = z_{\text{sc}}(n) + \dot{Z}_{\text{RW}}(n\omega_0) + \dot{Z}_{\text{cav}}(n\omega_0) \ . \tag{2.33}$$

The relation (2.32) will be always used in the following in order to express the self-field in a consistent way. Impedances are either beam characteristics (space charge impedance) or machine parameters (all the others, since they only depend on the ring properties), and with the Schottky and BTF analysis they can be satisfactorily estimated for each ring and in whatever working conditions [32, 33, 34, 36].

2.2.3 Space charge and cavity impedances

The self-field follows Maxwell's equations with the boundary conditions imposed by the environment. It is obvious that:

- the detailed environment seen by the beam is different for different machines and changes around the circumference of a given ring.

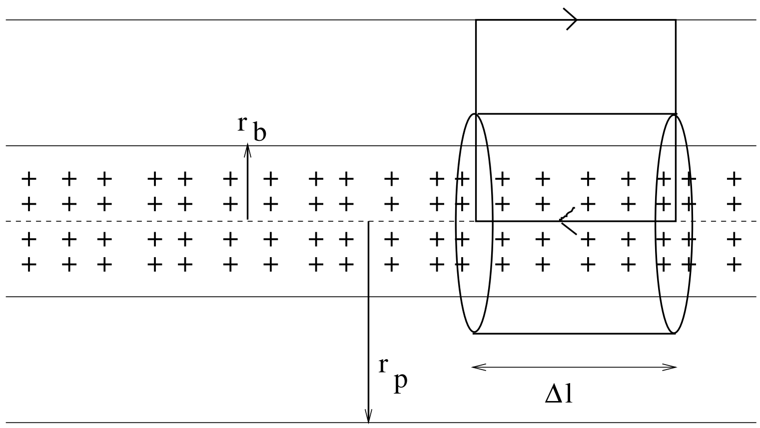

Figure 2.6: Ion beam propagating in a perfectly conducting pipe.

- one cannot expect to analytically express exact solutions for the electromagnetic field with handy formulae.

In view of this, in this subsection we will first of all consider the simplest type of environment and use the resulting electromagnetic field expression to show how the definition of coupling impedance applies. The second step will be to take into consideration the interaction beam-cavity and describe it: this is specially remarkable in the present context for the experimental part connected with this work.
Therefore, we start by considering a round beam of radius $r_{\rm b}$ traveling in a straight line – its mean velocity being $v_0 = \beta_0$ c – along the axis of a circular pipe of radius $r_{\rm p}$. To make things easier, we shall assume a perfectly conducting pipe and also limit our analysis to long wavelength perturbations of the beam current, in such a way that the fields created do not propagate inside the structure and vary only over long distances compared with the beam pipe radius. The starting point is the full set of Maxwell's equations:

$$\begin{aligned} &\int_\gamma \vec{E}\cdot\hat{s}\,\mathrm{d}s = -\frac{\mathrm{d}}{\mathrm{d}t}\int_{S_\gamma}\vec{B}\cdot\hat{n}\,\mathrm{d}S \qquad &&\int_\Sigma \vec{E}\cdot\hat{n}\,\mathrm{d}S = \frac{1}{\epsilon_0}\int_{V_\Sigma}\rho\,d\tau \\ &\int_\gamma \vec{B}\cdot\hat{s}\,\mathrm{d}s = \mu_0\int_{S_\gamma}\left[\vec{J}+\epsilon_0\frac{\partial\vec{E}}{\partial t}\right]\cdot\hat{n}\,\mathrm{d}S \qquad &&\int_\Sigma \vec{B}\cdot\hat{n}\,\mathrm{d}S = 0\ . \end{aligned} \tag{2.34}$$

Applying Gauss's law to the cylinder in Fig. 2.6 and assuming that the contributions to the flux through the bases of the cylinder is negligible, we obtain

$$E_r(r) = \begin{cases} \dfrac{\rho}{2\epsilon_0}\dfrac{r_{\rm b}^2}{r} \quad \text{if} \quad r > r_{\rm b} \\ \dfrac{\rho}{2\epsilon_0} r \quad \text{if} \quad r \le r_{\rm b} \end{cases}, \tag{2.35}$$

whereas Ampere's law applied to the perimeter of one of the cylinder's bases gives

$$B_\varphi(r) = \begin{cases} \dfrac{\mu_0 \Lambda v_0}{2\pi r} \quad \text{if} \quad r > r_{\rm b} \\ \mu_0\Lambda v_0 \dfrac{r}{2\pi r_{\rm b}^2} \quad \text{if} \quad r \le r_{\rm b} \end{cases}, \tag{2.36}$$

provided that one neglects the contribution of the time derivative of the electrical field $\vec{E}$ in the global balance of the current densities. Here we have introduced the beam line density $\Lambda(s,t) = \rho(s,t)\pi r_{\rm b}^2$, which is linked to the local current by the simple relation: $I(s,t) \simeq v_0\Lambda(s,t)$. Next step is to use Faraday's law on the rectangular oriented path in Fig. 2.6:

$$E_s(r=0)\Delta l = -\frac{\mathrm{d}}{\mathrm{d}t}\int_S B_\varphi(r)\,\mathrm{d}S + \int_0^{r_{\rm p}} E_r(r,s=0)\,\mathrm{d}r - \int_0^{r_{\rm p}} E_r(r,s=\Delta l)\mathrm{d}r =$$

$$= -\frac{\mu_0 v_0 g\Delta l}{4\pi}\frac{\partial\Lambda}{\partial t} + \frac{\Lambda(s=0)g}{4\pi\epsilon_0} - \frac{\Lambda(s=\Delta l)g}{4\pi\epsilon_0}\,. \tag{2.37}$$

In the last passage we have defined the g-factor referred to the field on the longitudinal axis: $g = 1 + 2\ln(r_{\rm p}/r_{\rm b})$. But this definition can be generalized and made independent of the choice $r = 0$ by redefining a g-factor transversely averaged: $g = 0.5 + 2\ln(r_{\rm p}/r_{\rm b})$ [31]. Since for the continuity equation applied to the beam it is

$$\frac{\partial\Lambda}{\partial t} = -\frac{\partial I}{\partial s} \simeq v_0\frac{\partial\Lambda}{\partial s}\,,$$

from (2.37) we finally write the expression of the longitudinal electric self field averaged all over the transverse plane:

$$E_s(s,t) = -\frac{g}{4\pi\epsilon_0\gamma_0^2}\frac{\partial\Lambda}{\partial s}\,. \tag{2.38}$$

As we know, every beam line density perturbation is in the form: $\Lambda(s,t) = \sum_n \Lambda_n(t)$ $\exp(\mathrm{i}ns/r_0)$, and therefore (2.38) becomes:

$$E_s(s,t) = \frac{1}{2\pi r_0}\sum_n\left[-\frac{\mathrm{i}gn}{2\epsilon_0\gamma_0^2\beta_0\mathrm{c}}I_n(t)\right]\exp(\mathrm{i}ns/r_0)\,. \tag{2.39}$$

Comparing (2.32) and (2.39), it is possible to deduce the right expression for the space charge impedance at low frequencies (well below the cut-off frequency of the beam pipe), that is:

$$z_{(\mathrm{sc})n} = -\frac{\mathrm{i}gZ_0 n}{2\gamma_0^2\beta_0} \quad\Rightarrow\quad \dot{Z}_{\rm sc}(\omega) = -\frac{\mathrm{i}gZ_0}{2\gamma_0^2\beta_0}\frac{\omega}{\omega_0}\,. \tag{2.40}$$

Using expression (2.38), we can quickly find out "a posteriori" what is the range of validity of the two approximations made in the evaluation of the field. It is easy to show that neglecting the contribution of the flux through the bases of the cylinder in Fig. 2.6 is equivalent to requiring that

$$\left|\frac{\Lambda}{\epsilon_0}\Delta l\right| \gg \left|\frac{\partial E_s}{\partial s}\Delta l\pi r_{\rm p}^2\right|\,, \tag{2.41}$$

whereas having neglected the contribution of the displacement current in the evaluation of the global flux of current density to obtain the (2.36) needs:

$$|\mu_0\Lambda v_0| \gg \left|\pi r_{\rm p}^2\epsilon_0\mu_0\frac{\partial E_s}{\partial t}\right|\,. \tag{2.42}$$

Both conditions are equivalent to the single

$$|\Lambda| \gg \left|\frac{g r_{\rm p}^2}{4\gamma_0^2}\frac{\partial^2\Lambda}{\partial s^2}\right|\,. \tag{2.43}$$

If one assumes the line density to have a longitudinal profile like $\sim \exp(\mathrm{i}s/\lambda)$, the above condition immediately re-writes as:

$$\lambda \gg r_{\mathrm{p}} \quad \text{or, in terms of harmonic number,} \quad n \ll \frac{r_0}{r_{\mathrm{p}}}\,, \tag{2.44}$$

having taken into account that we are dealing with a non-ultrarelativistic beam ($\gamma_0 \sim 1$) and the g-factor is also in general at least around 4–5.
For shorter wavelengths, that means for higher harmonic numbers, this expression is not valid any longer, and the space charge impedance rapidly vanishes in the range above the cut-off frequency of the beam pipe.

Resonating objects placed along a ring are a major problem for the effects they may have on a beam which keeps crossing them as it circulates therein. Particles well separated in time are coupled by such objects: this is because the response of very good resonators to the beam excitation, namely the wake field, stays undamped for a long time. RF cavities, for instance, which are designed and used on the very purpose to keep a longitudinal field inside of them in order to accelerate or bunch the particle beam, are the most frequent sources of narrow-band impedances. For their applications, they are generally tuned to resonate at the fundamental frequency $h\omega_0$, but their eigenfrequency may be as well driven far away from such values, as we will see. The impedance of an RF cavity is often written as

$$\dot{Z}_{\mathrm{cav}} = \frac{R_{\mathrm{s}}}{1 + \mathrm{i}Q\left(\dfrac{\omega}{\omega_{\mathrm{r}}} - \dfrac{\omega_{\mathrm{r}}}{\omega}\right)}\,, \tag{2.45}$$

where R_{s}, Q and ω_{r} are respectively the shunt impedance of the cavity, its quality factor and its eigenfrequency. The proof that expression (2.45) really is the Fourier transform of the wake field can be found in Ref. [7]. Anyhow, it is not very hard to convince oneself that the field induced by a beam crossing a cavity may act back on the beam itself and amplify the harmonic component of the current that had previously excited it. Of course the closer is the cavity eigenfrequency to a multiple of ω_0, the larger the amplitude of the induced field will be (the beam current spectrum has significant harmonic contributions at these frequencies, in fact): consequently the more dangerous the effect of the self-field on the beam will also be. This is exactly what Eq. (2.45) contains plus information about the phase relation between self-bunching field and beam current longitudinal distribution. The parameters R_{s} and Q relative to a certain machine can be deduced from a series of BTF measurements taken for known values of the cavity eigenfrequency. For example, all the measurements made at the ESR have clearly shown how close to reality this modeling of the interaction between beam and cavity is [35]. Figure 2.7 shows both real and imaginary part of the cavity impedance for the ESR, having used the previously measured values $R_{\mathrm{s}} = 1270\ \Omega$ and $Q = 50$.

A good knowledge of the key parameters so far introduced ($\dot{Z}_{\mathrm{sc}}$, R_{s}, Q, ω_{r}) greatly contributes to having a good control on a wide range of unwanted unstable evolutions that can occur in a beam. In particular, if one limits oneself to consider these two impedances alone acting on a given beam – which is indeed very close to reality some times, like in the ESR measurements that will be described in the next chapters – then a compact way to summarize the whole question of the longitudinal instability of a coasting beam in a ring is shown in Fig. 2.8. An initial beam current perturbation produces fields that act back on the beam and modify the current in the way that Vlasov equation predicts; this "updated" current will be then the source of "updated" fields, and the loop closes with that. The

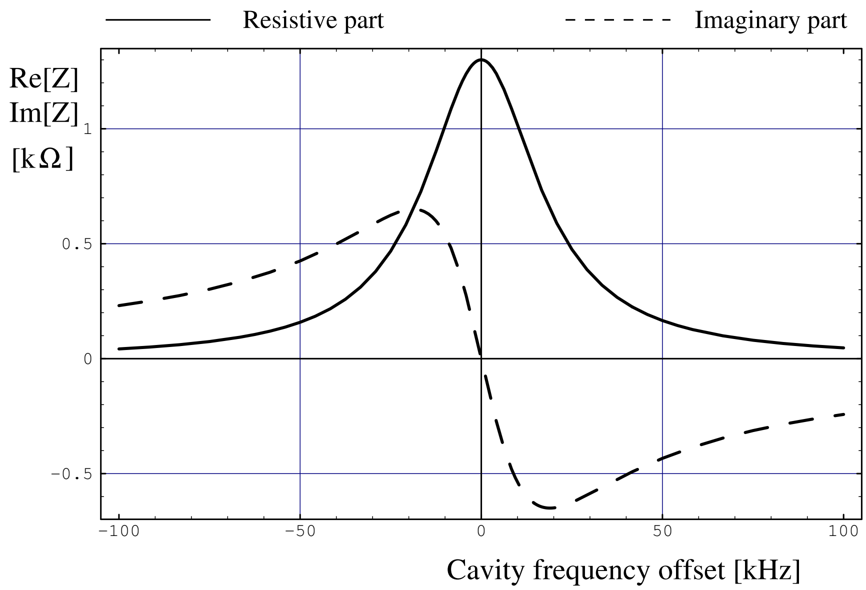

Figure 2.7: Longitudinal impedance of the ESR cavity.

situation in Fig. 2.8 might be a regime situation, where no growing signal is generated and kinetic mechanisms contained in the black box *Vlasov* never let the induced fields go above a certain level, or it might as well represent a time evolving situation, where the action of the self fields enhances the initial perturbation and self bunching sets in.

2.2.4 Other contributions to the longitudinal impedance

In order to give a satisfactory inventory of all significant components to a ring impedance, which can be handily employed to explain the great majority of longitudinal unstable phenomena, we finally have to mention and briefly describe two more contributions: the resistive wall impedance, used to account for the finite conductivity of the beam pipe, and the broad band impedance, which allows accounting for the effect of the numerous "non-idealities" present along the beam path (any box or local enlargement in the beam tube which can resonate).

For the contribution coming from the finite conductivity σ of the beam pipe, there exist essentially two regimes [37]. At very low frequencies, when the skin depth δ is larger than the wall thickness δ_{w}, the impedance seen by the beam is:

$$\dot{Z}_{\mathrm{RW}}(n\omega_0) = \frac{1}{\sigma}\frac{r_0}{r_{\mathrm{p}}\delta_{\mathrm{w}}} \tag{2.46}$$

At high frequencies, the wall is thicker than the skin depth. It can be shown that the previous formula must be amended by replacing δ_{w} by δ and multiplying by $(1+\mathrm{i})$ (an imaginary term appears),

$$\dot{Z}_{\mathrm{RW}}(n\omega_0) = (1+\mathrm{i})\frac{Z_0\beta_0\delta_0}{2r_{\mathrm{p}}}\sqrt{n}\ , \tag{2.47}$$

where $\delta_0^2 = 2/(\mu_0\sigma\omega_0)$ and $\delta^2 = \delta_0^2\omega_0/\omega$. The transition between the two expressions occurs when $\delta = \delta_{\mathrm{w}}$. The energy lost in the wall is drawn from the beam, which is

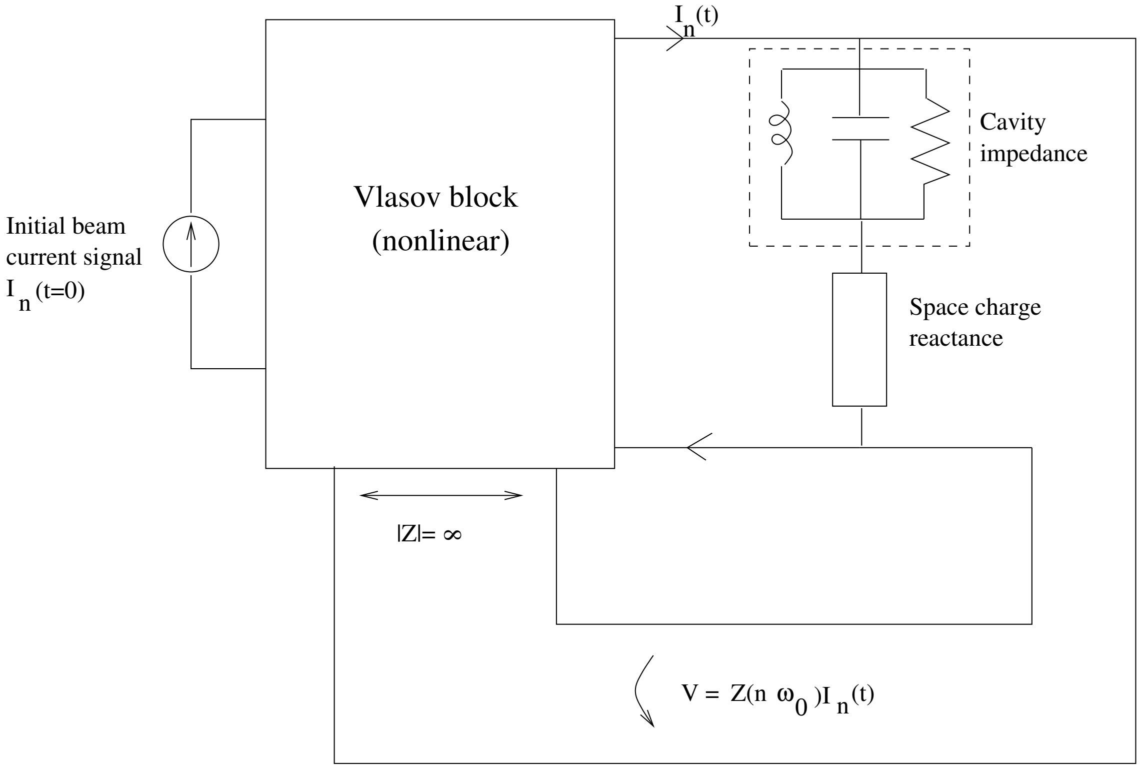

Figure 2.8: Circuital model for the electromagnetic problem of the interaction beam-beam and beam-cavity.

consequently decelerated. As far as instabilities are concerned, the resistive wall impedance is not a source of big worries in the longitudinal direction, whereas it essentially affects the transverse motion [38].
The last component of the impedance comes from the several changes of the cross section, kickers, pick-up electrodes, etc. It is obvious that these structures can trap some energy in form of magnetic field energy, and therefore behave like an inductance at low frequencies. This has been measured on existing machines [37]. From measurements one has also learned that, when no special care is taken, the vacuum chamber is essentially resistive at frequencies around the pipe cut-off frequency. This is due to the fact that the path followed by the return current is very complicated and the resistance is high when the vacuum chamber wall is not smooth, or correctly shielded along the longitudinal axis. It has also been observed that the resistive part drops at frequencies higher than the cut-off frequency. The object to represent all the above observations with a simple impedance model is a broad band resonator with a resonant frequency around the vacuum pipe cut-off frequency. This can give in general overall satisfactory results. To a certain extent, most experimental results drawn from existing rings have been correctly fitted by assuming the existence of such a component with $Q \simeq 1$ and a shunt resistance R_s adjusted to obtain the good value of the low frequency inductance [37]. Concerning orders of magnitudes, the full range

$$0.2\,\Omega \leq \frac{|\dot{Z}_{\mathrm{BB}}|}{n} \leq 50\,\Omega$$

has been found. The lowest values are achieved in modern machines. At present, a considerable effort is being put into designing very smooth chambers: unavoidable changes

of the cross section are systematically shielded and are no longer seen by the beam. For such low-Q objects, the impedance curve varies slowly with frequency and the resonator bandwidth is large. Therefore the wake field dacays rapidly. It is a local interaction that can only couple particles close to each other along the longitudinal axis.
Broad band impedances may significantly affect the beam longitudinal dynamics and give rise to microwave instabilities if the beam is space charge dominated: this is because, in spite of the low values of impedances associated with the broad band component, for quite high space charge impedances and also very high harmonic numbers a tiny little resistive part might be sufficient to drive a very quick instability. In the situations we have considered throughout this PhD work, this was not essential to be taken into consideration, since the dominant effect was a cavity driven instability on a low harmonic number. The problem can be however numerically studied employing a particle-in-cell code for the simulation of the beam longitudinal evolution (see next chapter). With this respect, one has to pay attention that, in the range where the broad band impedance normally acts, the approximation given by (2.32) might fail and one needs to go back to the more correct relation (2.15); and moreover, the beam has to be longitudinally sampled in such a way that even high harmonic oscillations (at least those in which one is interested) can be correctly resolved. All the issues connected to the accurate simulation of a very high frequency instability need to be carefully studied yet, and this is indeed a very challenging question for future deepening and work.

2.3 Linear analysis of the Vlasov equation

This section will be devoted to showing the way we obtain a *dispersion relation* between the harmonic number of a perturbation in the beam current (we deal, in fact, with a spatially periodic structure) and its complex frequency (complex, because we are mainly interested in searching for non-steady-state situations, in which current perturbations get damped or amplified). For this purpose, a harmonic analysis of the linearized Vlasov equation, which makes use of the Fourier transform, is possible but, given the non-steady-state nature of the problem, hereafter we will prefer to use the Laplace transform approach, which appears to better suit the initial value problem. The starting point is anyway the Vlasov equation (2.10) together with (2.32) that specifies the shape of the self induced voltage. The impedance should in general be the sum of the four contributions already introduced; but in practical cases, for each harmonic number, at least two or three of them are negligible with respect to the other(s):

$$\dot{Z}_{\rm tot} = \dot{Z}_{\rm sc} + \dot{Z}_{\rm cav} + \dot{Z}_{\rm RW} + \dot{Z}_{\rm BB}\ . \tag{2.48}$$

Before starting with the linearization of the Vlasov equation (2.10), it is convenient to re-write it in the rest frame of the beam by performing the following change of variables:

$$\begin{array}{l} x = s - v_0 t \\ u = v - v_0 \end{array} \quad \Rightarrow \quad \frac{\partial}{\partial s} \to \frac{\partial}{\partial x} \quad \frac{\partial}{\partial v} \to \frac{\partial}{\partial u} \quad \frac{\partial}{\partial t} \to \frac{\partial}{\partial t} - v_0 \frac{\partial}{\partial x} \tag{2.49}$$

Consequently the Vlasov equation in the new co-moving coordinates will be

$$\frac{\partial f}{\partial t} + u\frac{\partial f}{\partial x} - \frac{q}{m^*}\frac{\phi(x,t)}{2\pi r_0}\frac{\partial f}{\partial u} = 0 \tag{2.50}$$

where:

$$\phi(x,t) = \sum_n \dot{Z}_{\rm tot}(n\omega_0) I_n(t) \exp(\mathrm{i}nx/r_0) \tag{2.51}$$

$$I(x,t) = \sum_n I_n(t)\exp(\mathrm{i}nx/r_0) = qv_0 \int_{-\infty}^{\infty} (v_0+u) f(x,u,t)\,\mathrm{d}u$$

It is useful to remark here that the $I_n(t)$ that appear in this relation are different from the $I_n(t)$ that we have considered up to now only insofar as they do not contain the term $\exp(-\mathrm{i}\omega_0 t)$, which is now included in the exponential term of the Fourier expansion. Anyway this is completely legitimate, as we have already once pointed out how each $I_n(t)$ is actually a narrow-band signal centered around $n\omega_0$. The new $I_n(t)$ are the same as the old ones, only shifted to the low frequencies range. They express, in other words, the only slow collective motion of the beam, and hide the beam's much quicker revolutions around the ring.

2.3.1 Dispersion relation

We assume the longitudinal distribution function of the beam to be sum of an equilibrium coasting-beam part and a small perturbation

$$f(x,u,t) = f_0(u) + \delta f(x,u,t) = f_0(u) + \sum_n \delta f_n(u,t)\exp(\mathrm{i}nx/r_0)\ , \tag{2.52}$$

and of course the harmonic components of the current will be given by:

$$I_n(t) \approx qv_0 \int_{-\infty}^{\infty} \delta f_n(u,t)\,\mathrm{d}u \quad I_0 = \int_{-\infty}^{\infty} f_0(u)\,\mathrm{d}u\ , \tag{2.53}$$

the perturbations in the velocity being anyway far smaller than the beam's mean velocity all along the ring circumference. If we substitute the ansatz (2.52) and the self induced potential (2.51) in the Vlasov equation in the beam rest frame (2.50), and then neglect the second order terms – which means we are linearizing this equation – we obtain:

$$\frac{\partial \delta f}{\partial t} + u\frac{\partial \delta f}{\partial x} - \frac{q}{m^*}\frac{\sum_n \dot{Z}_{\mathrm{tot}}(n\omega_0) I_n(t)\exp(\mathrm{i}nx/r_0)}{2\pi r_0}\frac{\mathrm{d}f_0}{\mathrm{d}u} = 0$$

$$\frac{\partial \delta f_n}{\partial t} + \frac{\mathrm{i}nu}{r_0}\delta f_n - \frac{q^2 v_0 \dot{Z}_{\mathrm{tot}}(n\omega_0)}{m^* 2\pi r_0}\frac{\mathrm{d}f_0}{\mathrm{d}u}\int_{-\infty}^{\infty} \delta f_n du = 0\ . \tag{2.54}$$

In order to solve Eq. (2.54), we first transform it into the Laplace domain by defining

$$F_n(p,u) \stackrel{\mathrm{def}}{=} \mathrm{Lapl}[\delta f_n(t,u)] \tag{2.55}$$

$$F_n(p,u) - \frac{\delta f_n(0,u)}{p+\mathrm{i}un/r_0} - \frac{q^2 v_0}{m^* 2\pi r_0}\frac{\mathrm{d}f_0/\mathrm{d}u\cdot \dot{Z}_{\mathrm{tot}}(n\omega_0)}{p+\mathrm{i}un/r_0}\int_{-\infty}^{\infty} F_n(p,u)\,\mathrm{d}u = 0\ \ ,$$

and then integrate on the velocity space. In this way we get:

$$\int_{-\infty}^{\infty} F_n(p,u)\,\mathrm{d}u = \Upsilon_n(p) = \frac{\displaystyle\int_{-\infty}^{\infty} \frac{\delta f_n(0,u)}{p+\mathrm{i}un/r_0} du}{1 - \dfrac{q^2 v_0 \dot{Z}_{\mathrm{tot}}(n\omega_0)}{m^* 2\pi r_0}\displaystyle\int_{-\infty}^{\infty} \frac{\mathrm{d}f_0/\mathrm{d}u}{p+\mathrm{i}un/r_0}\,\mathrm{d}u} = \frac{N(p)}{D(p)}\ . \tag{2.56}$$

Of course $\Upsilon_n(p)$ represents the Laplace transform of the n-th harmonic of the perturbation on the beam current:

$$\Upsilon_n(p) \stackrel{\mathrm{def}}{=} \mathrm{Lapl}[I_n(t)]\ .$$

The next step consists now in going back to the time domain after inversion of the Laplace transform in (2.56). As we know, a Laplace transform must be analytical in a half-plane

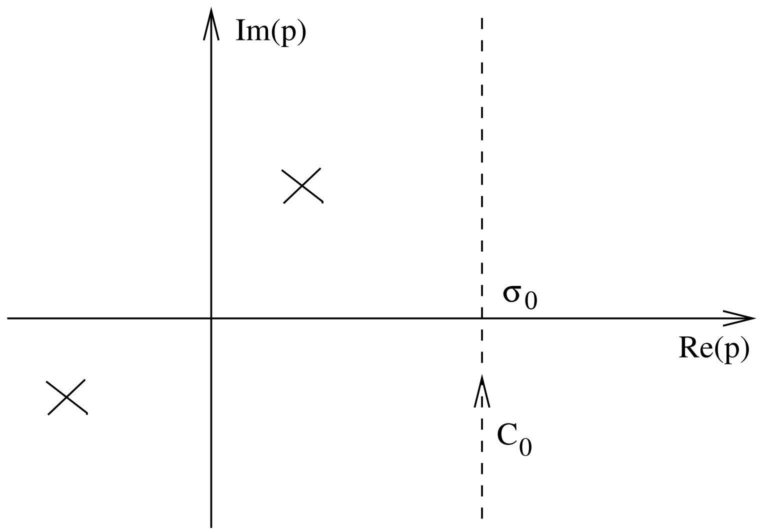

Figure 2.9: Vertical line for the correct inversion of the Laplace transform in (2.56).

$\sigma > \sigma_{\rm c}$, where $\sigma_{\rm c}$ is the convergence abscissa of the Laplace transform. The function that defines $\Upsilon_n(p)$ is in fact analytical in the half-plane $\sigma > 0$. It has got a clear discontinuity across the imaginary axis (when p crosses this axis, namely when Re(p) changes sign, both $N(p)$ and $D(p)$ are discontinuous since in the integrals which they contain the contribution of the pole gets suddenly left out). This means that any inversion of the (2.56) that is carried out on a line belonging to the convergence domain (see Fig. 2.9) is correct and leads to the right result:

$$I_n(t) = \frac{1}{2\pi \mathrm{i}} \int_{C_0} \Upsilon(p) \exp(pt)\, \mathrm{d}p \quad . \tag{2.57}$$

Nevertheless, we might want to express the solution in the time domain as the sum of the residues of the poles of $\Upsilon_n(p)$ in the whole complex plane:

$$I_n(t) = \sum_k \mathrm{Res}[\Upsilon_n(p)\exp(pt), p_k] = \sum_k \exp(p_k t)[(p-p_k)\Upsilon_n(p)]_{p=p_k} \tag{2.58}$$

In this case the analytical continuation of $\Upsilon_n(p)$ must be correctly considered and thus the integrals present in $N(p)$ and $D(p)$ must be substituted by themselves plus the pole contribution through the residue, as Re(p) reverses its sign (which corresponds to changing in the integrals the integration path from the real axis to the Landau path, as shown in Fig. 2.10). The p_k that appear in Eq. (2.58) are the solutions of the equation

$$D(p) = 1 - \frac{q^2 v_0 \dot{Z}_{\rm tot}(n\omega_0)}{m^* 2\pi r_0} \int_L \frac{\mathrm{d}f_0/\mathrm{d}u}{p + \mathrm{i}un/r_0}\, \mathrm{d}u = 0 \, , \tag{2.59}$$

and here it has been tacitly assumed that $N(p)$ does not have poles itself on one side, and moreover that Eq. (2.59) has got only first order solutions.

Altogether, the dynamics of the current perturbation $I_n(t)$ is fully determined by the solutions of (2.59) – which is often referred to as *dispersion relation* as it links the harmonic number of the perturbation n to its complex frequency p – and its properties of being

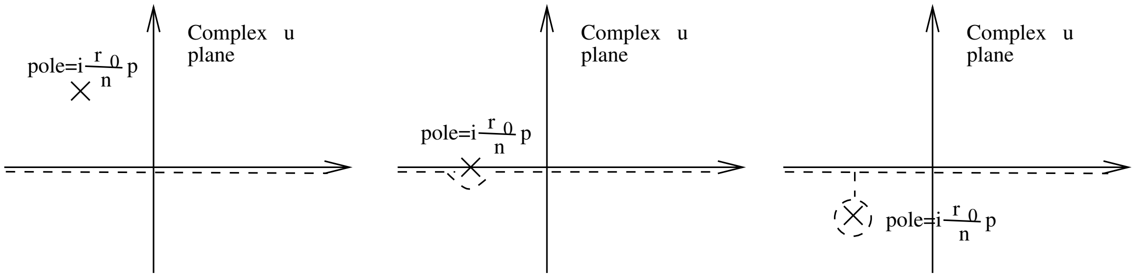

Figure 2.10: Landau path for the evaluation of the dispersion integral in (2.59) (dashed line – it depends on the location of the pole in the complex plane).

stable or unstable only depend upon the sign of the real part of these solutions. If there exists one single pole having a positive real part, then the n-th harmonic perturbation is expected to grow unstable. And besides, these poles always appear in couples and generally have a non-zero imaginary part, this meaning that there are at least a couple of waves propagating along the beam, one of which (always the "slow" one indeed, namely the one with a negative frequency shift) can be unstable. In most books and references, the dispersion relation is obtained from a kind of Fourier analysis and consequently one finds $\mathrm{i}\omega$ instead of p. It is clear that in this case the condition of instability will be given by $\mathrm{Im}(\omega) < 0$. Anyhow, the physical content of the derivation is of course no different, and besides, the rigorous mathematical approach given here has the advantage of thouroghly legitimating the Landau prescription for the evaluation of the integral in (2.59) (which would have otherwise required the use of different considerations to be explained [39]).
When solving the dispersion relation, one finds out that a finite region of the impedance plane exists, in which the beam is stable, and which is the smaller, the colder and the more intense the beam is. It is straightforward to prove that if we take into consideration a monochromatic beam, that is a beam with zero momentum spread – or, it would be a more correct definition, with zero revolution frequency spread[1] – this stability region shrinks down to a half imaginary axis and the beam will be expected to become unstable for any resistive impedance acting on it. The analytical formulae for the frequency shift and the instability growth rate can be easily evaluated starting from the dispersion relation (2.59) and using the distribution $f_0(u) = \delta(u)$ (the integration is carried out by parts, so that the derivative $\mathrm{d}f_0/\mathrm{d}u$ disappears):

$$
\begin{aligned}
\Delta\omega_{\mathrm{r}} &= \pm\omega_0 \left[\frac{1}{2\dot{Z}^*} \left(\sqrt{\mathrm{Re}[\dot{Z}]^2 + \mathrm{Im}[\dot{Z}]^2} - \mathrm{Im}[\dot{Z}] \right) \right] \\
\Delta\omega_{\mathrm{i}} &= \pm\omega_0 \left[\frac{1}{2\dot{Z}^*} \left(\sqrt{\mathrm{Re}[\dot{Z}]^2 + \mathrm{Im}[\dot{Z}]^2} + \mathrm{Im}[\dot{Z}] \right) \right]
\end{aligned} \tag{2.60}
$$

$$
\text{with} \qquad \dot{Z}^* = \frac{2\pi m^* \beta_0^2 \mathrm{c}^2}{q n I_0} \quad .
$$

[1]A beam with zero revolution frequency spread can be obtained, in spite of its having a finite energy spread, by simply operating a ring at the transition point. Setting the beam energy equal to the transition energy of the machine, in fact, one makes the slip factor η vanish, and the revolution frequency spread of the beam goes to zero, too, because the effect of the different momenta of the particles is exactly compensated by the dispersion due to the different orbits that different particles follow. For some applications it is desirable to operate a storage ring in an *energy isochronous mode*, when the flight time of the circulating ions only depends on their mass-to-charge ratio. This allows, for instance, precise mass measurements by measuring the flight time of the ions for multiple turns using a special timing detector [18, 40].

These formulae can be useful as they give rough estimates of the instability rise time when the impedance acting on the beam is much larger than the stability region size. Nevertheless they can be sensibly improved if one considers the effects of the momentum spread at least at the first order, as will be shown later on in Section 6.2.

At any rate, the physical meaning of the existence of a wide stability region when the beam momentum spread is considered, is clear from the fact that, in the dispersion integral, the contribution of the residue in the pole must be accounted for (directly or separately added, as is prescripted by the Landau integration path in Fig. 2.10). This residue carries the slope of the velocity distribution function at the wave phase velocity, and thus represents a sort of kinetic wave-particle effect connected with the particles that travel with velocities in phase with the wave (for all the other particles it does not really matter, because the net effect of the wave sliding over them will however average to zero on reasonable time scales). As we know from the kinetic theory of plasmas [41], this might lead to collisionless damping of the self-induced wave, if the number of particles slightly quicker than the wave is larger than the number of those slightly slower. This statement can be proven just by making an energy balance [41, 42] and figuring out how in such a situation the beam absorbs energy from the wave and consequently the wave gets damped. The phenomenon is well-known as Landau damping and, of course, it requires the right slope of the velocity distribution function at the phase velocity of the wave in order to significantly affect the overall beam dynamics.

2.3.2 Normalization of the dispersion relation and use of the stability charts

Next step will be to bring the relation (2.59) into a dimensionless form, independent of beam and machine parameters. In order to achieve this, we need first of all to define new parameters and functions which allow extracting dimensionless groups. The velocity spread S might be thought of as related to the half width half maximum of the distribution function $f_0(u)$,

$$S = \delta u_{1/2} \ ,$$

or to its standard deviation:

$$S = \delta u_\sigma \qquad \text{with} \qquad \delta u_\sigma = \left(\int_{-\infty}^{\infty} u^2 f_0(u)\, \mathrm{d}u \right)^{1/2}$$

Moreover we introduce the dimensionless variables

$$x = u/S \quad \text{and} \quad y = \frac{\mathrm{i}pR_o}{nS} \ ,$$

and the dimensionless function

$$G(x) = \frac{2\pi S R_0 f_0(xS)}{N} \ , \tag{2.61}$$

N being the total number of particles circulating in the machine (it is necessary to divide by N in order that the new defined function satisfies the condition of integral along the real axis equal to one).
After introducing a dispersion integral,

$$I_\mathrm{D}(y) \stackrel{\mathrm{def}}{=} -\mathrm{i} \int_L \frac{1}{y-x} \frac{\mathrm{d}G}{\mathrm{d}x}\, \mathrm{d}x \ , \tag{2.62}$$

and the complex number

$$T(n) = U + \mathrm{i}V = \frac{qI_0\dot{Z}_{\mathrm{tot}}(n\omega_0)}{2\pi m^*\beta_0^2 c^2\eta^2 n(\delta p/p_0)^2} \,, \tag{2.63}$$

the dispersion relation may be immediately re-written in the more compact form:

$$-T(n)I_{\mathrm{D}}(y)\mathrm{sign}(\eta) = 1 \,, \tag{2.64}$$

which becomes, when the beam is below transition energy:

$$T(n)I_{\mathrm{D}}(y) = 1 \quad \text{or} \quad U + \mathrm{i}V = \frac{1}{I_{\mathrm{D}}(y_{\mathrm{r}} + \mathrm{i}y_{\mathrm{i}})} \,. \tag{2.65}$$

What we finally reach in this model is therefore a complex function of a complex variable, which is analytic and thus represents a conformal mapping of the complex plane $y = y_{\mathrm{r}} + \mathrm{i}y_{\mathrm{i}}$ in the plane $T = U + \mathrm{i}V$ [6]. Given n, we can plot in the plane T the two families of curves corresponding to y_{r} =const. and y_{i} =const., so that for known beam and machine parameters one can determine a point in the plane $T = U + \mathrm{i}V$, the so-called *working point*, and figure out whether the beam is to be expected to be stable (the working point lies in a region entirely covered by curves with $y_{\mathrm{i}} < 0$, i.e. the *stability region*) or unstable (the working point lies on a curve with $y_{\mathrm{i}} > 0$ and in this case an initial perturbation would grow in time and lead to self-bunching). The border between stable and unstable region is the curve with $y_{\mathrm{i}} = 0$, which is therefore defined *stability boundary* and strongly depends on the actual distribution of the beam in the velocity space. In Fig. 2.11 Lorentzian, Gaussian and quartic distribution functions are plotted along with their corresponding stability boundaries in the (U, V) plane. For what we have stated in the previous subsection, it is clear that a higher number of particles that populate the tails of the distribution function tends to enhance the stability region because there are more particles involved in the Landau damping process: the result is that the curves $y_{\mathrm{i}} = 0$ tend to open in their upper part towards the region of capacitive-dominated impedances and the stability region will in fact enclose a bigger area. A drastic reduction of the size of the stability region occurs when the velocity distribution function is not single-peaked but has got bumps, dips, or is multi-stream. This is due to the fact that such a structure of the distribution function does not allow Landau damping for a more or less wide set of wave phase velocities. Figure 2.12 shows for instance a Gaussian distribution with a dip and the relative stability boundary: the stability region is only limited to the inner part of the small loop that surrounds the origin, as the rest of the “onion” is filled by the instability curves that curl around the origin, too, but in bigger turns.

When an instability is predicted because of a working point lying outside the stability region, it is possible to evaluate from the y_r-y_i charts both the frequency shift and the rise time of the unstable wave:

$$\Delta\omega_{\mathrm{r}} = \frac{nS\mathrm{Re}(y)}{R_0} = \frac{nSy_{\mathrm{r}}}{R_0} \tag{2.66}$$

$$\Delta\omega_{\mathrm{i}} = \frac{nS\mathrm{Im}(y)}{R_0} = \frac{nSy_{\mathrm{i}}}{R_0} \Rightarrow \tau_{\mathrm{inst}} = \frac{1}{\Delta\omega_{\mathrm{i}}} \tag{2.67}$$

Stability boundary and some instability trajectories are plotted in Fig. 2.13 for a Gaussian distribution function.
In practice, it is customary to make use of an impedance plane rather than of the universal $T = U + \mathrm{i}V$. The working point is in this case the normalized impedance of the machine,

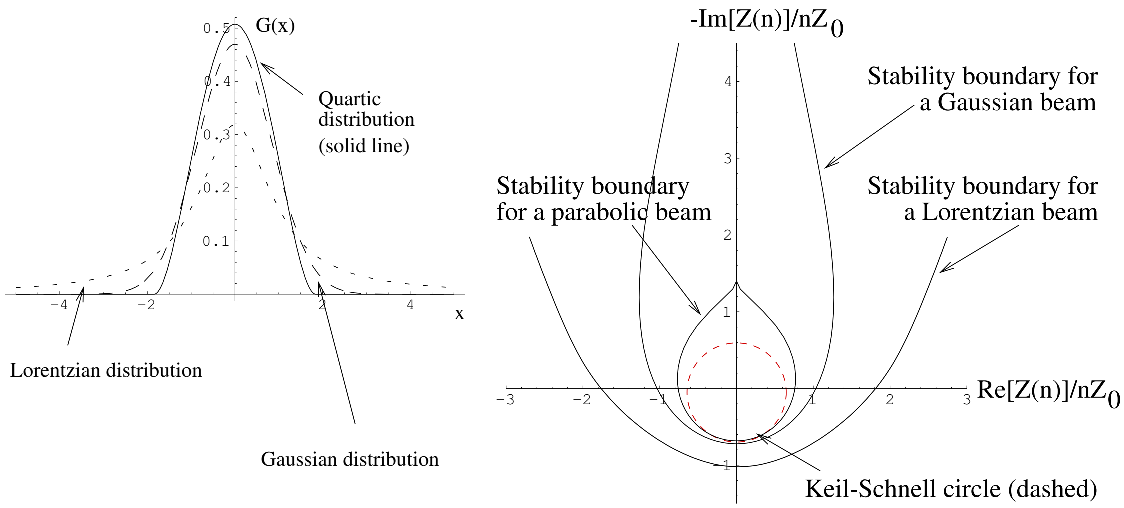

Figure 2.11: Different kinds of possible beam distribution functions and relative stability boundaries.

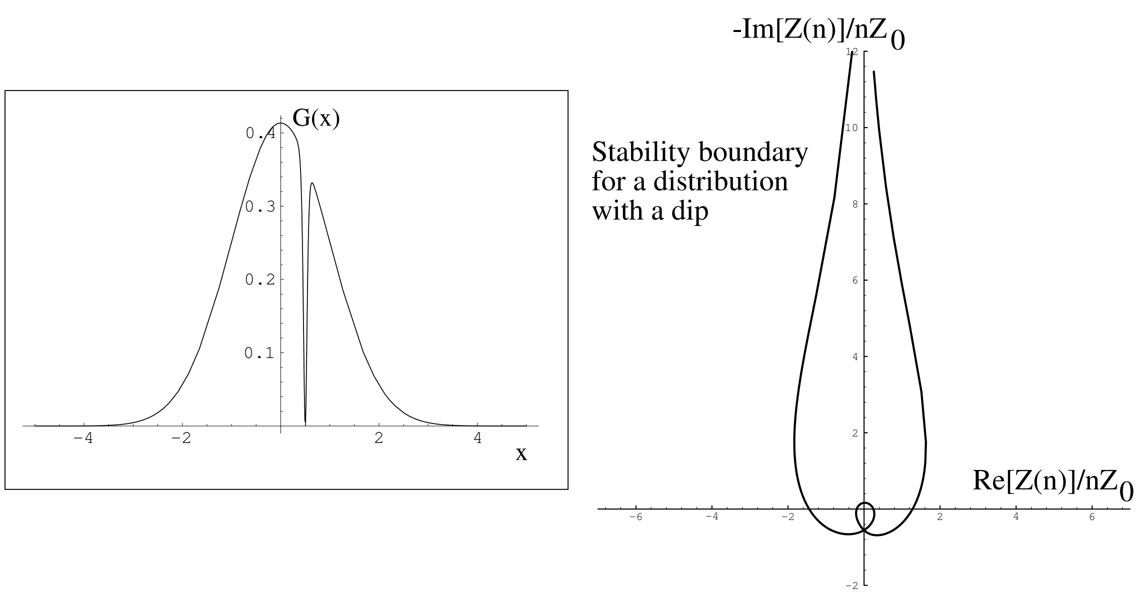

Figure 2.12: Velocity distribution with a dip and its stability boundary. The stability region shrinks to the small area enclosed in the loop about the origin in the normalized impedance plane.

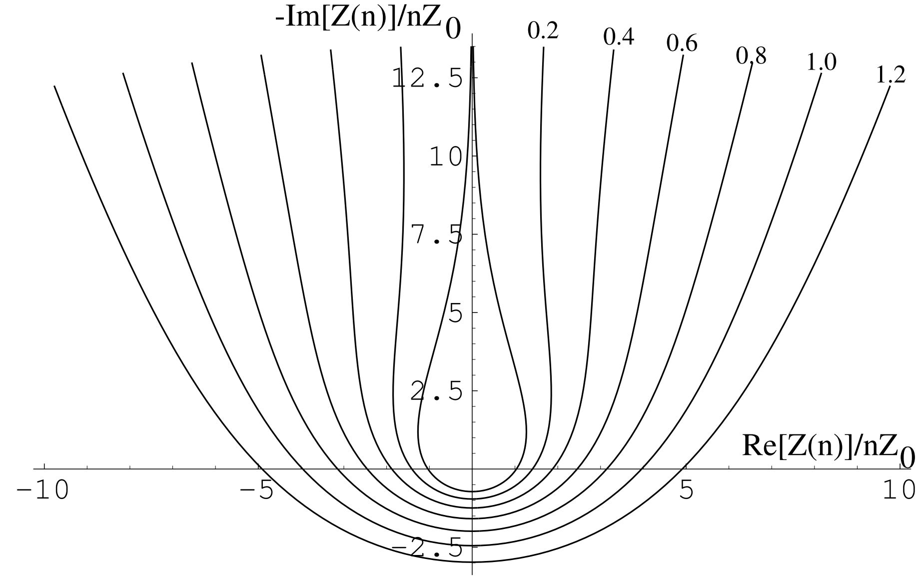

Figure 2.13: Stability boundary and unstable trajectories in the normalized impedance plane for a Gaussian velocity distribution function. From the numerical values which accompany each of the unstable curves, it is possible to figure out the rise time of the instability associated to a working point lying on that special curve (see Eq. (2.67)).

namely the ratio between the longitudinal coupling impedance and the harmonic number $(\dot{Z}_{\text{tot}}(n\omega_0)/n)$:

$$\dot{Z}_0 \cdot T(n) = \frac{\dot{Z}_{\text{tot}}(n\omega_0)}{n} \quad \text{with} \quad \dot{Z}_0 = \frac{2\pi m^* \beta_0^2 \mathrm{c}^2 \eta^2}{qI_0} \left(\frac{\delta p}{p_0}\right)^2 ,$$
$$\frac{\dot{Z}_{\text{tot}}(n\omega_0)}{n} = \dot{Z}_0 \frac{1}{I_{\text{D}}} . \tag{2.68}$$

The characteristic resistance $\dot{Z}_0$ may be evaluated from the beam parameters, as well as the curves y_{r} =const. and y_{i} =const. are known provided that the velocity distribution function of the beam is known. In order to investigate the stability of a coasting beam, all that one has to do is therefore to scale the plane $T = U + \mathrm{i}V$ with $\dot{Z}_0$, and then put in $\dot{Z}(n\omega_0)/n$ as working point. In many applications, the Keil-Schnell circle criterion [43] is widely used as an approximate check of the beam stability. This criterion requires that, in order for the beam to be stable, the inequality

$$\left(\frac{\delta p}{\bar{p}}\right)^2_{\text{HWHM}} > \frac{FqI_0}{4\beta_0^2\eta^2\gamma_0 m^* \mathrm{c}^2} \left|\frac{\dot{Z}_{\text{tot}}(n\omega_0)}{n}\right| \tag{2.69}$$

should be fulfilled. As we can see from Fig. 2.11, where the Keil-Schnell circle is plotted along with the actual stability boundaries for different distributions, the use of the inequality (2.69) might strongly underestimate the stability region of the beam, especially when the working point is strongly capacitive (maybe space charge dominated) and lies very close to the imaginary axis (very low resistive part). Therefore, beams which are expected to be unstable according to the Keil-Schnell criterion turn out to be stable because of Landau damping caused by the tail population. Experiments have clearly shown that the space charge impedance can exceed up to 10 times the Keil-Schnell critical impedance, without the beam becoming unstable as an effect [28, 30].

Chapter 3

Measurement of the longitudinal instability at the ESR

We have investigated experimentally the longitudinal instability of a coasting beam in the ESR far beyond the stability boundary and for several working points in the longitudinal impedances plane. The longitudinal coupling impedance was varied, in fact, by tuning the eigenfrequency of an ESR cavity to different values. For the eigenfrequency regulation a small RF cavity gap voltage was necessary throughout the whole measurement process. The development of special software analysis routines along with the appropriate choice of the sampling frequency for the beam current signal has enabled us to observe the beam dynamics up to 1000 ms with a much improved time resolution.
In this chapter the measurements are presented and the data acquisition is discussed. All experimental observations are carefully pointed out for a further, deeper understanding of the different phases in the evolution of an unstable beam.

3.1 Experimental and technical features for instability measurements

The ESR is a machine that gives unique possibilities to study coherent instabilities since very intense beams can be stored therein, and moreover their energy spreads and transverse emittances can be successfully decreased down to very low values employing the electron cooler which is along one of the long straight sections of the ring (see Sec. 2.1.2). For the first time in 1996, experiments were already successfully carried out in the ESR, which showed how a longitudinal instability could be driven in a very intense and cold beam – space charge dominated, one could say – by means of a cavity tuned in the vicinity of the second harmonic of the beam revolution frequency [28]. These measurements, which were made with Ca^{+20} and C^{+6} ion beams, allowed the observation of the transition from stability to instability, and were realized according to the following procedure:

phase 1: the beam was injected, stored and cooled via electron cooling while the RF cavity was kept strongly detuned.

phase 2: started with turning off the electron cooler and simultaneously shifting of the RF cavity eigenfrequency to the double of the beam revolution frequency, or neighboring values.

Provided that the cooling in phase 1 was sufficiently good (one had to be able to observe the double-peaked Schottky spectrum, indicating the achievement of a very high phase space density and a large space charge impedance acting on the beam), it was possible to observe the longitudinal instability excited by the resistive part of the impedance of the RF cavity (made sensibly different from zero in phase 2). The signal delivered by the beam to a pair of longitudinal pick-up electrodes is proportional to the beam current modulation: having monitored such a signal over some 200 ms, one could see the exponentially growing amplitude of the current modulation in the linear regime of the instability with a rise time of roughly 20 ms, and the phase of nonlinear saturation. No long term evolution could be observed then. Besides, no satisfactory comparison with the linearized theory could be quantitatively drawn, because the cavity eigenfrequency was not precisely known. This caused the longitudinal coupling impedance to be unknown, as well.

Anyhow, the success of this first set of measurements in producing at the ESR a beam that did grow unstable over a reasonable time scale, has strongly encouraged setting up a second beam time dedicated to the longitudinal instability. Its main goal was supposed to be: taking and storing data over a longer time (up to 1 s for each unstable evolution thanks to the undersampling technique that will be explained later on), and moreover having a precise control of the cavity eigenfrequency for each of the working conditions in which the instability would be excited. The advantages coming from these two conditions are evident: first, a long observation time gives a clear picture of the nonlinear phase in the instability evolution and of all the related phenomena; secondly, the precise knowledge of the cavity eigenfrequency allows the evaluation of the impedance acting on the beam for each measurement, so that connections can be established between the different working points in the impedance diagrams and the linear as well as the nonlinear phases of the beam evolution.
Unfortunately, it was known from the beginning that the feedback controlling system for the cavity eigenfrequency would require the presence of a small residual voltage at the cavity gap, which would perhaps significantly influence the beam dynamics in some cases. The idea was to ignore anyway, in first approximation, the presence of this external electric field oscillating in the cavity, because it would be kept always quite strongly detuned with respect to the beam, and consequently would not be expected to sensibly change the charge line density. This point will be widely discussed in the next chapter (Secs. 5.3 and 5.4), where analytical and numerical results concerning the dynamics of a beam under the action of self-fields and a residual voltage are presented. There it will become clear up to which extent to ignore the small finite voltage can be considered a good approximation, and when, on the other hand, severe changes must be expected in the instability evolution because of its presence.
Preliminary calculations based on the linear theory of the instabilities showed that, if the beam delivered to the ESR for these measurements had been C^{+6} at 340 MeV/u with a current spanning from few tenths of mA to some mA and a momentum spread of the order of 10^{-6}, an instability on the first harmonic would appear and grow the quicker, the closer the cavity eigenfrequency would be tuned to the beam revolution frequency. The growth times required for the experiment to deliver reliable results should be in the few tens milliseconds region, such that:

1. the instability could be considered not to be significantly affected by the electron cooling, at least in its linear phase (characteristic cooling time is some hundreds of milliseconds).

2. the instability would be also slow enough that the ramping time of the cavity (15 ms) could be neglected for its development from the eventual working point.

For a favorable data acquisition, it was evident that a traditional sampling technique could not be chosen, or else this would have required an amount of data to store so large, that it would have become impossible to follow the beam evolution over a period as long as 1 s. As a matter of fact, a C^{+6} beam at 340 MeV/u in the ESR has a revolution frequency of 1.886633 MHz: this means, if we had wanted to resolve one lap with some 100 samples in order to have a resolution up to the 50th harmonic – which is not much, anyway, but large enough for our purpose to excite an instability on the first harmonic – the acquisition of 188.6 Megasamples for each 1 s beam evolution would have been needed. Considering that the measurement was to be repeated for at least 10 different working conditions, the amount of data eventually stored would have grown really huge (using a 8 bit precision, a minimum of nearly 2 Gbyte only on this experiment). So, the idea has been used to undersample our current signal at 2 MHz (even below the Nyquist minimum frequency for the reconstruction of the signal, which is twice the frequency of the signal [44]); this technique utilizes samples from subsequent turns in order to reconstruct the wave form over one turn, and is expected to work without loss of information because the beam profile does not change much over several hundreds turns due to:

- The momentum spread is very small, corresponding to a velocity spread in the order of 500 m/s. After 100 turns, the quickest particles will have moved about 60 mm in the longitudinal direction, which is negligible with respect to the 108 m circumference of the ESR, and does not cause a sensible variation of the beam line density.
- With a period $T_0 = 0.53\,\mu$s, 100 turns correspond to about 0.053 ms. Thus, the dynamics of the slow unstable wave can be still correctly resolved, as it must have a time scale of the order of tens of milliseconds.

In fact, it is pretty straightforward to figure out that sampling the signal at 2 MHz, 17.64 data samples would be needed to resolve one period. Of course this resolution, which would indeed be enough to analyze an instability rising on the first harmonic, prevents the observation of possible much higher harmonics generation, and moreover does not allow a very detailed reproduction of the bunch shape. That's why a special software analysis routine was developed (off-line) to "interleave" a series of $n \cdot 17$ consecutive data samples (each i-th series is then shifted by the fractional part of $i \cdot (1 - 0.64) = i \cdot 0.36$ samples during the interleave), such that the beam line density can be reconstructed with a very high time resolution of more than 100 MHz. The advantage of this method is that the beam signal could be taken over the long time interval of 1000 ms, by simultaneously giving the possibility to perform high accuracy zooms on the beam signal in the off-line analysis. With the "interleaving" procedure that guarantees high resolution even with a very low sampling frequency, the whole set of parameters, both concerning the physics of the experiment and its technical part, was eventually fixed. In the next section, the measurement process will be described in all details.

3.2 Measurement process

The longitudinal instability in the ESR was basically excited by varying the longitudinal coupling impedance of the ESR cavity and observing a longitudinal pick-up signal (Fig. 3.1). The total impedance acting on the beam consists of a real part, which is mainly the resistive part of the cavity impedance, and an imaginary part, which is given by the sum of the imaginary part of the cavity impedance and the space charge reactance ($\approx -700\,\Omega$ per harmonic) from the beam itself [35, 30].
After injection of about $300\,\mu$A C^{6+} ions ($E_{\rm kin} = 340$ MeV/u) we decreased the beam

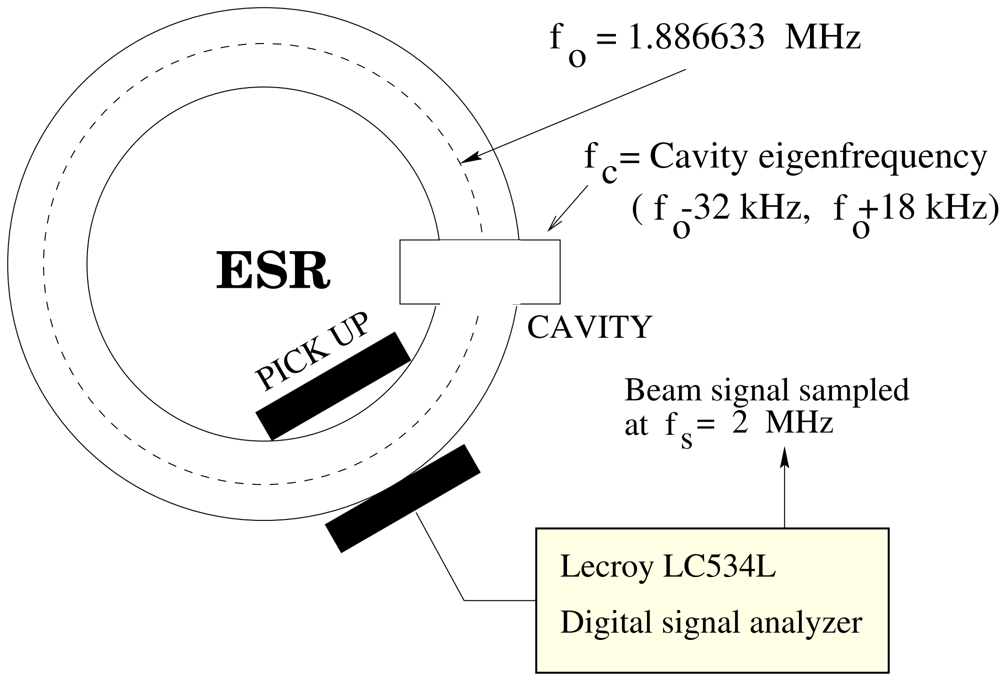

Figure 3.1: Scheme of the experiment performed at the ESR.

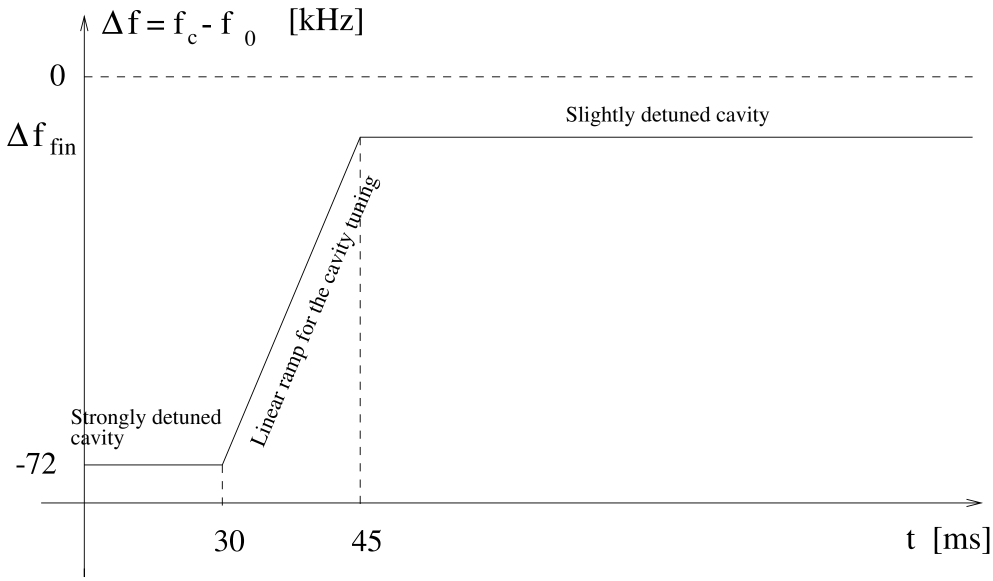

Figure 3.2: Measurement process.

momentum spread using the ESR electron cooler, which was optimized for longitudinal cooling. Simultaneous transverse heating minimized intra-beam scattering effects and enhanced the longitudinal cooler efficiency [45]. For the very cold beam the longitudinal Schottky spectrum is strongly deformed (Fig. 2.4). Nevertheless the momentum spread can be calculated from the deformation of the spectrum [46]. During the cooling process the eigenfrequency of the cavity was kept detuned $|\Delta f| \approx 70$ kHz away from the beam first harmonic, $f_0 = 1.886633$ MHz. After an equilibrium momentum spread of

$(\Delta p/p_0)_{\mathrm{FWHM}} = 1.1 \cdot 10^{-5}$ had been reached and the beam had been observed to be stable in this situation of detuned cavity, the eigenfrequency of the ESR cavity was tuned close to the revolution frequency of the beam by a linear (in time) frequency ramp within 15 ms (Fig. 3.2). The difference between the beam revolution frequency and the cavity eigenfrequency, $\Delta f = f_0 - f_{\mathrm{r}}$, determines the impedance acting on the beam (following the cavity resonance curve, Fig. 2.7). The ESR cavity has a quality factor of $Q \approx 50$ and a shunt impedance of about $R_{\mathrm{s}} \approx 1.3\,\mathrm{k}\Omega$ [35]. As was already pointed out, the eigenfrequency regulation system requires a finite RF voltage of 320 V at the cavity gap, which was continuously present during the measurements.

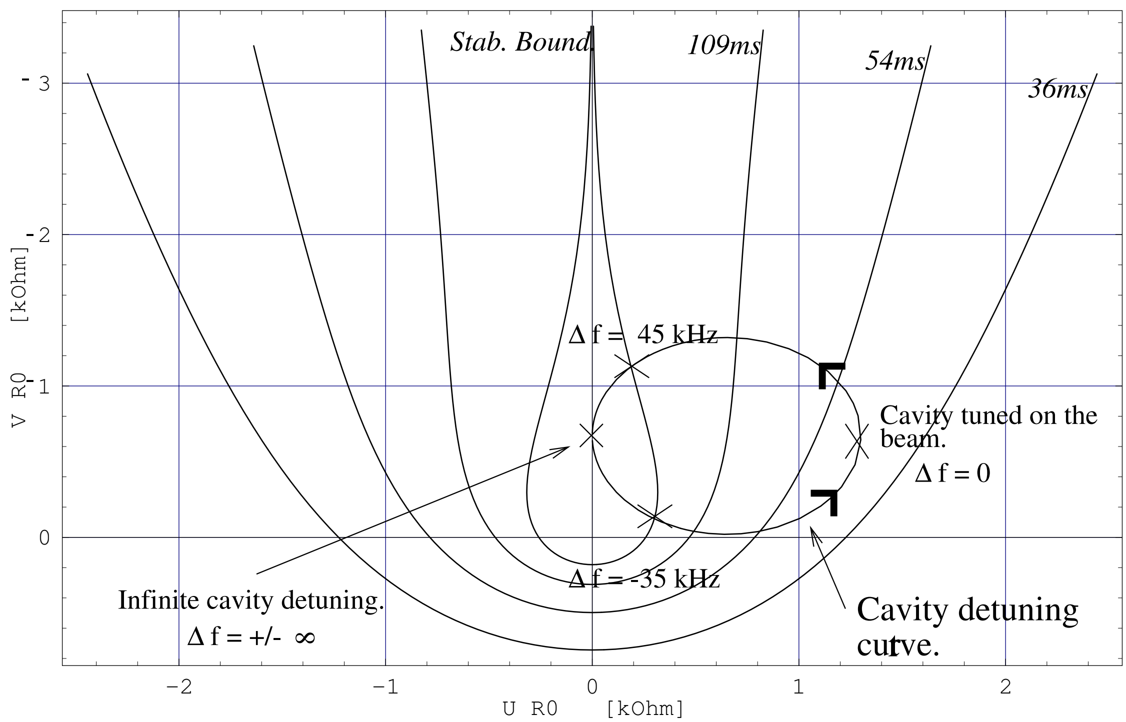

Figure 3.3: Impedances diagram for the ESR measurements. The cavity detuning curve is drawn according to the shown direction as Δf spans between $-\infty$ and ∞.

For the interpretation of the measurements, we plot the cavity detuning curve on the stability diagram of the longitudinal instability in the complex impedance plane [6]. The beam is unstable outside the onion-shaped stability boundary of a Gaussian distribution (Fig. 3.3). When the cavity eigenfrequency is brought sufficiently close to the beam revolution frequency, the impedance working point in the longitudinal stability diagram ends up far outside the stability boundary and the beam becomes unstable. The longitudinal beam signal was then measured over about 1000 ms by sampling the signal of a longitudinal beam monitor at 2 MHz using the digital signal analyzer LeCroy LC534L. Fig. 3.4a shows the measured beam envelope for a small eigenfrequency detuning of $\Delta f = -2$ kHz, which corresponds to a large cavity coupling impedance of about $(1285 + \mathrm{i}136\,)\Omega$. The eigenfrequency ramp starts at $t = 30$ ms and lasts 15 ms; so we observe that, within 5 ms after completion of the ramp, the beam gets quickly unstable. In Fig. 3.4b the cavity eigenfrequency was detuned by $\Delta f = -17.4$ kHz, with a corresponding cavity impedance of $(700.3 + \mathrm{i}648\,)\Omega$, causing therefore an instability that shows up far later and with a

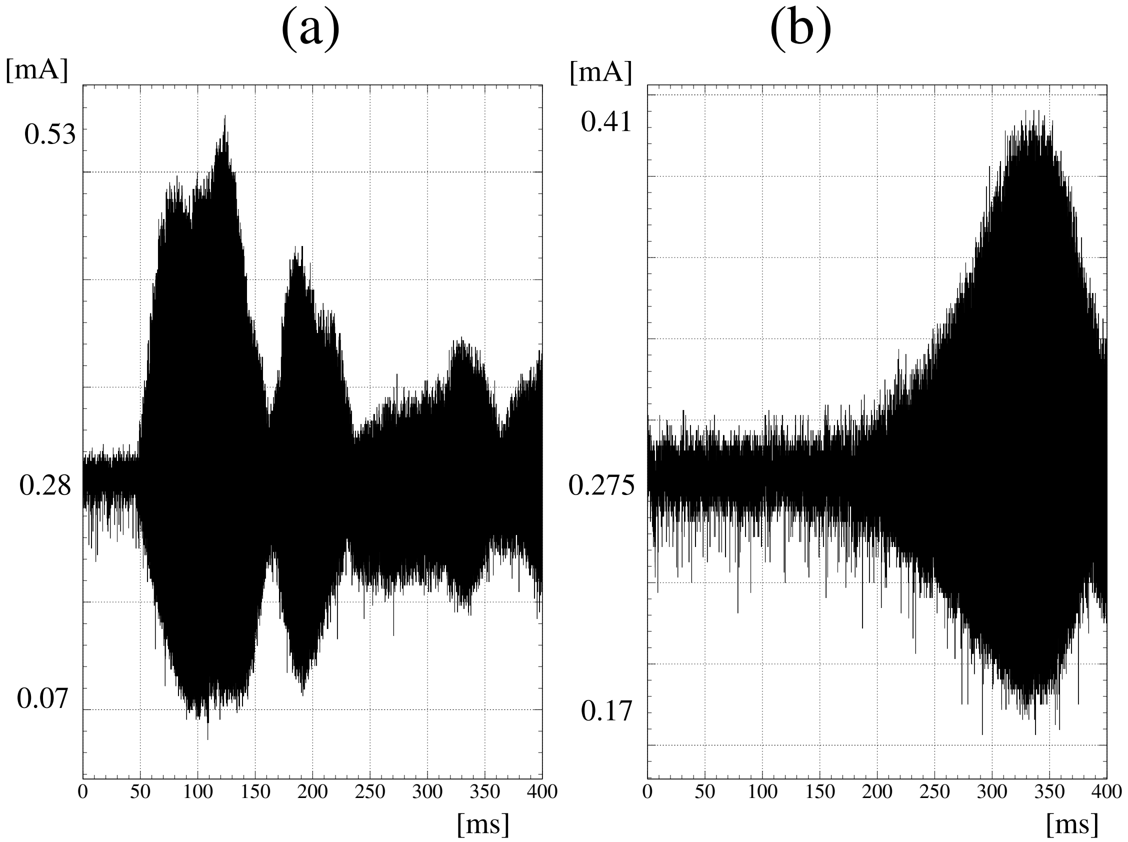

Figure 3.4: Beam envelopes up to 400 ms for $\Delta f_{\mathrm{fin}} = -2$ kHz (a) and for $\Delta f_{\mathrm{fin}} = -17.4$ kHz (b). The cavity eigenfrequency gets tuned to Δf_{fin} during the time interval $30 - 45$ ms.

much longer rise time.

3.3 Experimental observations during the unstable evolution of the beam

The analytical theory predicts that due to the positive resistive cavity impedance the longitudinal instability arises on the slow wave, which corresponds to the plasma wave running backwards in the beam frame. This may be seen in Figs. 3.5a and 3.5b. In these two pictures the beam evolution is represented in form of the so-called waterfall diagrams: that is to say, the line density of the beam along the ring (here an azimuthal coordinate θ is chosen for that) is plotted in several instants, and the time difference between two subsequent traces is a multiple of the revolution frequency of the beam (actually, it is a multiple of $f_{\mathrm{r}} - f_0$, with f_{r} sampling frequency of the signal, because one of the effects of the undersampling is the reconstruction of the signal in low frequency). In Fig. 3.5a the beam modulation splits up into a higher harmonic order oscillation from $t = 200$ ms. If the cavity eigenfrequency was tuned close to the beam, we observed in almost all measurements that the beam does not stay unstable just on the first harmonic, but gets also excited at much higher harmonics. The frequencies that correspond to these instabilities reach up to 40 MHz (they arise at 190 ms in Fig. 3.5a). It is well-known that the ESR injection kicker has several resonances in this frequency region [47]. All beam modulations that appear at frequencies different from the fundamental mode are due to nonlinear effects in the instability dynamics, since they are absent if the fundamental mode is stable. The mechanism of these nonlinearities will be widely discussed throughout the next chapters.

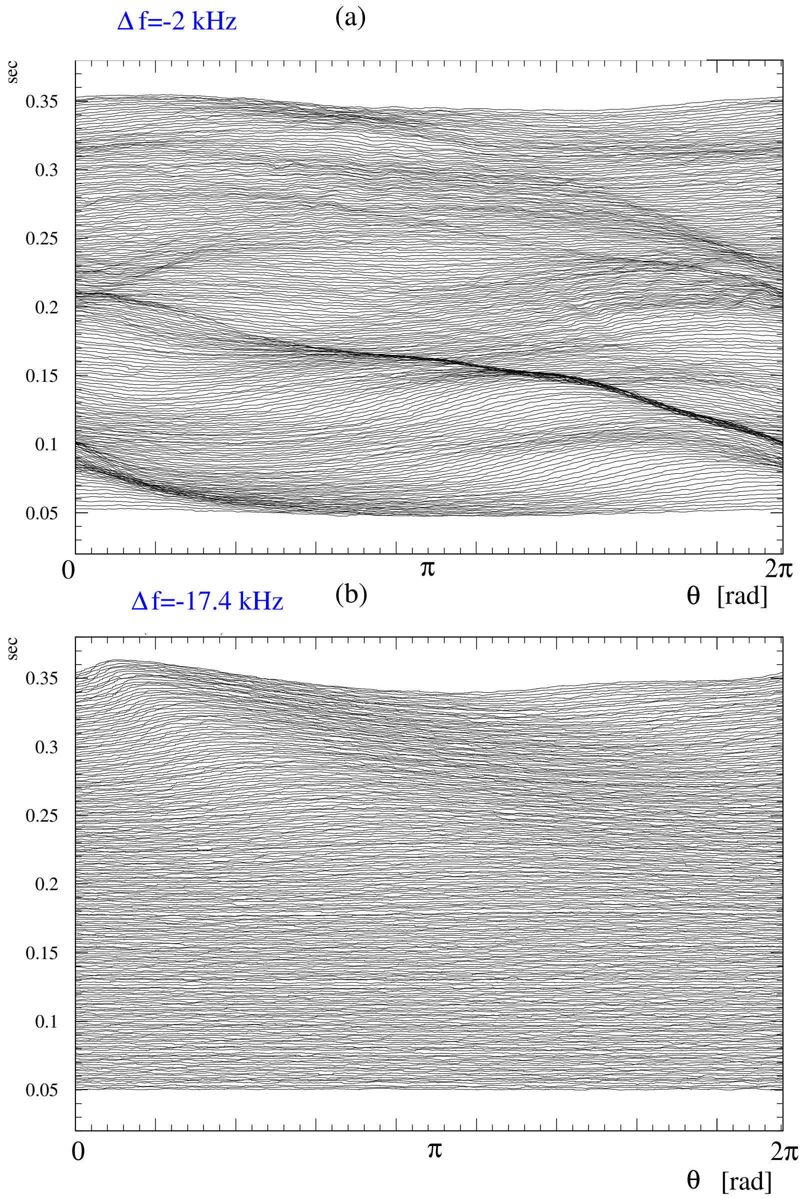

Figure 3.5: Waterfall diagrams for the two cases in Fig. 3.4. Here the beam line density traces along the ring are plotted over one another at several instants in the interval 50–350 ms.

We studied the modulation signal of different measurements (with different coupling impedances). At the early stage of the instability we always observed symmetric sinusoidal modulation signals growing in amplitude (Fig. 3.6a and 3.6b), whereas in the nonlinear region asymmetric bunch shapes occurred (Fig. 3.6c), and sometimes triangular later on. The wave front steepening (Fig. 3.6c) is a common feature of waves in nonlinear regime [42] (see also Chapter 6). As expected due to our "undersampled" data, in the measured

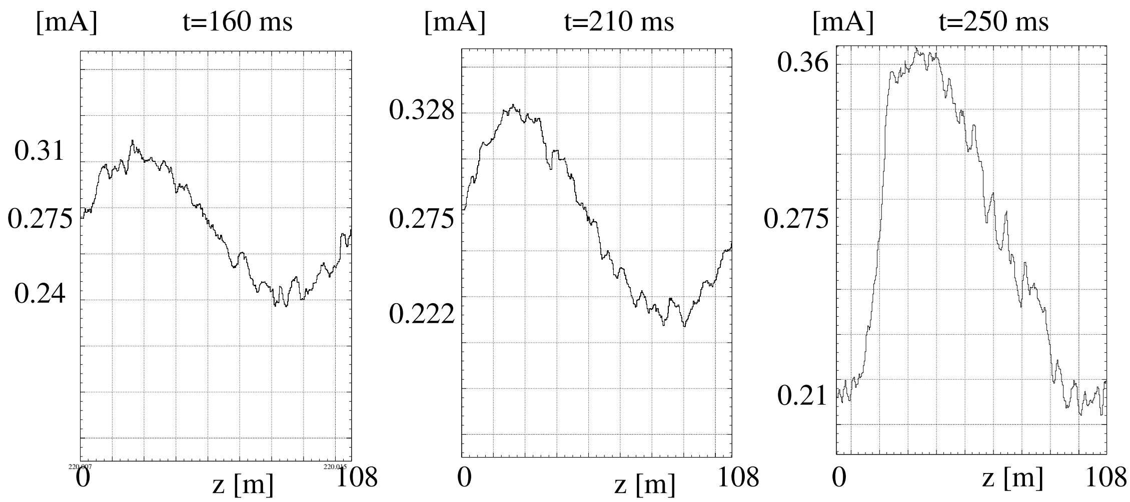

Figure 3.6: $\Delta f_{\text{fin}} = -17.4$ kHz: sinusoidal bunch shapes occurring in the linear phase of the instability (first two pictures) and steepened wave front at the time of maximum amplitude (third picture).

bunch signal the large slope appears at an earlier time. After steepening, the unstable wave always reached its saturation level. From this point on, a residual coherence could be in all cases observed to persist on the beam, oscillating some times in a sort of recurrent fashion. This is clear both in the envelope and waterfall diagrams of Figs. 3.7 and 3.8. This means that even after saturation, the beam structure never goes back to the pure coasting beam, constant along the longitudinal direction and smooth in the velocity space, but stays coherent. This subject will be reconsidered in Chapter 8, where a comparison with long term simulations is drawn and widely discussed.

In fact, it is this coherent long-lived structure of the beam line density that does not allow applying the methods of the Schottky diagnosis anymore on a beam which has undergone a longitudinal instability at some point in its history. Actually, this is the main reason why from these data we cannot extract information about the evolution of the beam in the velocity space. For the purpose, simulations will be of much help, and also recently new forms of investigation always using Fourier analysis are being under study in order to be able to get this kind of useful insight when analyzing beam instabilities.

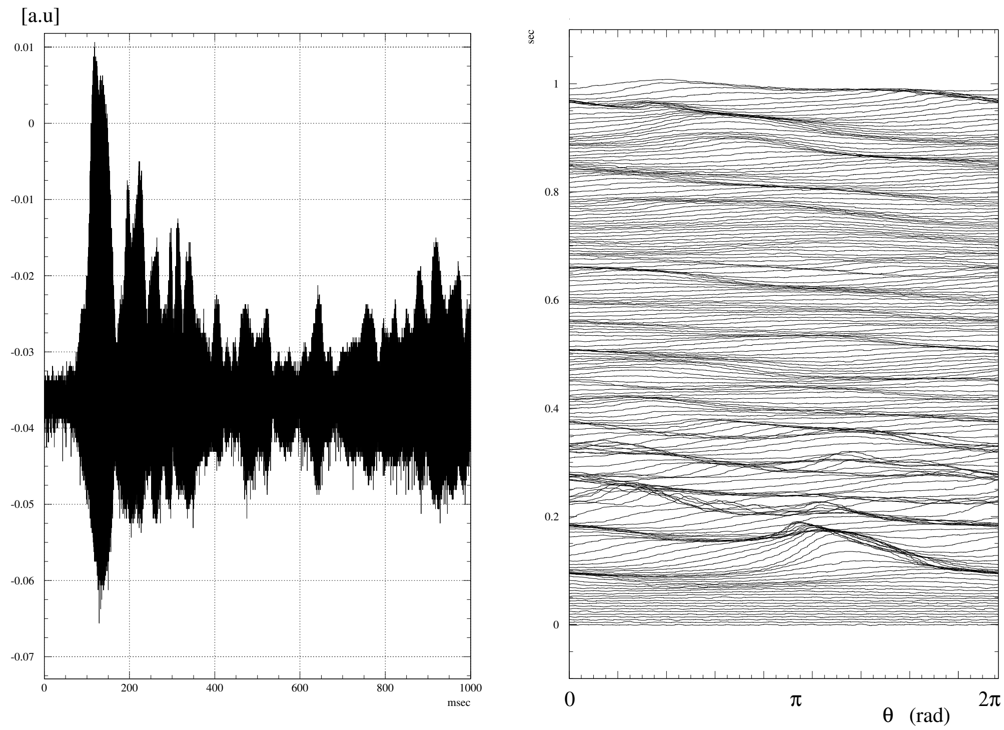

Figure 3.7: Beam current evolution over 1 s (current modulation envelope on the left side and waterfall diagram on the right side) for the case $\Delta f = 6.7$ kHz.

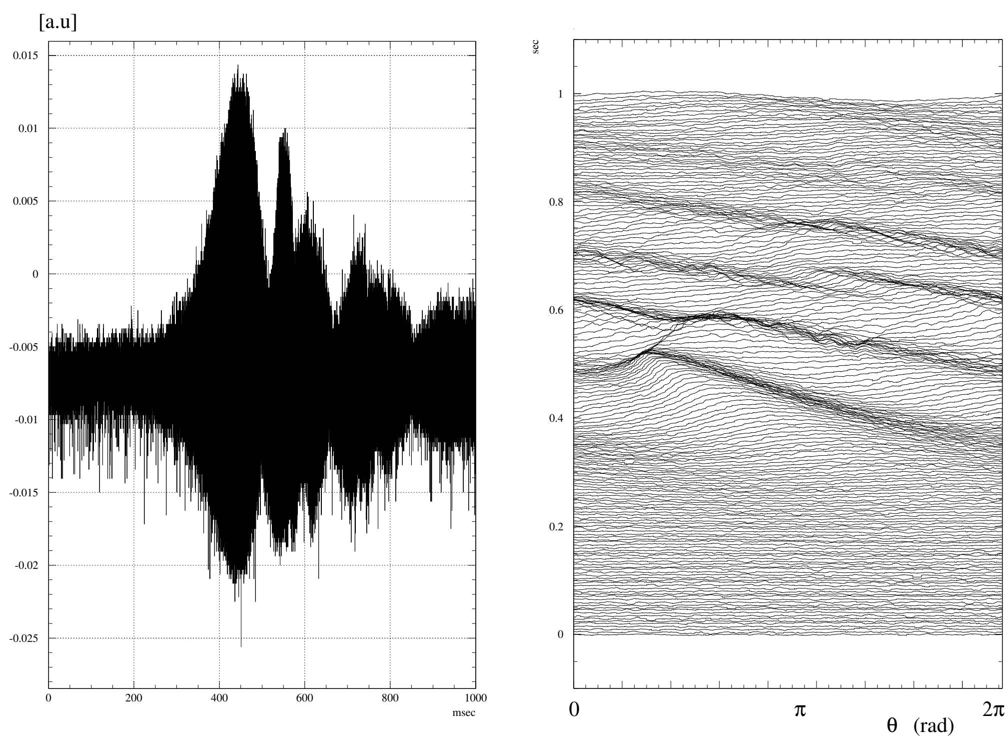

Figure 3.8: Beam current evolution over 1 s (current modulation envelope on the left side and waterfall diagram on the right side) for the case $\Delta f = -13.8$ kHz.

Chapter 4

Interpretation of the linear phase

By using the linear kinetic theory and the particle-in-cell code PATRIC [48, 49], the longitudinal instability observed in the ESR has been investigated for different values of the longitudinal impedance of the machine. The numerical investigations show that initially the instability grows exponentially as predicted by the linear theory. Theoretical and measured instability rise times have been confronted with the simulated ones and a good accord between them is found. When the perturbation reaches large values, significant high order harmonics are produced: steepening of the density profile as well as saturation of the instability growth appear first, and turbulence later on. These phenomena will be object of a far more detailed analysis in the next chapters. Analytical and numerical studies with a small RF voltage applied at the detuned cavity gap have also been carried out in order to meet the conditions in which the actual measurements were made at the ESR.

4.1 The simulation program PATRIC

The code for beam simulation PATRIC (PArticle TRacing In Cell) [48] allows following the evolution of a given particle distribution in the phase space under the action of external as well as self-induced electric fields. In this context, as particle distribution in the phase space we simply mean an ensemble of discrete, point-like charges, whose number, order of charge and mass can be freely chosen, and whose motions are ruled by the laws of classical mechanics and electrodynamics. In order to be able to follow the dynamics of this ensemble, the code makes use of a discretized form of the equations of motion for the each particle. From the Vlasov equation written in the co-moving frame (2.50), it is possible to easily deduce the equations of the longitudinal motion, which can take into account both relativistic and frequency dispersion effects; moreover, the equations for the transverse dynamics that are employed in this description are quite straightforward as the motion is non-relativistic and assumed not to be coupled with the longitudinal degree of freedom. It is natural to use for the longitudinal motion the ion beam rest frame, because this introduces a strong simplification in the computation and has the advantage to show anyway all the phenomena in which we are interested.
PATRIC has been constructed in a severely modular fashion in such a way as to make it easier for the user to add new modules and integrate new functions. The parameters required for the beam simulations are entered through a configuration file, which is in ASCII format and is read by the code in the beginning of each simulation. All the dimensional quantities are required to be entered in SI-units, unless otherwise specified. The program is written in C-language and runs under the platform VMS.
The latest version of PATRIC has largely profited from all the work previously done

throughout the years. The routines for the calculation of the space charge distribution via the Area-Weighting method as well as the discretization of the equations of motion following the Leapfrog-method [50, 51], were first implemented in the SCOPRZ (Space Charge OPtics in RZ-geometry) code by I. Hofmann and I. Bozsic [49]. For the solution of the Poisson equation, the fast Poisson solver by U. Schumann and R. Sweet is employed [52]. The development of PATRIC in C-language has been subsequently made by G. Kalisch [35] and U. Oeftiger (smoothing of the fields for the reduction of the granularity noise, upgrade of the Area-weighting technique, etc.). As collective forces were already included in the capabilities of the code, for our study of the coasting beam instability, we have only needed to add the action of an external off-resonance voltage acting on the beam in order to better reproduce the conditions in which our measurements were taken.

4.1.1 Beam dynamics

PATRIC describes the motion of macro-particles in the ordinary six-dimensional phase space. The projections of this space on the corresponding two-dimensional subspaces define the longitudinal, horizontal and vertical phase planes.
The possible electric potentials considered are limited to the axially symmetrical case. The (transversely) azimuthal information is lost in this kind of representation, and that's why many times this model is referred to as a $2\frac{1}{2}$-dimensional model.

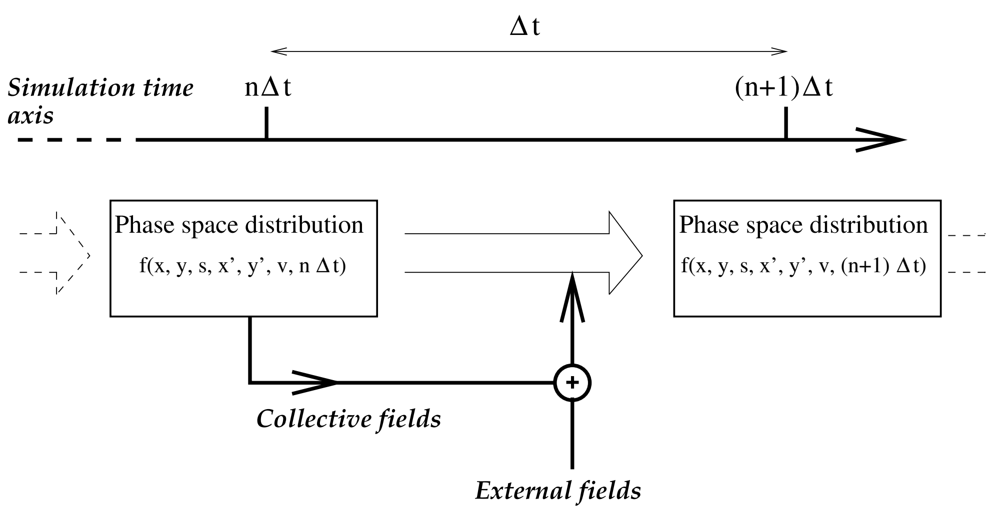

Figure 4.1: Principle of the numerical beam simulation along a discrete time axis. For each iteration step, the updated phase space distribution of the beam is constructed starting from the previous one and from the fields acting on the particles (a part of which might also depend on the particles distribution at the previous time step).

The simulation process goes through time steps of length Δt: the state of the beam at the time instant $t_{n+1} = t_n + \Delta t$ is iteratively computed from the output-state at the instant $t_n = n\Delta t$ (see Fig. 4.1). For each simulation step the electric fields are calculated at the grid points of an r-z net previously set, their values at the particles' actual locations are extrapolated by means of the Area-weighting method, and eventually the particles are accordingly moved after the principles of Newtonian mechanics. Longitudinally, the condition of periodicity in s of period $C_0 = 2\pi r_0$ is applied, whereas if a particle reaches

transversely to a bigger distance than r_{pipe}, it is considered lost (it hits the wall).
To solve the time and space discretized set of equations of motion

$$\begin{aligned}
\dot{x} &= v_x \quad ; \quad \dot{v}_x = -\frac{1}{m_I}\frac{\partial}{\partial x}(U_{\mathrm{ext}} + U_{\mathrm{coll}}) \\
\dot{y} &= v_y \quad ; \quad \dot{v}_y = -\frac{1}{m_I}\frac{\partial}{\partial y}(U_{\mathrm{ext}} + U_{\mathrm{coll}}) \quad , \\
\dot{s} &= v_s \quad ; \quad \dot{v}_s = -\frac{1}{m^*}\frac{\partial}{\partial s}(U_{\mathrm{ext}} + U_{\mathrm{coll}})
\end{aligned} \tag{4.1}$$

the well-know Leapfrog method is employed, which has the advantage of minimizing any artificial emittance growth. Positions and velocities of the macro-particles are herewith determined not at the same time instants, but shifted of $\Delta t/2$ [51].
The number of grid points can be freely chosen at the beginning of each simulation, such as to be adapted to the particular needs. The Area-weighting method is indeed used twice by PATRIC in each simulation step: first, in order to determine the space charge smooth distribution starting from the positions of the particles, and the second time when the electric fields, which are given at the grid points, have to be extrapolated back to the points where the particles stand [51].

4.1.2 External potentials

External fields are necessary for beam focusing. In real synchrotrons and storage rings, the beam is transversely focused by the action of quadrupolar fields which are ordered along the desired trajectory in an alternate fashion (as for the sign of the magnetic field gradients) so as to achieve horizontal as well as vertical focusing. In the PATRIC simulations, this real structure is neglected and the beam is continuously radially focused by the action of an ideal field having potential $U_{\mathrm{rad}} \propto r^2$ (smooth approximation [31]). Of course, this means that one has to give up any more detailed description of the effects of the real transverse dynamics, such as chromaticity or frequency dispersion. Only the global η effect is in any case taken into account in the longitudinal dynamics, thanks to our considering in the longitudinal equation of motion the effective mass of the ion m^* instead of its real relativistic mass.
For the longitudinal beam focusing, an RF electric field is required that oscillates on a multiple h of the revolution frequency of the beam (this harmonic number depends upon how many bunches must be kept orbiting in the ring). In real machines, this field is applied only at the cavity gap, but being the synchrotron frequency always by far smaller than the revolution frequency of the particles, one can make the approximation that the field is smeared all along the ring without committing major mistake. For the study of stationary bunches, originally only stationary sinusoidal fields were considered possibly acting on the beam (bunching fields causing no net beam acceleration). But since our problem required the study of the beam dynamics under the action of an off-frequency external field, too, the option to simulate a beam with a non-stationary electric field has been also added in the code. In our system co-moving with the particle beam, we have therefore in general a sinusoidal field

$$U_{\mathrm{long}} \propto \cos\left(\frac{h}{r_0}x - \Delta\omega\, t\right) \tag{4.2}$$

as function of the longitudinal "local" coordinate x and time t, its period being one single bucket length $2\pi r_0/h$.

4.1.3 Collective fields

The collective fields are used to model the totality of the interactions among beam particles, and of the beam particles with the surrounding environment (on a macroscopic scale, anyway, that is disregarding at this stage collisional effects). For this kind of study, the concept of impedance introduced in the previous chapters is of major help (Sec. 3.2.2). It can be naturally used, in fact, to calculate these self-induced fields, and subsequently have them act on the beam particles in order to determine their motion.

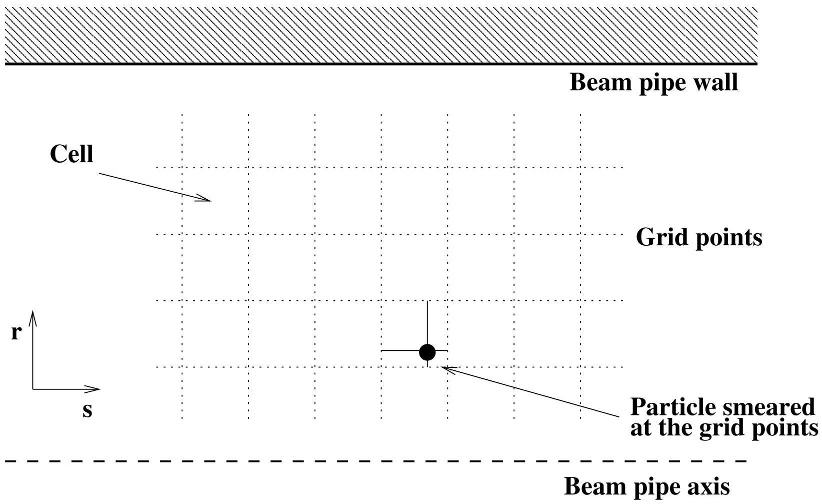

Figure 4.2: Here we see the partition of space in cells along the longitudinal direction. The contribution of each beam particle to the smooth charge density at the grid points is calculated according to the Area-weighting method, as well as the field evaluated at the grid points is extrapolated back at the particles location with the same procedure.

The space charge field indeed need not go through the computation via the impedance model, which would be correct only to some extent (see Sec. 3.2.3), but simply uses the potential that solves the Poisson equation for the given particles distribution, and therefrom derives the longitudinal electric field which acts back on the particles. After having determined the charge spatial distribution at the grid points with the method of the Area-weighting at each time step, the Poisson equation

$$\nabla^2 U_{\rm sc} = -\frac{\rho}{\epsilon_0} \tag{4.3}$$

is solved by a fast Poisson solver with the assumption of axisymmetric system inside a perfectly conducting cylindrical pipe [52]. The derivation of the field from the potential is then straightforward, and the last step consists in evaluating the field at the particle points from the one at the grid points – again with the method of the Area-weighting (Fig. 4.2).

For the interaction beam-cavity, which has been so far the one implemented in the code, the concept of impedance is employed. The beam current signal over one period is Fourier transformed with an FFT algorithm, and the harmonic component corresponding to the number on which (or in the vicinity of which) the cavity is supposed to be tuned, is multiplied by the cavity impedance. The resulting complex number gives amplitude and phase of the sinusoidal field acting back on the beam particles. In order to carry out this

computation, essential parameters like the cavity eigenfrequency, its shunt resistance and its quality factor, must be entered through the configuration file of the code.
For the beam diagnosis, observables like beam line density and velocity distribution are stored every m time steps, and eventually give a clear picture about the beam evolution over the pre-defined simulation time. An option for the Schottky analysis on the beam has been also set up, in order to be able to draw Schottky spectra from the simulations and try to gain a deeper insight into the method itself, which has been used so far mainly for diagnosis on stable coasting or bunched beams [32, 53].

4.2 PATRIC simulations of unstable coasting beams: comparison with the linear theory

In this section, the PATRIC code is used in order to simulate some unstable beam evolutions. First of all, the results of these simulations will be compared with the prediction of the well-known linear theory (see Chapter 3), and at the same time all the nonlinear featuring will be pointed out for deepening in the next couple of chapters. This is mainly done in order to show the excellent accord existing between theory and simulations in the ideal case, and consequently the reliability of the predictions from the PATRIC code in matter of beam instabilities. The unstable situations that we are going to consider in the following, directly come from the points experimentally investigated in the ESR. The only difference is that in this first approach we have reproduced ideal conditions in which the finite voltage at the cavity gap is ignored and the current has been assumed to be constant and equal to 0.366 mA for all simulation points (which was not the case during the measurements, when the current spanned between 0.27 mA to 0.36 mA). That's why now the only comparison will be drawn between theory and simulations, whereas in the next section, when the simulated dynamics is corrected to take into account the real conditions, experimental points will be also considered in the analysis.
Let's start with briefly summarizing the parameters for the simulations. The beam of C^{6+} ions at $E_{\mathrm{kin}} = 340$ MeV/u can be assumed Gaussian shaped in the velocity distribution, and the total impedance is changed by varying the RF cavity eigenfrequency f_{r} in a range of few tens of kHz in the neighborhood of the beam revolution frequency f_0. The beam and machine parameters are: $I_0 = 0.36$ mA, $f_0 = 1.886633$ MHz, $(\Delta p/p_0)_{\mathrm{FWHM}} = 1.1 \cdot 10^{-5}$, $\eta = -0.367$.
In the ESR the only significant contribution to the environment impedance comes from the space charge and the RF cavity [35]:

$$\dot{Z} = \dot{Z}_{\mathrm{sc}} + \dot{Z}_{\mathrm{cav}} \ ,$$

$$\dot{Z}_{\mathrm{sc}}(n\omega_0) = -\mathrm{i}nX_{\mathrm{sc}} \ ,$$

$$\dot{Z}_{\mathrm{cav}}(n\omega_0) = \frac{R_s}{1 + \mathrm{i}Q\left(\dfrac{n\omega_0}{\omega_{\mathrm{r}}} - \dfrac{\omega_{\mathrm{r}}}{n\omega_0}\right)} \ . \tag{4.4}$$

X_{sc} (space charge reactance of the beam) does not depend on the wave number n in the long wavelength limit - $n \ll (r_0/r_{\mathrm{b}})$, where r_{b} is the beam radius; R_{s}, Q and $\omega_{\mathrm{r}} = 2\pi f_{\mathrm{r}}$ are, respectively, the shunt resistance, the quality factor and the fundamental eigenfrequency of the RF cavity. For our analysis we assume the ESR values: $R_{\mathrm{s}} = 1.3$ kΩ, $Q = 50$ [35] and we set $X_{\mathrm{sc}} = 700\Omega$ [30].
The stability diagram and the cavity detuning curve that correspond to this situation are shown in Fig. 3.3. Since $Q \gg 1$ and the cavity is tuned in proximity of the beam revolution

frequency f_0, the contribution of the cavity impedance to the total machine impedance is negligible for $n \geq 2$. Thus, for $n \geq 2$, $\dot{Z}(n\omega_0)$ is purely capacitive and it is only due to space charge. For these perturbations the pair (R_0U, R_0V) corresponding to the total machine impedance lies always inside the stable area (the machine operates below the transition energy). As a consequence, all the perturbations with $n \geq 2$ are stable. Let us consider now the perturbation with $n = 1$. For $\Delta f < -35$ kHz and $\Delta f > 45$ kHz, where $\Delta f = f_0 - f_\mathrm{r}$ is the detuning frequency of the cavity, the working point again lies inside the stable area: in these conditions the first harmonic perturbation is stable too. On the other hand, for -35 kHz$< \Delta f < 45$ kHz the working point lies outside the stable area and thus the perturbation is expected to be exponentially unstable.
When the initial perturbation has grown to large values, the linear theory becomes inadequate. With PATRIC not only small perturbations can be studied, but also the evolution of the instability can be followed into its nonlinear region. Several different working points on the cavity detuning curve have been simulated. Fig. 4.3 shows the phase space plots, the line density profiles and the averaged (along the ring circumference) velocity distribution functions, for $\Delta f = -17.4$ kHz, when the longitudinal instability appears and develops in time.

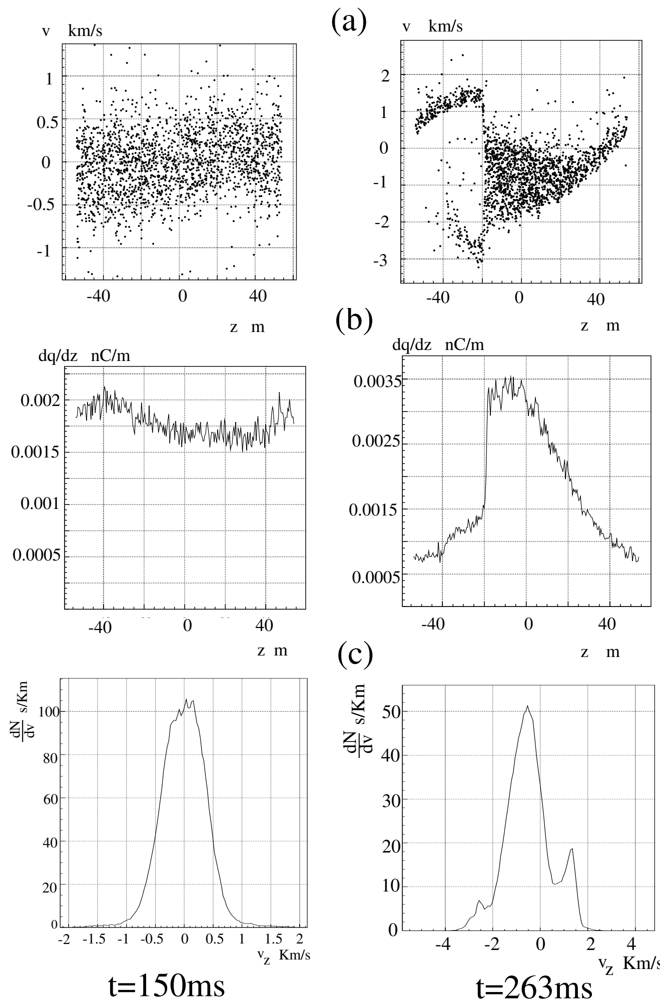

Figure 4.3: Numerical simulation for $\Delta f = -17.4$ kHz. Longitudinal phase space plots (a), line density profiles (b), and averaged velocity distribution functions (c), at $t = 150$ ms and $t = 263$ ms

In the first phase of the instability evolution (see $t = 150$ ms) the sinusoidal perturbation grows exponentially and propagates backwards, as predicted by the linear kinetic theory. When the perturbation amplitude has grown to large values, high order harmonics are produced, and saturation and wave steepening occur (see $t = 263$ ms). In particular in Fig. 4.4 the time evolution of the amplitude of the 1st, 2nd and 3rd spatial harmonics of the current and an exponential fitting of the first harmonic amplitude are represented. In the early phase of the instability the first harmonic amplitude grows exponentially. The rise time estimated in this way, roughly 45 ms, agrees very well with that obtained by using the impedance diagram.
In Fig. 4.5a the e-folding times $1/|\Delta\omega_{\mathrm{i}}|$ obtained from the linear kinetic theory are directly compared with those extrapolated from the simulations for different values of the detuning parameter Δf. In Fig. 4.5b the simulated and the theoretical slow wave frequency shifts $\Delta\omega_{\mathrm{r}}$ versus Δf are also plotted. As predicted by the linear theory the e-folding time $1/|\Delta\omega_{\mathrm{i}}|$ and the frequency shift $\Delta\omega_{\mathrm{r}}$ versus Δf curves are not symmetric with respect to the origin (the origin corresponds to a perfectly tuned cavity): for $\mathrm{Im}(\dot{Z}_{\mathrm{cav}}) > 0$ the rise time is lower and the wave is slower than for $\mathrm{Im}(\dot{Z}_{\mathrm{cav}}) < 0$.

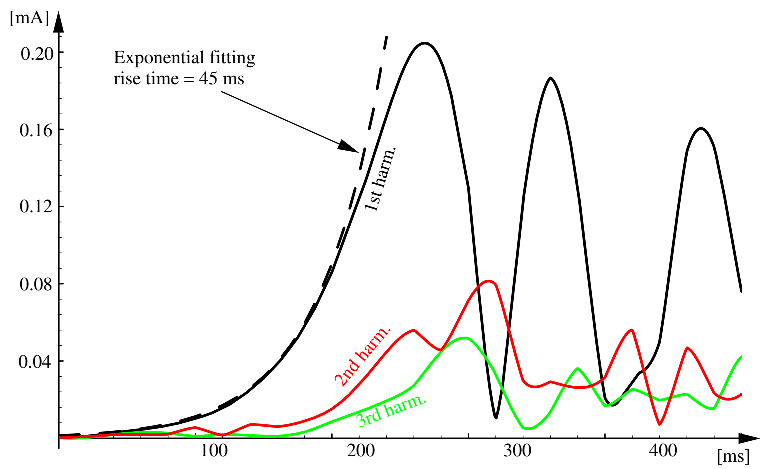

Figure 4.4: First, second and third current harmonic amplitudes versus time for $\Delta f = -17.4$ kHz.

From the simulation, it is evident that the first harmonic amplitude of the current grows exponentially (Fig. 4.4) and the averaged velocity distribution function does not show noteworthy changes (see $t = 150$ ms in Fig. 4.3c) as long as the second and third order harmonics stay negligible. The exponential growth of the first harmonic drives the growth of the higher order harmonics (Fig. 4.4) and the steepening of the wave front profile, which gives rise to a sharp gradient in the saturation phase of the instability (see $t = 263$ ms in Fig. 4.3b). The steepening of the wave front and the sharp gradient in the saturation phase have been clearly observed in the measurements in the ESR (cfr. previous chapter). From the phase space plot, it is also evident that in the saturation phase, the instability develops a bucket where most of the particles end up getting trapped (see $t = 263$ ms in Fig. 4.3a). As a consequence, the mean value of the corresponding averaged velocity distribution function decreases and the beam slows down, as well as the velocity spread increases (see $t = 263$ ms in Fig. 4.3c). Later on, the phase space distribution becomes turbulent.

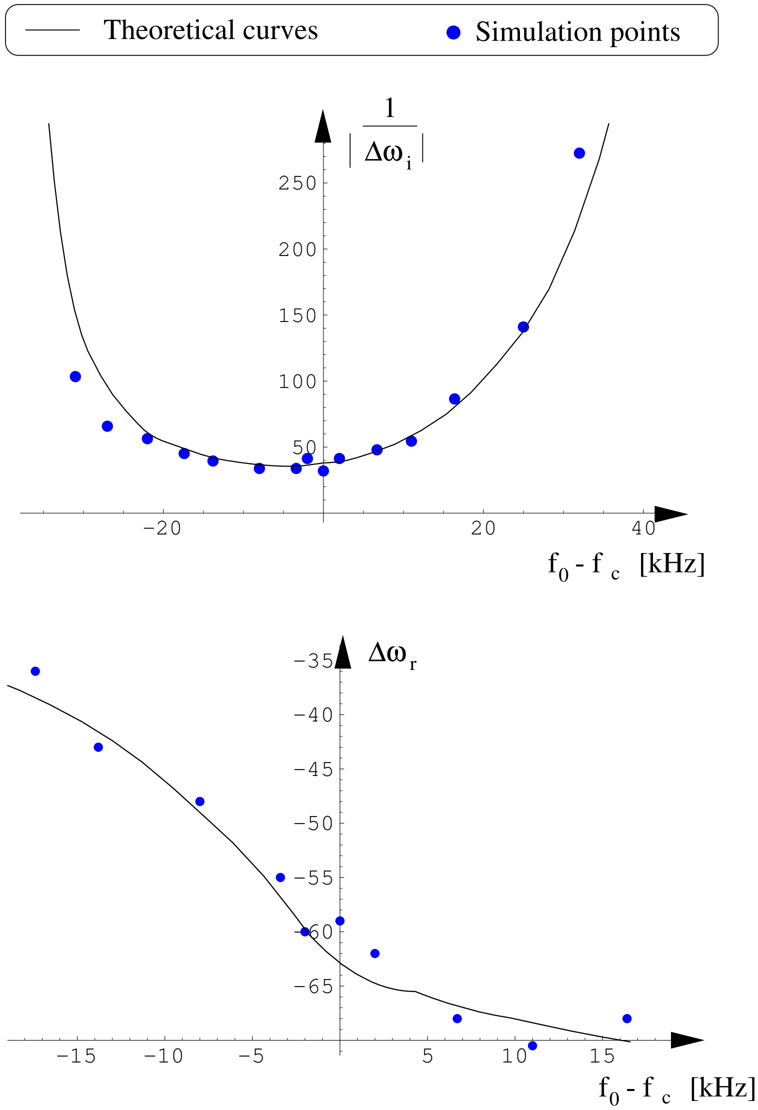

Figure 4.5: E-folding times $1/|\Delta\omega_{\rm i}|$ (a) and slow wave frequency shifts $\Delta\omega_{\rm r}$ (b) versus cavity detuning frequency Δf.

4.3 Beam simulations with an off-frequency voltage in the cavity

For a satisfactory comparison of the PATRIC results with the experimental observations at the ESR, we need to carry out the simulations including the external voltage for the cavity eigenfrequency feedback control, which was present during the measurements. But before that, it is useful to show how the comparison between theory and measurements would look like, if we applied the bare linear theory without taking into account the presence of the voltage in the cavity. Afterwards, we will go through a first correction to that by simply using the PATRIC code, which is able to simulate this extra-voltage, and in the next section a theoretical analysis of the full problem will be eventually attempted.

The rise times for the different measurements were extrapolated by means of a Fourier analysis on the beam current signal. As shown in Fig. 4.6, the interleaved beam signal over

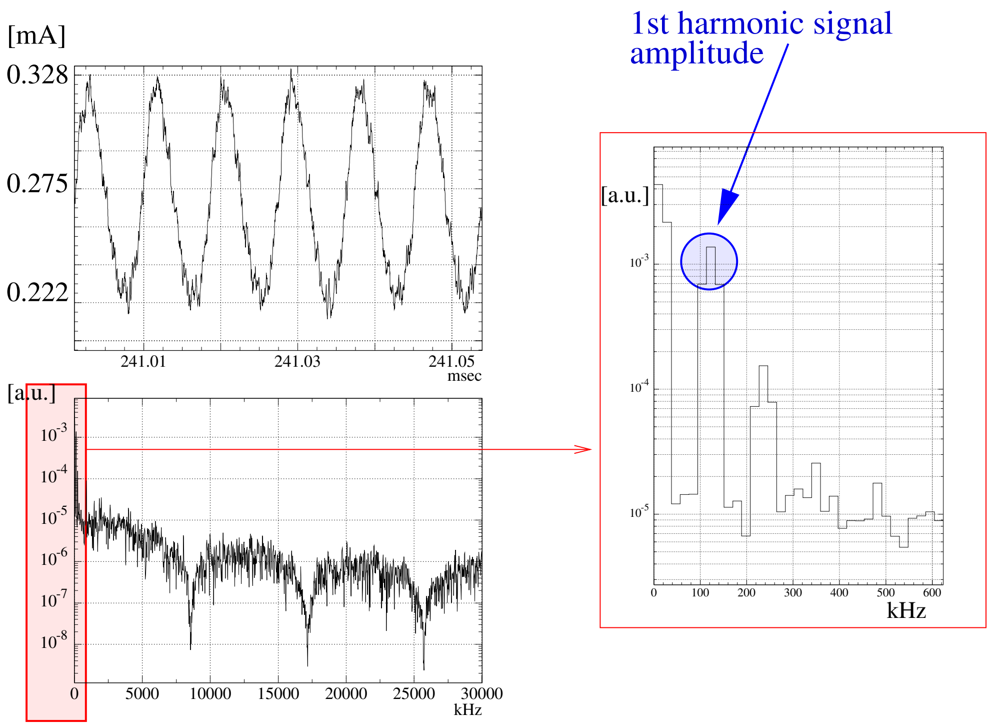

Figure 4.6: Rise time extrapolation from the experimental data. The first harmonic current component is extrapolated through a spectral analysis at many subsequent time instants. On the left, six periods of beam current and Fourier transform of this signal are represented; on the right, is the zoom of the beam current spectrum at very low frequencies, which allows the estimation of the first harmonic value.

6 periods was Fourier transformed via an FFT, and hence the beam first harmonic[1] could be evaluated at many subsequent time instants; from exponential interpolation of the beam first harmonic time profile, the growth times were calculated for all the measurements. As theory predicts, an asymmetry with respect to the sign of Δf was observed in the rise times of the instability. We evaluated the rise times from the early stage of the beam instability by performing an exponential fit through several beam modulation first harmonic signals analyzed at different time points of the beam evolution. In Fig. 4.7 we have plotted the measured rise times together with those predicted by the analytical theory of longitudinal instabilities, having assumed a Gaussian momentum distribution. There is a significant discrepancy with the theoretical predictions for the measurement results at very large detuning frequencies. Here the total impedance is very close to the stability boundary. In this region tiny deviations in the beam parameters (such as the actual beam momentum distribution) or slight inaccuracies in the impedance value (due for instance to a cavity quality factor Q not precisely known or to different contributions to the total impedance that had been neglected so far) strongly affect the predicted rise times and may even let a stable beam be expected unstable or vice versa. The measurement points for small cavity detuning frequencies are more reliable and show rise times around 20 ms. As seen in Fig. 4.7, the analytical theory predicts rise times that are larger for small detuning

[1] Actually, the 6th component of the spectrum had to be looked at, because of the choice of analyzing over 6 periods in order to make a better resolution between the dc component and the first harmonic in which we were interested.

frequencies, whereas there is better agreement a bit farther away from the center. Our computer simulation results suggest to explain this discrepancy by taking into account the finite cavity gap voltage of 320 V, which was needed for the eigenfrequency regulation system of the cavity.

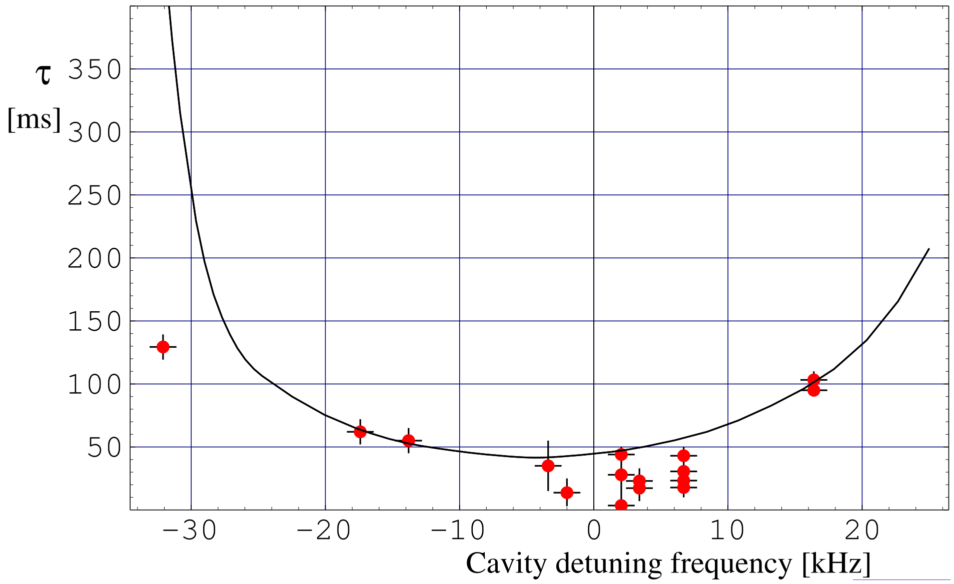

Figure 4.7: Measured rise times and comparison with the theory.

But for a fair check of the experimental results, we must necessarily employ the numerical approach with PATRIC. In fact, if with a small voltage at the cavity gap the analytical theory does not hold anymore, the PATRIC code is on the other hand able to simulate it. We have found out that for large detuning frequencies (few tens of kHz) the external voltage signal has little effect on the phase space distribution of the beam and almost no effect on the instability rise time. On the contrary, it produces a more significant phase space modulation (with some amount of line density modulation, see Fig. 4.8) when the cavity eigenfrequency is nearer to the resonance with the beam.

In the latter case, as a result, the instabilities become evident prior to and faster than without the RF voltage applied. The shapes of the rising beam density modulation (sinusoidal in the beginning and with a sharp slope backwards in the beam frame later on, Fig. 4.9) in all cases perfectly match the measured bunch signals (one can confront Fig. 4.9 with Fig. 3.6, where snapshots have been taken at the same times in the beam evolution). In the simulations we also have obtained maximum self-bunching peak currents of $\approx 400 - 530\,\mu$A, that are in good agreement with the $360 - 550\,\mu$A observed in the measurements.

Fig. 4.10 shows the instability rise times derived from the ESR measurements, along with the ones evaluated from the PATRIC simulations and the curve resulting from the analytical theory. The estimations from PATRIC confirm a reduction in the rise times caused by the external signal nearby the central part of the detuning curve.

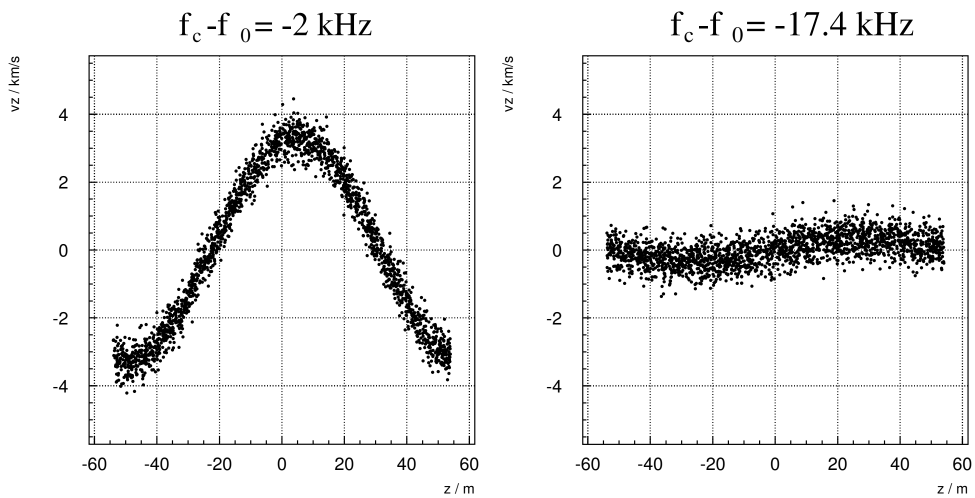

Figure 4.8: Beam modulation in the longitudinal phase space for small detuning, $\Delta f = -2$ kHz (left), and for large detuning, $\Delta f = -17.4$ kHz (right).

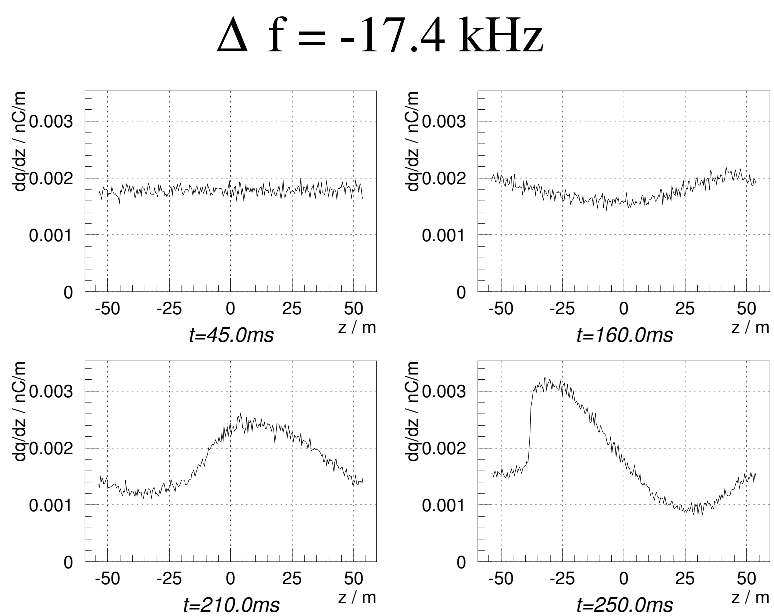

Figure 4.9: Evolution of the beam line density during an instability: growth of the slow wave and its saturation and steepening.

4.4 Theoretical modeling of the residual voltage

The first goal of the model presented in this section is to show how the phase space plots shown in Fig. 4.8 can be theoretically explained by means of a kinetic approach. For this very purpose, self-fields can be neglected, and the beam response to the action of the residual voltage alone is studied in detail. Only subsequently, a linear analysis of the evolution under the action of self-fields is carried out starting from the phase space modulated configuration, which was proven to be consistent with the presence of an external off-frequency voltage. With this procedure, it will become eventually clear when and how

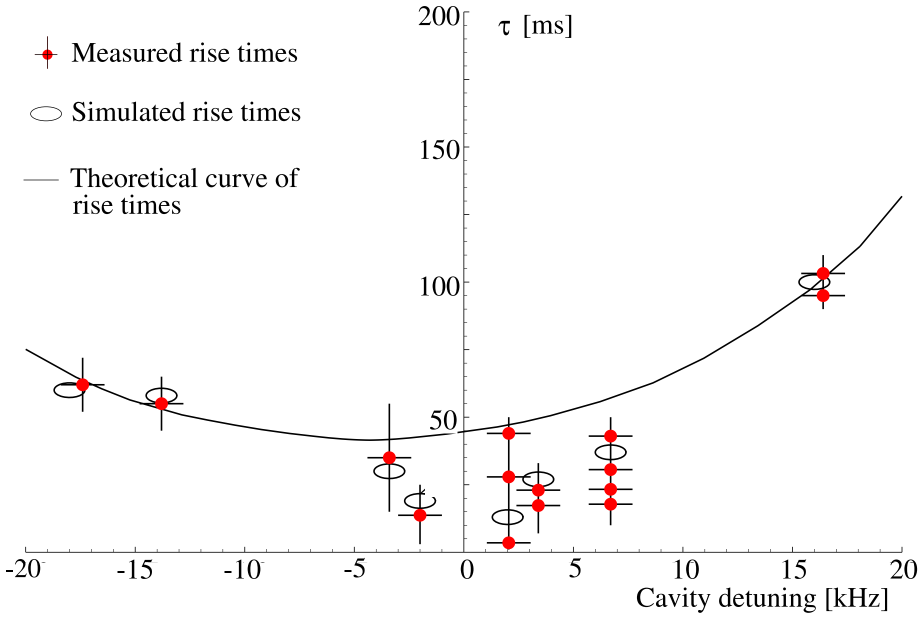

Figure 4.10: Rise times of the longitudinal instability: measured, theoretical, simulated.

much the residual voltage perturbs the results of the classical theory, and what changes are to be expected for different values of the frequency offset.

4.4.1 Solution without self-fields

The starting point is the Vlasov equation in the beam frame

$$\frac{\partial f}{\partial t} + u\frac{\partial f}{\partial x} + \frac{qE(x,t)}{m^*}\frac{\partial f}{\partial u} = 0 \quad , \tag{4.5}$$

where the electric field that represents the driving term is not the self-induced term like in Eqs. (2.50) and (2.51), but is an external voltage not stationary over the beam. Besides, the beam is assumed to be initially a coasting beam: its velocity distribution might be taken to be Gaussian, but this not a necessary condition for the development we are presenting here:

$$\left\{ \begin{array}{l} E(x,t) = \dfrac{V_0}{2\pi r_0} \cos\left(\dfrac{x}{r_0} - \Delta\omega\, t\right) \\[2ex] f(x,u,t=0) = \tilde{f}(u) \qquad \text{e.g.,} \quad \tilde{f}(u) = \dfrac{1}{\sqrt{2\pi}\sigma_u} \exp\left(\dfrac{u^2}{2\sigma_u^2}\right) \end{array} \right. . \tag{4.6}$$

As the simulations suggest (looking at the snake-shaped phase space distribution that appears to be the solution of this problem), a good attempt for proceeding consists in defining first:

$$\left\{ \begin{array}{l} \xi = \dfrac{x}{r_0} - \Delta\omega\, t \\[2ex] U = u - \Delta v(t) \cos[\xi(x,t) + \theta(t)] \end{array} \right. , \tag{4.7}$$

and seeking then a solution in the form:

$$f(x,u,t) = \tilde{f}(U) \quad , \tag{4.8}$$

which certainly satisfies the initial condition $f(x,u,t=0)=\tilde{f}(u)$ if $\Delta v(0)=0$, whatever is $\theta(0)$. Substituting the ansatz (4.8) in the Vlasov equation (4.5), we obtain:

$$\Delta v(t)\left(\frac{\mathrm{d}\theta}{\mathrm{d}t}-\Delta\omega\right)\sin(\xi+\theta)-\frac{\mathrm{d}\Delta v}{\mathrm{d}t}\cos(\xi+\theta)+u\frac{\Delta v(t)}{r_0}\sin(\xi+\theta)+\frac{qV_0}{m^*2\pi r_0}\cos\xi=0\,.$$

At this point, we expand the terms in sine and cosine, and we separately equal their coefficients to zero. This procedure yields:

$$\begin{cases}\Delta v(t)\left(\frac{\mathrm{d}\theta}{\mathrm{d}t}-\Delta\omega\right)\cos\theta(t)+\frac{\mathrm{d}\Delta v}{\mathrm{d}t}\sin\theta(t)+\frac{u\Delta v(t)}{r_0}\cos\theta(t)=0\\ \Delta v(t)\left(\frac{\mathrm{d}\theta}{\mathrm{d}t}-\Delta\omega\right)\sin\theta(t)-\frac{\mathrm{d}\Delta v}{\mathrm{d}t}\cos\theta(t)+\frac{u\Delta v(t)}{r_0}\sin\theta(t)+\frac{qV_0}{m^*2\pi r_0}=0\end{cases}\,. \tag{4.9}$$

This couple of equations still depends on u, and thus it would not allow a closed solution of the problem for the dynamics of $\Delta v(t)$ and $\theta(t)$, unless we make use at this stage of the approximation $\Delta\omega\gg u/r_0$. In fact, this is absolutely legitimated, at least in our case, if we take into consideration the values relative to the measurements about which we have reported in this work: $|\Delta\omega|/(2\pi)\sim 2000-30000$ Hz and $|u|/(2\pi r_0)\sim 0-28$ Hz. Using this approximation, Eqs. (4.9) become:

$$\begin{cases}-\Delta v(t)\left(\Delta\omega-\frac{\mathrm{d}\theta}{\mathrm{d}t}\right)\cos\theta(t)+\frac{\mathrm{d}\Delta v}{\mathrm{d}t}\sin\theta(t)=0\\ -\Delta v(t)\left(\Delta\omega-\frac{\mathrm{d}\theta}{\mathrm{d}t}\right)\sin\theta(t)-\frac{\mathrm{d}\Delta v}{\mathrm{d}t}\cos\theta(t)+\frac{qV_0}{m^*2\pi r_0}=0\end{cases}\,. \tag{4.10}$$

The set of equations (4.10) can be numerically solved. But before that, it might be interesting to find out from these equations that an eventual regime situation is reached, in which the phase space distribution along the ring oscillates sinusoidally at a fixed velocity amplitude and with constant phase velocity $r_0\cdot\Delta\omega$ (this is what we actually do expect after the results of the PATRIC simulations with the off-frequency voltage). Such a situation would require that the following conditions are satisfied:

$$\lim_{t\to+\infty}\Delta v(t)=\Delta v_{\mathrm{fin}}\quad \lim_{t\to+\infty}\theta(t)=\theta_{\mathrm{fin}}\quad\Longrightarrow\quad\lim_{t\to+\infty}\frac{\mathrm{d}\Delta v}{\mathrm{d}t}=0\quad\lim_{t\to+\infty}\frac{\mathrm{d}\theta}{\mathrm{d}t}=0\,. \tag{4.11}$$

From the former of the (4.10), one would expect:

$$\Delta v_{\mathrm{fin}}=0\quad\text{or}\quad\cos\theta_{\mathrm{fin}}=0\Rightarrow\theta_{\mathrm{fin}}=\pm\pi/2\,,$$

whereas it is straightforward from the latter to realize that it cannot be $\Delta v_{\mathrm{fin}}=0$ and consequently, since it has to be $\theta_{\mathrm{fin}}=\pm\pi/2$:

$$\mp\Delta v_{\mathrm{fin}}\Delta\omega+\frac{qV_0}{m^*2\pi r_0}=0\ \Rightarrow\ \Delta v_{\mathrm{fin}}=\pm\frac{qV_0}{m^*2\pi r_0}\cdot\frac{1}{\Delta\omega} \tag{4.12}$$

This expression for the final Δv can be put in a different form,

$$|\Delta v_{\mathrm{fin}}|=\frac{|\eta|qV_0}{2\pi p_0}\left(\frac{\omega_0}{\Delta\omega}\right)\,,$$

which is the formula that can be read in Ref. [29], too.
At any rate, this regime analysis – which, we would like to point out here, does not mean that the system comes to an equilibrium time-independent situation – allows us to draw

the conclusion that under the action of an external off-frequency voltage alone[2] the beam will eventually reach this configuration ($\theta_{\rm fin} = \pi/2$):

$$f_\infty(x,u,t) = \tilde{f}\left[u - \frac{qV_0}{m^* 2\pi r_0 \Delta\omega}\cos\left(\frac{x}{r_0} - \Delta\omega\, t + \frac{\pi}{2}\right)\right] =$$

$$= \tilde{f}\left[u + \frac{qV_0}{m^* 2\pi r_0 \Delta\omega}\sin\left(\frac{x}{r_0} - \Delta\omega\, t\right)\right] \tag{4.13}$$

If the choice $\theta_{\rm fin} = -\pi/2$ had been made, there would have consistently resulted $\Delta v_{\rm fin} = -qV_0/(m^* 2\pi r_0 \Delta\omega)$, and hence the expression (4.13) would stay unchanged. Besides, there is another important observation to make about the initial condition for $\theta(t)$. As it must be $\Delta v(0) = 0$, from the former equation of the (4.10) one would obtain either $\mathrm{d}\Delta v/\mathrm{d}t(0) = 0$ or $\sin\theta(0) = 0$. But $\mathrm{d}\Delta v/\mathrm{d}t(0) = 0$ is inconsistent with the latter equation (as long as there is a non-zero voltage oscillating at the cavity gap), and so it must be:

$$\sin\theta(0) = 0 \quad \Rightarrow \quad \theta(0) = 0$$

Of course, one can easily check that the choice $\theta(0) = \pi$ would have not changed the subsequent development predicted by the Eqs. (4.10), consistently with the uniqueness of the solution of the problem.

The set of differential equations (4.10) has been numerically solved with the 4th order Runge-Kutta algorithm, and for this purpose it needed to be recast in explicit form:

$$\begin{cases} \dfrac{\mathrm{d}\Delta v}{\mathrm{d}t} = \dfrac{qV_0}{m^* 2\pi r_0}\cos\theta(t) \\ \dfrac{\mathrm{d}\theta}{\mathrm{d}t} = \Delta\omega - \dfrac{qV_0}{m^* 2\pi r_0}\dfrac{\sin\theta(t)}{\Delta v(t)} \end{cases} . \tag{4.14}$$

The initial conditions to be coupled with this system are, as we know

$$\Delta v(t=0) = 0 \qquad \theta(t=0) = 0\ ,$$

which determine the time derivatives in $t = 0$:

$$\begin{aligned} &\frac{\mathrm{d}\Delta v}{\mathrm{d}t}(t=0) = \frac{qV_0}{m^* 2\pi r_0} \\ &\frac{\mathrm{d}\theta}{\mathrm{d}t}(t=0) = \Delta\omega - \frac{qV_0}{m^* 2\pi r_0}\lim_{t\to 0^+}\frac{\sin\theta(t)}{\Delta v(t)} \end{aligned} . \tag{4.15}$$

The limit in the second of the (4.15) is to be calculated with the De L'Hôpital theorem,

$$\lim_{t\to 0^+}\frac{\sin\theta(t)}{\Delta v(t)} = \lim_{t\to 0^+}\frac{\cos\theta(t)\dfrac{\mathrm{d}\theta}{\mathrm{d}t}}{\dfrac{\mathrm{d}\Delta v}{\mathrm{d}t}} = \frac{\dfrac{\mathrm{d}\theta}{\mathrm{d}t}(t=0)}{\dfrac{qV_0}{m^* 2\pi r_0}}\ ,$$

so that, plugging this into the second of Eqs. (4.15):

$$\frac{\mathrm{d}\theta}{\mathrm{d}t}(t=0) = \Delta\omega - \frac{\mathrm{d}\theta}{\mathrm{d}t}(t=0) \Rightarrow \frac{\mathrm{d}\theta}{\mathrm{d}t}(t=0) = \frac{\Delta\omega}{2}\ ,$$

[2] Of course, provided that the frequency offset is large enough with respect to the beam revolution frequency spread, approximation $\Delta\omega \gg u/r_0$

and we finally get the correct value for the time derivative of $\theta(t)$ in $t = 0$, which is essential for the numerical computation. Fig. 4.11 shows the time evolution of $\Delta v(t)$ (a) and of $\theta(t)$ (b), and we can see that, as expected, after a transient of some tens of milliseconds, in which both functions exhibit very high amplitude oscillations (they are anyways tolerable because they damp and cannot lead to beam losses meanwhile), they both end up coming to their asymptotic values that exactly correspond to those evaluated with the regime analysis performed above.

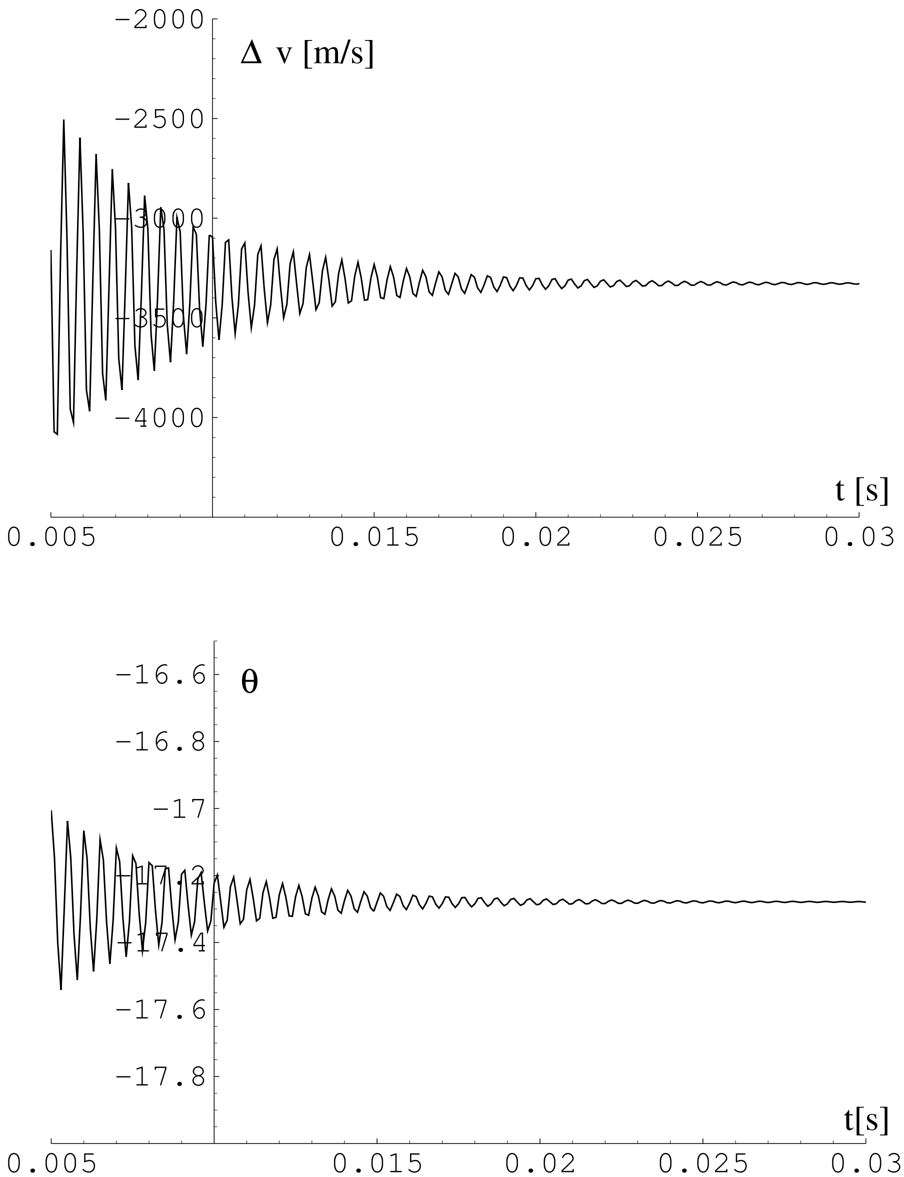

Figure 4.11: $\Delta v(t)$ (above) and $\theta(t)$ (below), when the sinusoidal off-frequency voltage, $V_{\text{ext}} = 350$ V with a $\Delta f = -2$ kHz, is abruptly applied on a uniform coasting beam from $t = 0$. After a transient with large amplitude oscillations, their values eventually come to the expected regime values.

The strong oscillations present in the first part of the phase space evolution are essentially due to the fact that we have assumed to start from a uniform coasting beam in $t = 0$, and we have abruptly applied the external voltage in that very same instant. On the other hand, it would be more reasonable to choose as driving term in the Eqs. (4.10) a voltage that rises linearly from zero to its final value, and the uniform coasting beam distribution given at $t = 0$ would then be consistent with the zero voltage at the same time instant. Such a voltage ramp has been performed in the PATRIC simulations with the external voltage, too, in order to avoid the transient with high amplitude phase space oscillations. Under this assumption, Eqs. (4.10) become

$$\begin{cases} \dfrac{\mathrm{d}\Delta v}{\mathrm{d}t} = \dfrac{qV(t)}{m^* 2\pi r_0} \cos\theta(t) \\ \dfrac{\mathrm{d}\theta}{\mathrm{d}t} = \Delta\omega - \dfrac{qV(t)}{m^* 2\pi r_0} \dfrac{\sin\theta(t)}{\Delta v(t)} \end{cases} \tag{4.16}$$

$$\text{with} \quad V(t) = \frac{V_0}{T} t \cdot [1(t) - 1(t-T)] + V_0 \cdot 1(t-T) \ ,$$

where T is the time interval on which the voltage is ramped, assumed to be of the same order of magnitude as the transient time – some 15-20 ms – in both our numerical analyses (PATRIC simulations and integration of Eqs. (4.16)). The numerical solution of these equations (Fig. 4.12) shows indeed that the maximum amplitude Δv_{fin} is reached smoothly, with no strong oscillations, as well as the phase θ soon damps down to its final value. In Fig. 4.13, one can see the space-time profile of $\Delta v(x,t)$ from $t = 0$ to the completion of the voltage ramp, and a little further. The growing sinusoidal shape exactly matches that observed in the PATRIC simulated phase space distributions all along the voltage ramp.

4.4.2 Linear analysis with self-fields

Now we have our starting point for a perturbative study of the Vlasov equation with self-fields and an external signal oscillating in the cavity. We only have to assume that every development due to the action of the self-induced fields appears far later than the regime is reached due to the external signal. This is exactly the case in our measurements, because there the regime takes 10-15 ms to be reached, whereas the instability that rises from pure statistical noise takes at least 3-4 times that (for the working points where it grows faster). Under this assumption, for the beam distribution function

$$f(x,u,t) = \tilde{f}(u + \Delta v_{\mathrm{fin}} \sin(x/r_0 - \Delta\omega\, t)) + \delta f(x,u,t) = f_{\mathrm{reg}}(x,u,t) + \delta f(x,u,t) \ ,$$

the Vlasov equation will be:

$$\frac{\partial f_{\mathrm{reg}}}{\partial t} + \frac{\partial \delta f}{\partial t} + u\frac{\partial f_{\mathrm{reg}}}{\partial x} + u\frac{\partial \delta f}{\partial x} +$$
$$+ \left[\frac{qV_0}{2\pi r_0 m^*} \cos\left(\frac{x}{r_0} - \Delta\omega\, t\right) + \frac{q}{2\pi r_0 m^*} \sum_n \dot{Z}(n\omega_0) I_n(t)\right] \left(\frac{\partial f_{\mathrm{reg}}}{\partial u} + \frac{\partial \delta f}{\partial u}\right) = 0 \tag{4.17}$$

In this equation we may cancel the terms that represent the "dynamic equilibrium" of $f_{\mathrm{reg}}(x,u,t)$, and also introduce the usual assumption for small-amplitude analysis $|\partial\delta f/\partial u| \ll |\partial f_{\mathrm{reg}}/\partial u|$:

$$\frac{\partial \delta f}{\partial t} + u\frac{\partial \delta f}{\partial x} + \frac{qV_0}{2\pi r_0 m^*} \cos\left(\frac{x}{r_0} - \Delta\omega\, t\right) \frac{\partial \delta f}{\partial u} + \frac{q}{2\pi r_0 m^*} \sum_n \dot{Z}(n\omega_0) I_n(t) \cdot \frac{\partial f_{\mathrm{reg}}}{\partial u} = 0 \ . \tag{4.18}$$

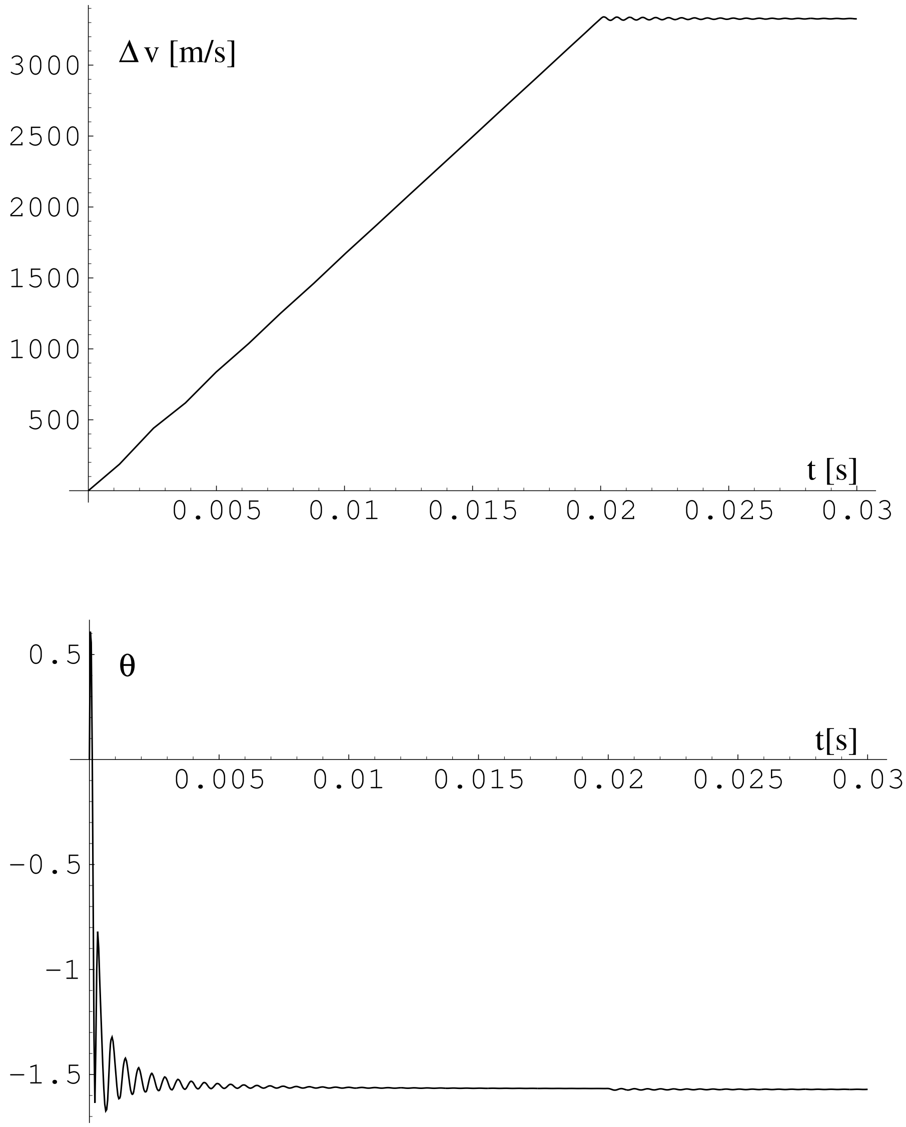

Figure 4.12: $\Delta v(t)$ (above) and $\theta(t)$ (below), when the sinusoidal off-frequency voltage, $V_{\rm ext} = 350$ V with a $\Delta f = -2$ kHz, is ramped from zero to its final value within 20 ms (on a uniform coasting beam in $t = 0$). Contrary to what happened in the case where the voltage was abruptly applied, the value of Δv smoothly follows the driving voltage ramp and eventually comes to its expected regime value, whereas the phase $\theta(t)$ goes through a much shorter oscillatory transient and quickly comes to its regime value.

Furthermore, we use the following expansions in Fourier series (possible thanks to the periodicity of the functions):

$$f_{\rm reg}(x,u,t) = \tilde{f}(u + \Delta v_{\rm fin} \sin\xi) = \sum_m \varphi_m(u) \exp(-{\rm i}m\xi) \ ,$$

$$\frac{\partial f_{\rm reg}}{\partial u} = \sum_m \frac{\partial \varphi_m}{\partial u} \exp\left[-{\rm i}m\left(\frac{x}{r_0} - \Delta\omega\, t\right)\right] \ ,$$

$$\delta f(x,u,t) = \sum_n \delta f_n(u,t) \exp\left(-{\rm i}n\frac{x}{r_0}\right) \ .$$

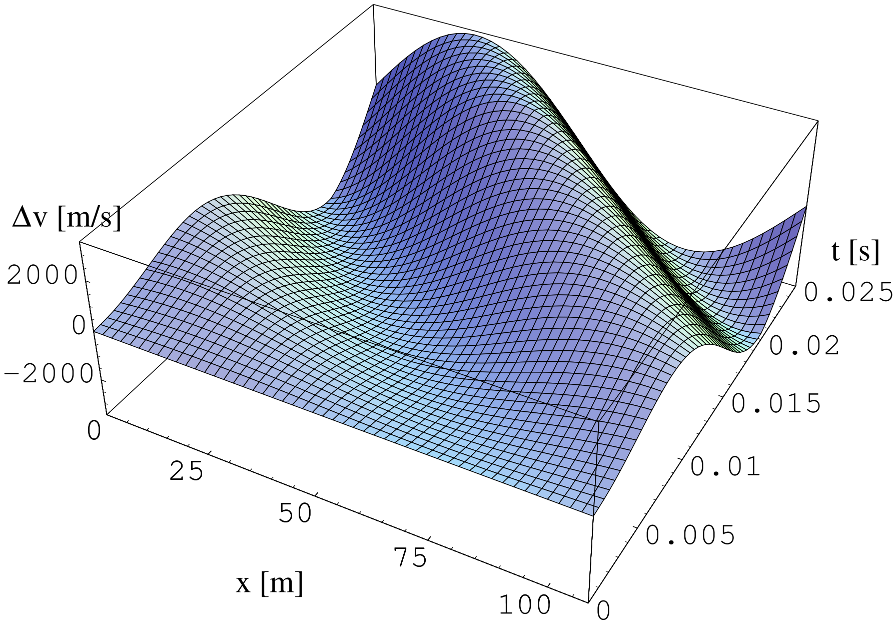

Figure 4.13: $\Delta v(x,t)$ for an external voltage ramped over 20 ms (same case as in Fig. 4.12). It is clear from this picture that the phase space modulation regularly grows during the ramping time and eventually leads to the snake-shaped distribution which was first observed in the PATRIC simulations.

Thus, Eq. (4.18) assumes the complicated form:

$$\sum_n \frac{\partial \delta f_n}{\partial t} \exp\left(-\mathrm{i}n\frac{x}{r_0}\right) + \sum_n u\left(-\mathrm{i}\frac{n}{r_0}\right)\delta f_n \exp\left(-\mathrm{i}n\frac{x}{r_0}\right) +$$

$$+\frac{qV_0}{4\pi r_0 m^*}\left[\exp\left[\mathrm{i}\left(\frac{x}{r_0}-\Delta\omega\, t\right)\right]+\exp\left[-\mathrm{i}\left(\frac{x}{r_0}-\Delta\omega\, t\right)\right]\right]\sum_n \frac{\partial \delta f_n}{\partial u}\exp\left(-\mathrm{i}n\frac{x}{r_0}\right)+$$

$$+\frac{q}{4\pi r_0 m^*}\sum_n \dot{Z}(n\omega_0)\int \delta f_n \,\mathrm{d}u \exp\left(-\mathrm{i}n\frac{x}{r_0}\right)\cdot\sum_m \frac{\partial \varphi_m}{\partial u}\exp\left[-\mathrm{i}m\left(\frac{x}{r_0}-\Delta\omega\, t\right)\right]=0\,,$$

and we are interested in the evolution of the first harmonic ($n = 1$) of the perturbation, because the impedance has a real part sensibly different from zero only on the first harmonic in our case. Consequently, we separately equal to zero the term $n = 1$ from the equation above:

$$\frac{\partial \delta f_1}{\partial t} - \mathrm{i}\frac{u}{r_0}\delta f_1 + \frac{qV_0}{4\pi r_0 m^*}\frac{\partial \delta f_2}{\partial u}\exp(-\mathrm{i}\Delta\omega\, t)+$$

$$+\frac{q}{2\pi r_0 m^*}\left[\dot{Z}(\omega_0)\int \delta f_1 \,\mathrm{d}u\frac{\partial \varphi_0}{\partial u}+\sum_{\substack{n+m=1\\ n\neq 1}}\dot{Z}(n\omega_0)\int \delta f_n\,\mathrm{d}u\frac{\partial \varphi_m}{\partial u}\exp(\mathrm{i}m\Delta\omega\, t)\right]=0\,. \tag{4.19}$$

At this point, we need to make one last assumption: the dynamics of the perturbation $\delta f_1(u,t)$ evolves on a time scale much bigger than $\tau = 1/\Delta\omega$ - this condition is certainly met in the ESR experiment, where τ is always in the order of few tenths of a millisecond, whereas the perturbation has a characteristic time constant τ_{pert} of some tens of milliseconds. In this approximation, we can imagine to average Eq. (4.19) on a time which is long compared to τ, but short with respect to τ_{pert}. This yields a new equation for the slow dynamics of the first harmonic perturbation:

$$\frac{\partial \delta f_1}{\partial t} - \mathrm{i}\frac{u}{r_0}\delta f_1 + \frac{q}{2\pi r_0 m^*}\dot{Z}(\omega_0)\int \delta f_1 \,\mathrm{d}u \frac{\partial \varphi_0}{\partial u} = 0\ . \tag{4.20}$$

From this equation, we easily get to the same dispersion relation that we would obtain in the ordinary case for the complex frequency of the first harmonic perturbation, with the only difference that, instead of having the uniform coasting beam velocity distribution $\tilde{f}(u)$, we have the new function $\varphi(u)$, which actually represents the beam's initial velocity distribution:

$$\varphi(u) = \frac{1}{2\pi}\int_0^{2\pi} \tilde{f}(u + \Delta v_{\text{fin}} \sin\xi)\,\mathrm{d}\xi = \frac{1}{2\pi r_0}\int_0^{2\pi r_0} \tilde{f}\left[u + \Delta v_{\text{fin}} \sin\left(\frac{x}{r_0} - \Delta\omega\ t\right)\right]\,\mathrm{d}x\ . \tag{4.21}$$

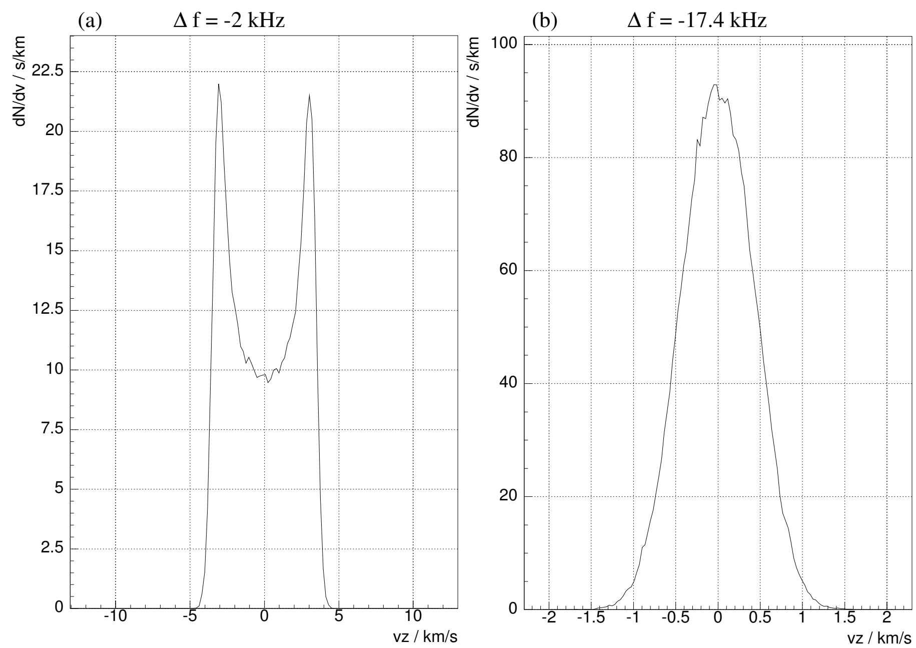

Figure 4.14: Velocity distribution functions averaged all along the beam. On the left is the double peaked distribution relative to a cavity detuning $\Delta f = -2$ kHz (a), and on the right is the almost unchanged distribution for $\Delta f = -17.4$ kHz (b).

This means that what mostly determines the stability of the beam still remains the phase space distribution averaged in the longitudinal coordinate along the ring. This consideration is well enough to explain why, for small frequency detuning, there is a reduction of the rise time of the expected instabilities: the distortion induced on the velocity distribution function for small detuning ($|\Delta\omega|$ below few kHz) is very strong and causes the formation of a dip in the center (see Fig. 4.14a), whilst for stronger detuning ($|\Delta\omega|$ above 10 kHz) there is no big change in this distribution (Fig. 4.14b). This altered feature of the distribution function produces a loss of Landau damping, as we know from Sec. 3.3.2, and consequently the instability appears and grows much quicker than in the case where the structure of the beam is uniform and coasting. Actually, the loss of Landau damping is also quite clear from the kinetic point of view: if the phase space distribution of the beam is modulated like in Fig. 4.8a, a slow wave having phase velocity in the range of the

beam's local velocity spread cannot feel the benefits of the Landau damping mechanism, since it always interacts with a much smaller number of particles[3]. In other words, there is no chance of slowing down the instability thanks to some amount of Landau damping, because the kinetic structure of the beam does not permit it.
These considerations satisfactorily support the drop in the rise times observed in the experiments with respect to the classical linear theory for the cases when the cavity was eventually tuned very close to the beam revolution frequency.

[3]Besides, this slow unstable wave also interacts with particles having the "wrong" slope in a fraction of the ring, and this might even cause an enhancement of the instability if the balance of energy exchange along the ring is globally favorable to the wave

Chapter 5

Early nonlinear evolution

As we have discussed in Chapter 4, from the measurements that we have carried out at the ESR, one can clearly observe both phenomena typical of the linear beam evolution, which are fully explained within the perturbative small-amplitude kinetic model (e.g., the exponential growth of the slow wave), and strongly nonlinear phenomena like generation of higher harmonics, asymmetric wave steepening, and wave growth saturation. In the current chapter, a one-dimensional fluid model is successfully developed and employed in order to give a satisfactory explanation of the growth of the slow wave as well as of the nonlinear steepening and higher harmonics generation. Taking into account the effects of the initial momentum spread of the beam through a modified space charge impedance, the model predicts with high accuracy the rise time and the frequency shift of the unstable wave (which would otherwise be more or less strongly underestimated in a purely cold-fluid model, according to the formulas in Section 3.3.2). Subsequently, nonlinear convective effects are shown to give rise to wave steepening and harmonic generation. Predictions of the fluid model are compared to experimental data and with those obtained under a full kinetic model as well as from the particle-in-cell code PATRIC [48].

5.1 Fluid model

Recently, a fluid model has been proposed to describe transverse equilibrium and stability properties of an unbunched, continuously-focused intense ion beam [54]. Furthermore, for space charge dominated beams, the mechanism of the longitudinal instability in coasting beams is intrinsically of fluid nature (see, for example, Ref. [31]). Therefore, our attempt has been to look into collective nonlinear fluid effects, such as convection, in order to give a physical explanation of the observed nonlinear phenomena in a longitudinally unstable beam.

Making use of the fluid model, it is possible to describe the initial phase of the instability growth when the operating point of the machine is far outside the stability region corresponding to the equilibrium velocity distribution of the beam. This limit of validity is due to the fact that in the fluid model Landau damping is completely absent [5, 6, 31]. The mechanism of beam stabilization due to Landau damping gives rise to a finite stability region in the impedance plane that cannot be predicted by a model where the wave-particle interaction is not taken into account. In other words, we must never expect that a fluid model can predict the existence of a stable beam when the resistive part of the impedance is different from zero, as occurs in kinetic theory. Even far outside the stability boundary the cold fluid model underestimates the rise time and the absolute value of the frequency shift that characterizes the unstable wave.

In this chapter, we will show that far outside the stability boundary the effect of the beam initial momentum spread plays the same role as the beam space charge impedance. In particular, we show that this effect cannot be neglected when the threshold impedance of the Keil-Schnell criterion (see, for instance, Ref. [31]) is of the same order of magnitude as the total impedance. This result suggests the use of a cold fluid model with a modified space charge impedance to take into account the effects of the initial momentum spread of the beam. This model foresees with high accuracy the instability rise time, frequency shift, wave steepening and higher harmonic generation.
The model is applied to the ESR storage ring, so that comparisons between the results obtained from the different models (fluid, kinetic, and particle-in-cell simulations with the PATRIC code [48]) and the data observed at the ESR may be drawn. These comparisons make clear how far the proposed macroscopic model provides a correct description of the beam dynamics and what nonlinear effects it can thoroughly explain.

In a fluid description, we shall examine the evolution of the macroscopic fluid properties of the beam such as the number line density (see the Vlasov equation in Sec. 3.2.1)

$$n(s,t) = \int_{-\infty}^{\infty} f(s,v,t)\,\mathrm{d}v\ , \tag{5.1}$$

the mean longitudinal velocity

$$U(s,t) = \frac{\displaystyle\int_{-\infty}^{\infty} v f(s,v,t)\,\mathrm{d}v}{n(s,t)}\ , \tag{5.2}$$

and the kinetic pressure

$$P(s,t) = \int_{-\infty}^{\infty} m^*(v-U)^2 f(s,v,t)\,\mathrm{d}v\ . \tag{5.3}$$

The beam current $I(s,t)$ is given by

$$I(s,t) = qn(s,t)U(s,t) \cong qv_0 n(s,t)\ . \tag{5.4}$$

In Eq. (5.4) we have approximated the actual averaged velocity of the beam with the nominal mean velocity v_0 because in real beams $|U - v_0|$ is very small compared with $|v_0|$, whereas $|n - n_0|$ can become the same order of magnitude as n_0. Operating on the Vlasov equation (2.10) with the moments technique, yields the continuity equation

$$\frac{\partial n}{\partial t} + \frac{\partial}{\partial s}(nU) = 0\ , \tag{5.5}$$

the momentum equation

$$\frac{\partial}{\partial t}(m^* nU) + \frac{\partial}{\partial s}\left[(m^* nU)U + P\right] = \frac{1}{2\pi r_0} qn\phi\ , \tag{5.6}$$

and the pressure equation

$$\frac{\partial}{\partial t}\left(\frac{P}{n^3}\right) + U\frac{\partial}{\partial s}\left(\frac{P}{n^3}\right) + \frac{1}{n^3}\frac{\partial Q}{\partial s} = 0\ , \tag{5.7}$$

where $Q(s,t)$, defined as

$$Q(s,t) = \int_{-\infty}^{\infty} m^*(v-U)^3 f(s,v,t)\,\mathrm{d}v\ , \tag{5.8}$$

represents the longitudinal heat flow inside the beam. Now we assume that during the beam evolution the heat flow is negligible within the beam, that is $Q(s,t) = 0$. In this way we get a closure for the model (adiabatic assumption).
Similar to what we have already done in Sec. 3.3 directly on the Vlasov equation, it is useful here to recast the fluid equations (5.5) -(5.7) in such a way as to hide the "fast" component of the dynamics - namely the one associated to the beam orbiting in the ring, its characteristic time being $2\pi/\omega_0$ - and provide a description for the evolution of the "slow" component alone. For this purpose, we perform the following linear transformation of variables:

$$\begin{cases} U = v_0 + V \\ s = v_0 t + x \end{cases} . \tag{5.9}$$

By applying this transformation to the equations (5.5)- (5.7) we obtain

$$\begin{cases} \dfrac{\partial \Lambda}{\partial t} + \dfrac{\partial}{\partial x}(\Lambda V) = 0 \\ \dfrac{\partial V}{\partial t} + V\dfrac{\partial V}{\partial x} + \dfrac{q}{\Lambda}\dfrac{\partial}{\partial x}(R\Lambda^3) = -\dfrac{q}{2\pi r_0 m^*}\psi(x,t) \\ \dfrac{\partial R}{\partial t} + V\dfrac{\partial R}{\partial x} = 0 \end{cases} \tag{5.10}$$

where $\Lambda(x,t) = qn(x+v_0t,t)$, $V(x,t) = U(x+v_0t,t) - v_0$, $R(x,t) = P(x+v_0t,t)/\Lambda^3(x,t)$, the potential function $\psi(x,t)$ is given by

$$\psi(x,t) = \frac{v_0 X_{\mathrm{sc}}}{k_0}\frac{\partial \Lambda}{\partial x} + v_0 \sum_m \dot{Z}_{\mathrm{cav}}(m\omega_0)\Lambda_m(t)\exp(-\mathrm{i}mk_0x) , \tag{5.11}$$

and

$$\Lambda_m(t) = \frac{1}{C_0}\int_0^{C_0} \Lambda(x,t)\exp(\mathrm{i}mk_0x)\,\mathrm{d}x ; \tag{5.12}$$

the quantity $\Lambda(x,t)$ represents the line charge density. The first term on the right hand side of (5.11) is the potential due to the interaction of the beam with the pipe, assumed to be perfectly conducting.
Due to the periodicity of the structure, the system (5.10) is to be solved with periodic boundary conditions, $\Lambda(x=0,t) = \Lambda(x=C_0,t)$, $V(x=0,t) = V(x=C_0,t)$ and $R(x=0,t) = R(x=C_0,t)$.

5.2 Linear analysis of the warm-fluid model

To study the stability of the beam, we consider the linearized version of the set of Eqs. (5.10)

$$\begin{cases} \dfrac{\partial \delta\Lambda}{\partial t} + \Lambda_0\dfrac{\partial \delta V}{\partial x} = 0 \\ \dfrac{\partial \delta V}{\partial t} + \dfrac{q}{\Lambda_0}\dfrac{\partial \delta P}{\partial x} = -\dfrac{q}{2\pi r_0 m^*}\psi(x,t) \\ \dfrac{\partial}{\partial t}\left(\dfrac{\delta P}{\Lambda_0^3} - \dfrac{3P_0}{\Lambda_0^3}\dfrac{\delta\Lambda}{\Lambda_0}\right) = 0 \end{cases} ; \tag{5.13}$$

Λ_0 and P_0 are respectively the equilibrium line charge density and pressure along the ring, whereas $\delta\Lambda$, δV and δP represent the perturbations. From the definition of P, it is straightforward to find out the relation between P_0 and the beam's initial velocity spread Δu_{HWHM}:

$$P_0 = \frac{m^* \Lambda_0}{2q \ln 2} \Delta u_{\mathrm{HWHM}}^2 \,. \tag{5.14}$$

Observing that the third of the (5.13) easily provides

$$\delta P = 3P_0 \frac{\delta\Lambda}{\Lambda_0} + \text{const.} \tag{5.15}$$

and using the expression (5.11) of the potential $\psi(x, t)$, we finally find the system of equations for $\delta\Lambda$ and δV,

$$\begin{cases} \dfrac{\partial \delta\Lambda}{\partial t} + \Lambda_0 \dfrac{\partial \delta V}{\partial x} = 0 \\ \dfrac{\partial \delta V}{\partial t} = -\dfrac{q}{m^*} \dfrac{U_0}{2\pi} \left(\dfrac{6\pi m^* P_0}{v_0 \Lambda_0^2} + X_{\mathrm{sc}} \right) \dfrac{\partial \Lambda}{\partial x} - \dfrac{q v_0}{2\pi r_0 m^*} \displaystyle\sum_m \dot{Z}_{\mathrm{cav}}(m\omega_0) \Lambda_m(t) \exp(-\mathrm{i} m k_0 s) \,. \end{cases} \tag{5.16}$$

From the second equation of system (5.16), it becomes clear that the influence of the pressure term acts in the linear phase of the beam evolution exactly as a further contribution to the space charge impedance seen by the beam. Thus, the effect of a finite pressure can be taken into account by considering a

$$X_{\mathrm{eq}} = X_{\mathrm{sc}} + X_{\mathrm{kin}} \,, \tag{5.17}$$

in a fluid model with $P = 0$ (cold fluid model), where

$$X_{\mathrm{kin}} = 6\pi \left(\frac{\mathrm{k} T_0}{q I_0} \right) \,; \tag{5.18}$$

$$T_0 = \frac{q P_0}{\Lambda_0 \mathrm{k}} \tag{5.19}$$

is the initial longitudinal temperature of the beam. A useful way of writing X_{kin} is

$$X_{\mathrm{kin}} \cong 3.1 |\dot{Z}_{\mathrm{th}}| \,, \tag{5.20}$$

where

$$|\dot{Z}_{\mathrm{th}}| = 0.7 \frac{2\pi p_0 \beta_0 c |\eta|}{q I_0} \left(\frac{\delta p}{p_0} \right)_{\mathrm{HWHM}}^2 \tag{5.21}$$

is simply the threshold impedance of the Keil-Schnell criterion [43]; as the initial velocity distribution of the beam has been assumed to be Gaussian, the form factor is around 1. Thus, the effect of the pressure cannot be neglected when the Keil-Schnell impedance is the same order of magnitude as the space charge impedance.

If we give the perturbations a space-time dependence of the kind

$$\begin{aligned} \delta\Lambda(x, t) &= A_m \exp[\mathrm{i}(\Delta\omega\, t - m k_0 x)] + \text{c.c.} \\ \delta V(x, t) &= B_m \exp[\mathrm{i}(\Delta\omega\, t - m k_0 x)] + \text{c.c.} \end{aligned} \tag{5.22}$$

and we substitute them into Eqs. (5.13), we obtain for the complex frequency $\Delta\omega = \Delta\omega_r + i\Delta\omega_i$

$$\begin{aligned} \Delta\omega_r &= \pm\omega_0 \left[\frac{1}{2\dot{Z}^*} \left(\sqrt{\mathrm{Re}(\dot{Z})^2 + \mathrm{Im}(\dot{Z})^2} - \mathrm{Im}(\dot{Z}) \right) \right]^{1/2} \\ \Delta\omega_i &= \pm\omega_0 \left[\frac{1}{2\dot{Z}^*} \left(\sqrt{\mathrm{Re}(\dot{Z})^2 + \mathrm{Im}(\dot{Z})^2} + \mathrm{Im}(\dot{Z}) \right) \right]^{1/2} \end{aligned} \,, \tag{5.23}$$

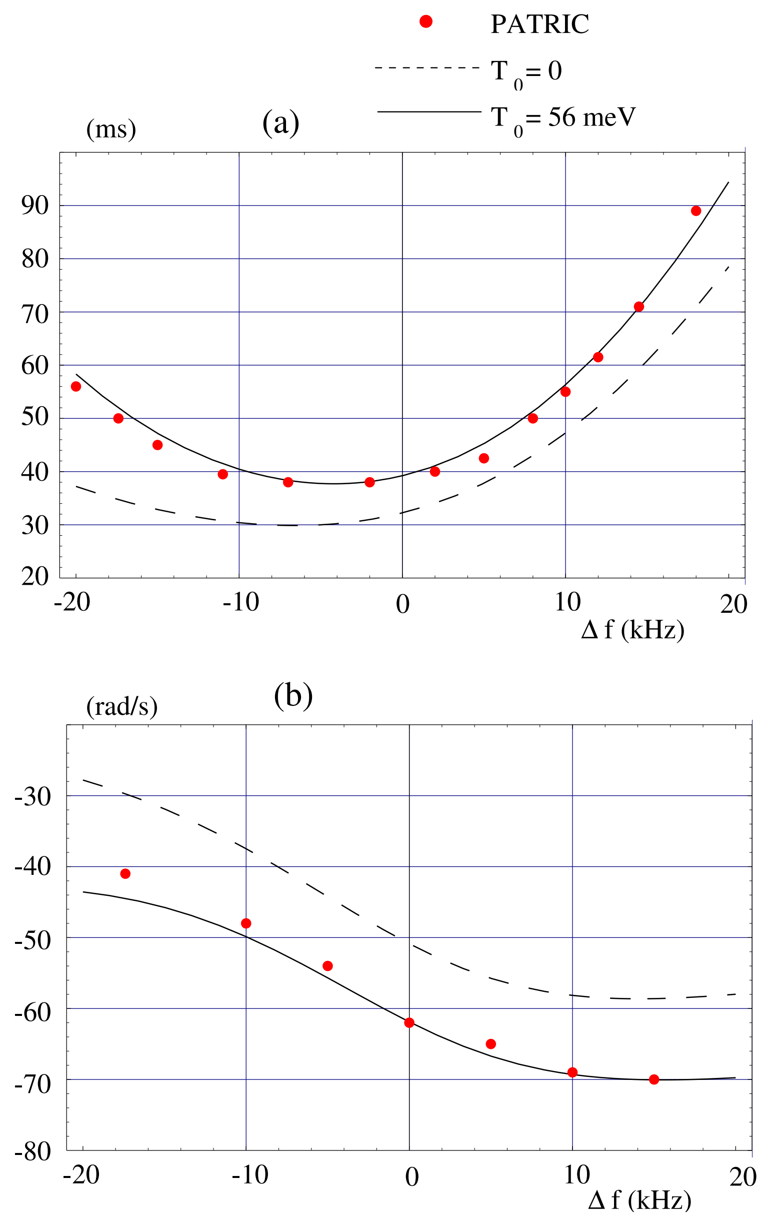

Figure 5.1: Comparison between the growth times (a) and the frequency shifts (b) obtained from the warm-fluid model with those obtained from the kinetic and the cold fluid model.

where

$$\mathrm{Re}(\dot{Z}) = \mathrm{Re}[\dot{Z}_{\mathrm{cav}}(m\omega_0)] \; , \;\; \mathrm{Im}(\dot{Z}) = \mathrm{Im}[\dot{Z}_{\mathrm{cav}}(m\omega_0)] - mX_{\mathrm{eq}} \; , \tag{5.24}$$

and the characteristic resistance $\dot{Z}^*$ is given by

$$\dot{Z}^* = 2\pi \frac{|m^*| v_0^2}{qI_0} \; . \tag{5.25}$$

Thus, the fluid model predicts a longitudinal exponential instability to appear whenever the impedance is not purely capacitive (below the transition energy). Beam stability in case of interaction with an impedance having a resistive part is never possible in this model, because we are neglecting the wave-particle interaction and, hence, the stabilizing mechanism of Landau damping. However, the results obtained from the fluid model are to some extent correct if the operating point on the stability diagram is far away from the stability boundary, as was in the recent ESR measurements [30]. In fact, relatively to our cavity detuning experiment, in Figs. 5.1a and 5.1b the growth times and the frequency shifts for $m = 1$ predicted by the linear kinetic theory in a region far outside the stability boundary are plotted along with those obtained from the fluid models with $T_0 = 0$ and $T_0 = 56$ meV. The improvement achieved by considering the effect of the initial finite temperature is impressive.

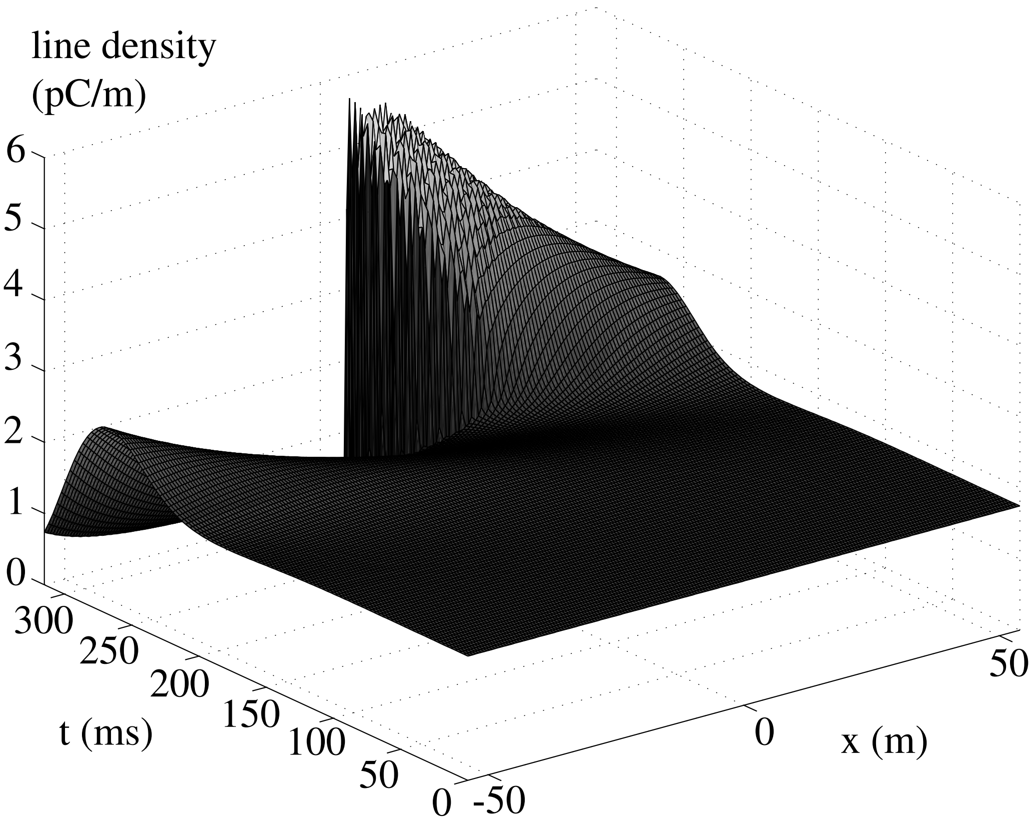

Figure 5.2: Space-time evolution of the line charge density $\Lambda(x,t)$ predicted by the cold fluid model with corrected space charge impedance for $\Delta f = -17.4$ kHz and $I_0 = 0.366$ mA.

5.3 Interpretation of the early nonlinear evolution at the ESR

Due to the above results, the analysis of the longitudinal evolution of the ESR beam can be performed by using a cold fluid model

$$\left\{ \begin{array}{l} \dfrac{\partial \Lambda}{\partial t} + \dfrac{\partial}{\partial x}(\Lambda V) = 0 \\ \dfrac{\partial V}{\partial t} + V \dfrac{\partial V}{\partial x} = -\dfrac{q}{2\pi r_0 m^*} \psi(x,t) \ . \end{array} \right. , \tag{5.26}$$

where we consider the corrected $X_{\rm eq}$ instead of the space charge reactance $X_{\rm sc}$. We use this model because we want to show that some nonlinear phenomena observed at the ESR

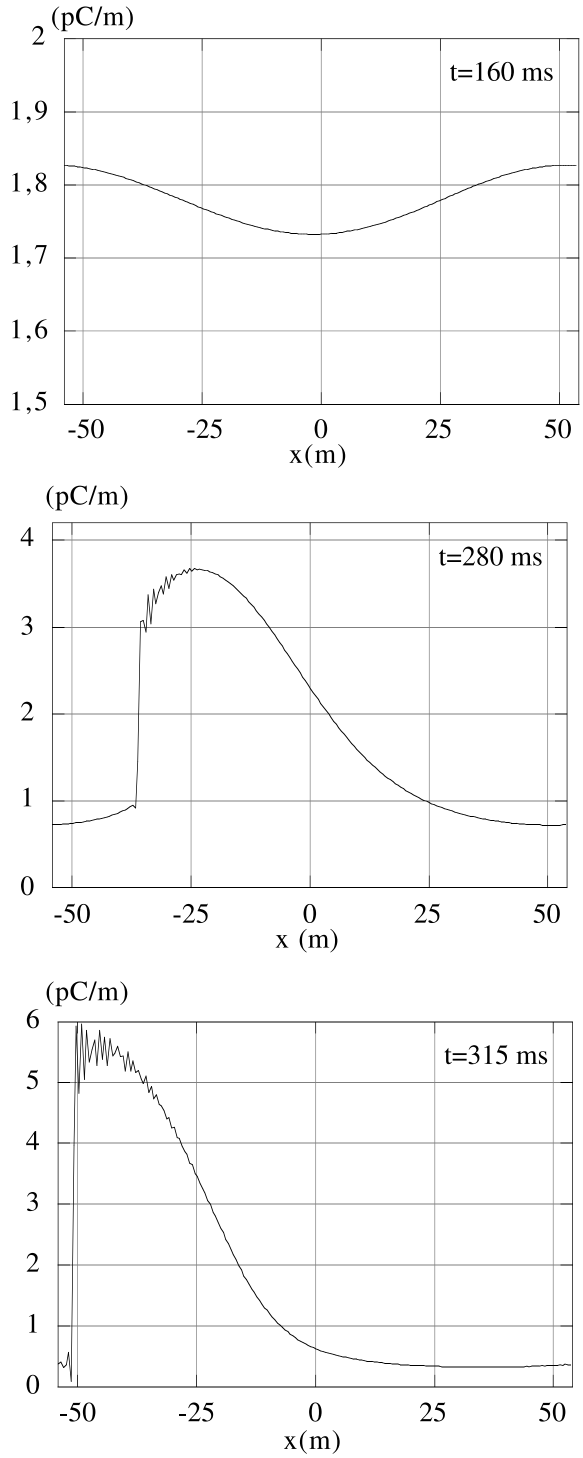

Figure 5.3: Distribution of the line charge density at different times obtained from the cold fluid model with corrected space charge impedance for $\Delta f = -17.4$ kHz and $I_0 = 0.366$ mA.

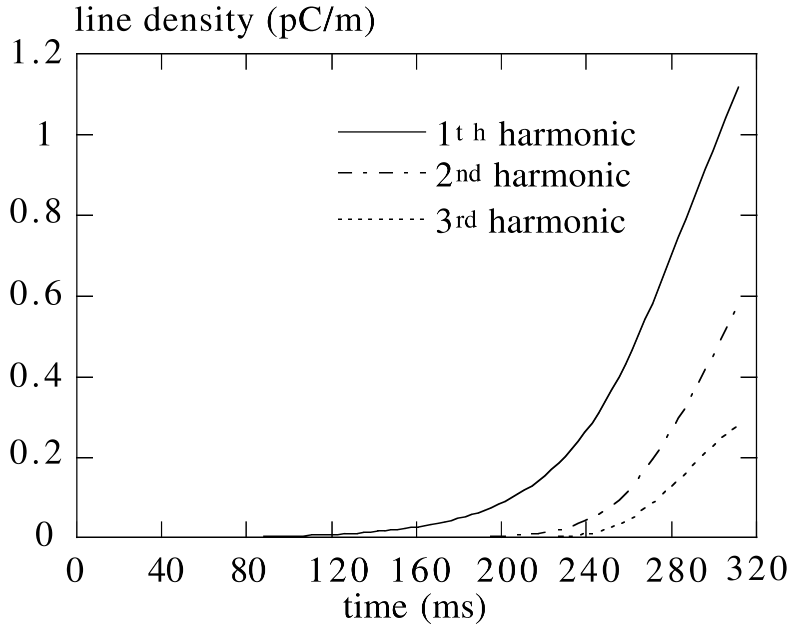

Figure 5.4: Time evolution of the first, second and third spatial harmonics of the line charge density obtained from the cold fluid model with corrected space charge impedance for $\Delta f = -17.4$ kHz and $I_0 = 0.366$ mA.

are only caused by the nonlinear convective terms $\partial(nV)/\partial x$ and $V\partial V/\partial x$.
The system (5.26) can be analytically solved only in the limit $|\Delta f| \rightarrow \infty$, where the longitudinal impedance of the machine is purely capacitive and the beam is stable. For the more interesting unstable case, numerical solutions of the system (5.26) are needed.
The numerical solution of Eqs. (5.26) is based on the finite difference approximation of the partial derivative operators. First of all, the equations are approximated in space using the method of the central differences (the error vanishes like Δx^2 for $\Delta x \rightarrow 0$, where Δx is the width of the spatial grid). The spatial interval $(0, C_0)$ has been uniformly parted into N intervals of width $\Delta x = C_0/N$. At the boundary grid points, the conditions of periodicity of the structure are imposed. In all the simulations, we have parted the ring circumference into up to 200 intervals. The Fourier integrals have been evaluated by using the FFT (Fast Fourier Transform) algorithm. The resulting system of ordinary differential equations in time has been then numerically integrated by a fourth order Runge-Kutta algorithm (the corresponding error vanishes as Δt^4 as $\Delta t \rightarrow 0$). The time step Δt has been chosen to assure the stability of the numerical algorithm and to correctly resolve the beam dynamics. The linear theory predicts in all cases under consideration frequency shifts ≤ 10 Hz. Therefore, in all simulations, we have chosen a time step of 1 ms, which allows a correct time resolution of the self-field and assures stability for the numerical algorithm.

In Fig. 5.2 the space-time evolution of the line charge density for $\Delta f = -17.4$ kHz and $I_0 = 0.366$ mA is shown. A slow wave growing in amplitude and getting steep to the left side in the late phase of the instability is clearly observable. In Figs. 5.3 the line charge densities at different phases of the beam evolution are represented: at 160 ms the

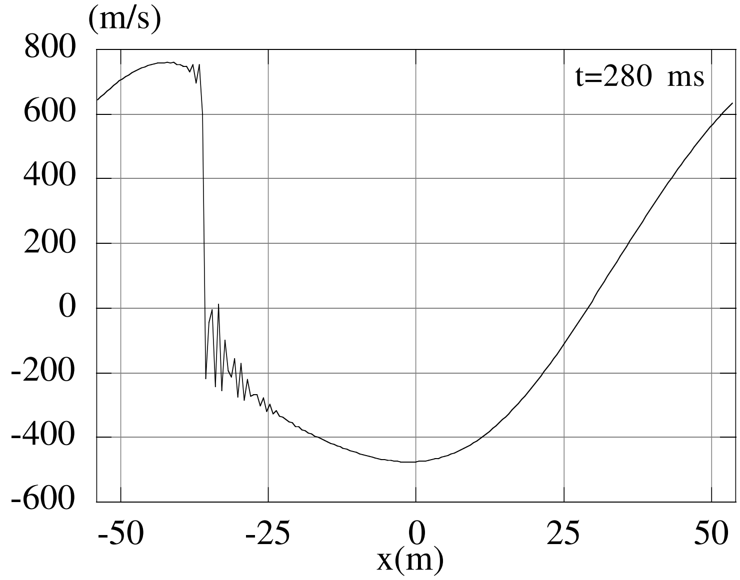

Figure 5.5: Distribution of the mean velocity obtained from the cold fluid model with corrected space charge impedance for $\Delta f = -17.4$ kHz and $I_0 = 0.366$ mA.

line density is still sinusoidal; at 280 ms the amplitude has grown so large that the wave shape becomes strongly asymmetric with a sharp left edge; at 315 ms a strongly depleted zone has formed. Higher order harmonics are produced late in the instability evolution, as soon as the first harmonic has become high enough to significantly drive their growth (Fig. 5.4); this is in agreement with what has been observed in the PATRIC simulations [29], even though no saturation of the growth appears now. In Fig. 5.5 the distribution of the fluid velocity is shown at 280 ms. In Fig. 5.6 the line density predicted by the fluid model, after the instability has gone through its linear phase, is compared with the one obtained from the particle-in-cell code PATRIC and with the experimental one from ESR, both taken at the same moment of the instability evolution. The bunch shapes predicted by the fluid model are in excellent accord both with simulations and measurements. The agreement during the phase of the steepening between the solution of the fluid equations, the measured data, and the relative PATRIC simulations, confirms that this phenomenon is simply a fluid mechanism that need not be explained by looking in further detail into the actual beam distribution in phase space. The steepening phenomenon is widely observed in gases, fluids [57] and plasmas [58].
Finally, Fig. 5.7 shows the time evolution of the beam current first harmonic: the saturation that clearly appears both in the experimental points and in the PATRIC simulation is on the other hand completely absent in the fluid evolution. The fluid model is not able to explain the saturation of the instability growth, because this phenomenon is due to resonant wave-particle interaction. As the instability grows, the electric potential associated with the fundamental mode becomes more and more intense, and most of the particles are trapped in the potential well: the conversion of untrapped particles into trapped particles leads to a situation in which the growth of the unstable mode stops.
Exponential growth of wave amplitudes, their saturation due to trapping of particles, and steepening of the wave profile due to the plasma nonlinearity, are also observed in beam-plasma interactions in solar wind [59].

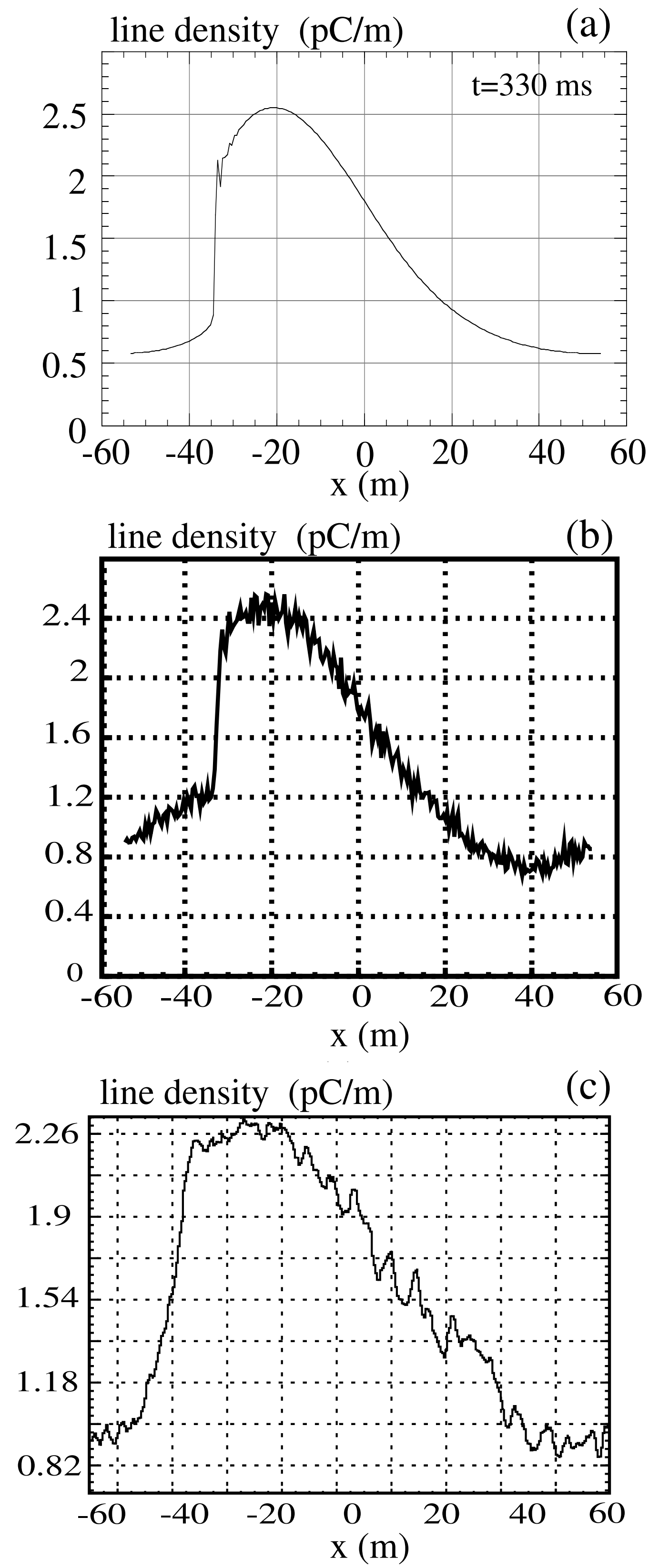

Figure 5.6: Distribution of the charge line density for $\Delta f = -17.4$ kHz and $I_0 = 0.276$ mA: cold fluid model with corrected space charge impedance (a); PATRIC code (b); ESR measurements (c).

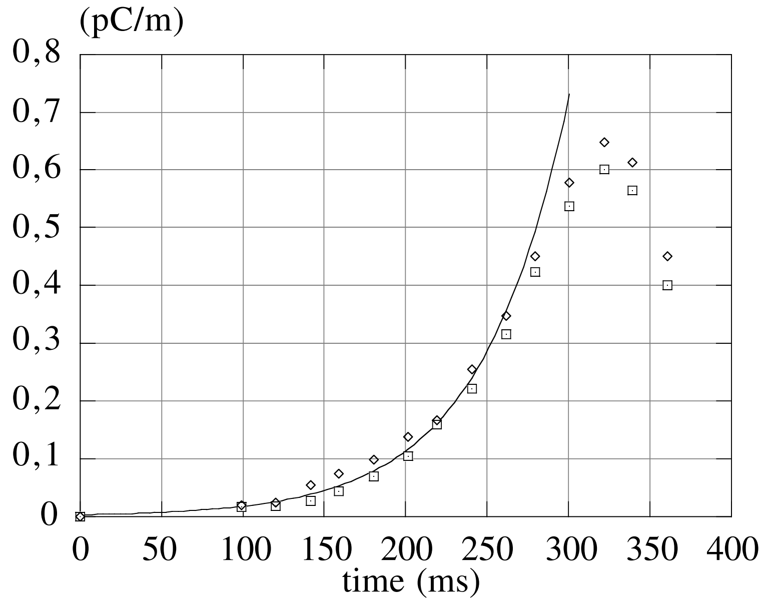

Figure 5.7: Time evolution of the first spatial harmonic of the line charge density for $\Delta f = -17.4$ kHz and $I_0 = 0.276$ mA: cold fluid model with corrected space charge impedance (–), ESR measurements (□) and particle-in-cell simulation with PATRIC code (◇).

5.4 Asymmetric wave steepening

In order to deeply understand the mechanism at the basis of the asymmetric steepening we consider the limit $|\Delta f| \to \infty$, for which analytical solutions exist. In this limit the cavity impedance is no longer effective, $\dot{Z}_{\text{cav}} \to 0$, and the machine impedance is purely capacitive. Then the system (5.26) can be rewritten as

$$\begin{cases} \dfrac{\partial \Lambda}{\partial t} + \dfrac{\partial}{\partial x}(\Lambda v) = 0 \\ \dfrac{\partial V}{\partial t} + V\dfrac{\partial V}{\partial x} + \chi\dfrac{\partial \Lambda}{\partial x} = 0 \end{cases} , \tag{5.27}$$

where the coefficient χ is defined as

$$\chi \stackrel{\text{def}}{=} -\frac{\eta}{p_0}\frac{\omega_0}{2\pi}\frac{q v_0 X_{eq}}{k_0} . \tag{5.28}$$

The parameter χ is positive definite if the particle beam is below the transition energy, $\eta < 0$, whereas it is negative above the transition energy, $\eta > 0$. Here we consider only the case $\eta < 0$, for which an analytical solution of the set (5.27) can be found.
A linearized solution of these equations is

$$\begin{aligned} \Lambda(x,t) &= [F_-(x - c_0 t) + F_+(x + c_0 t)] + \Lambda_0 \\ V(x,t) &= \frac{c_0}{\Lambda_0}\left[F_-(x - c_0 t) - F_+(x + c_0 t)\right] \end{aligned} , \tag{5.29}$$

where F_- and F_+ are, respectively, the forward and the backward line charge density waves and c_0 is their propagation velocity

$$c_0 = \sqrt{\Lambda_0 \chi} . \tag{5.30}$$

The shape of the functions $F_\pm$ depends on the initial conditions for the line charge density and the mean velocity,

$$\begin{aligned} F_-(x) &= \frac{1}{2}\left[\delta\Lambda(x,t=0) + \frac{\Lambda_0}{c_0}\delta V(x,t=0)\right] \\ F_+(x) &= \frac{1}{2}\left[\delta\Lambda(x,t=0) - \frac{\Lambda_0}{c_0}\delta V(x,t=0)\right] \end{aligned} . \tag{5.31}$$

It is interesting to observe that by choosing appropriate initial conditions we can excite either only a forward or a backward wave. For instance, by choosing $\delta V(x,t=0) = -c_0\delta\Lambda(x,t=0)/\Lambda_0$ we excite the backward wave alone (slow wave). In this case we obtain:

$$\delta V(x,t) = \frac{c_0}{\Lambda_0}\delta\Lambda(x,t) \; . \tag{5.32}$$

From (5.32) one can get the idea of solving the nonlinear system (5.27) by assuming the existence of a nonlinear algebraic relation between line charge density and mean velocity of the beam, that is $V = N(\Lambda)$. By substituting this ansatz in the Eqs. (5.27), we have

$$\begin{cases} \dfrac{\partial\Lambda}{\partial t} + \left[N(\Lambda) + \dfrac{\mathrm{d}N}{\mathrm{d}\Lambda}\Lambda\right]\dfrac{\partial\Lambda}{\partial x} = 0 \\ \dfrac{\mathrm{d}N}{\mathrm{d}\Lambda}\dfrac{\partial\Lambda}{\partial t} + \left[N(\Lambda)\dfrac{\mathrm{d}N}{\mathrm{d}\Lambda} + \chi\right]\dfrac{\partial\Lambda}{\partial x} = 0 \end{cases} . \tag{5.33}$$

Since the system (5.33) is homogeneous in the unknowns $\partial\Lambda/\partial t$ and $\partial\Lambda/\partial x$, a condition for nontrivial solution is that

$$\chi - \left(\frac{\mathrm{d}N}{\mathrm{d}\Lambda}\right)^2\Lambda = 0 \tag{5.34}$$

Therefore, we obtain for $N(\Lambda)$

$$V = N(\Lambda) = \pm 2\sqrt{\chi\Lambda} + K_0 \tag{5.35}$$

Now we want to concentrate on the solution that corresponds in the linearized model to a purely backward wave, because it can be reliably reproduced in experiments and in PATRIC simulations. Hence, we have to choose the determination with the minus sign in the relations (5.35) and $K_0 = 2\sqrt{\chi\Lambda_0}$. We obtain

$$V_+(x,t) = -2\sqrt{\chi\Lambda_+(x,t)} + 2\sqrt{\chi\Lambda_0} \; . \tag{5.36}$$

To excite this solution, we need suitable initial conditions. For small density amplitudes, Eq. (5.36) returns Eq. (5.32) to the leading order.

Now we can derive the equation for the line density $\Lambda(x,t)$. Substituting (5.36) in one of the two fluid equations, we find the nonlinear first order wave equation:

$$\frac{\partial\Lambda}{\partial t} - c_s(\Lambda)\frac{\partial\Lambda}{\partial x} = 0 \tag{5.37}$$

where

$$c_s(\Lambda) = v_s[3\sqrt{\Lambda/\Lambda_0} - 2] \; . \tag{5.38}$$

Eq. (5.37) is to be solved with the initial condition for the line charge density profile. Let us consider the unknown function $\Lambda(x,t)$ in the plane (x,t). Then the expression $\partial\Lambda/\partial t - c_s(\Lambda)(\partial\Lambda/\partial x)$ represents the total derivative of $\Lambda(x,t)$ along a curve C having the slope

$$\frac{\mathrm{d}x}{\mathrm{d}t} = -c_s(\Lambda) \; . \tag{5.39}$$

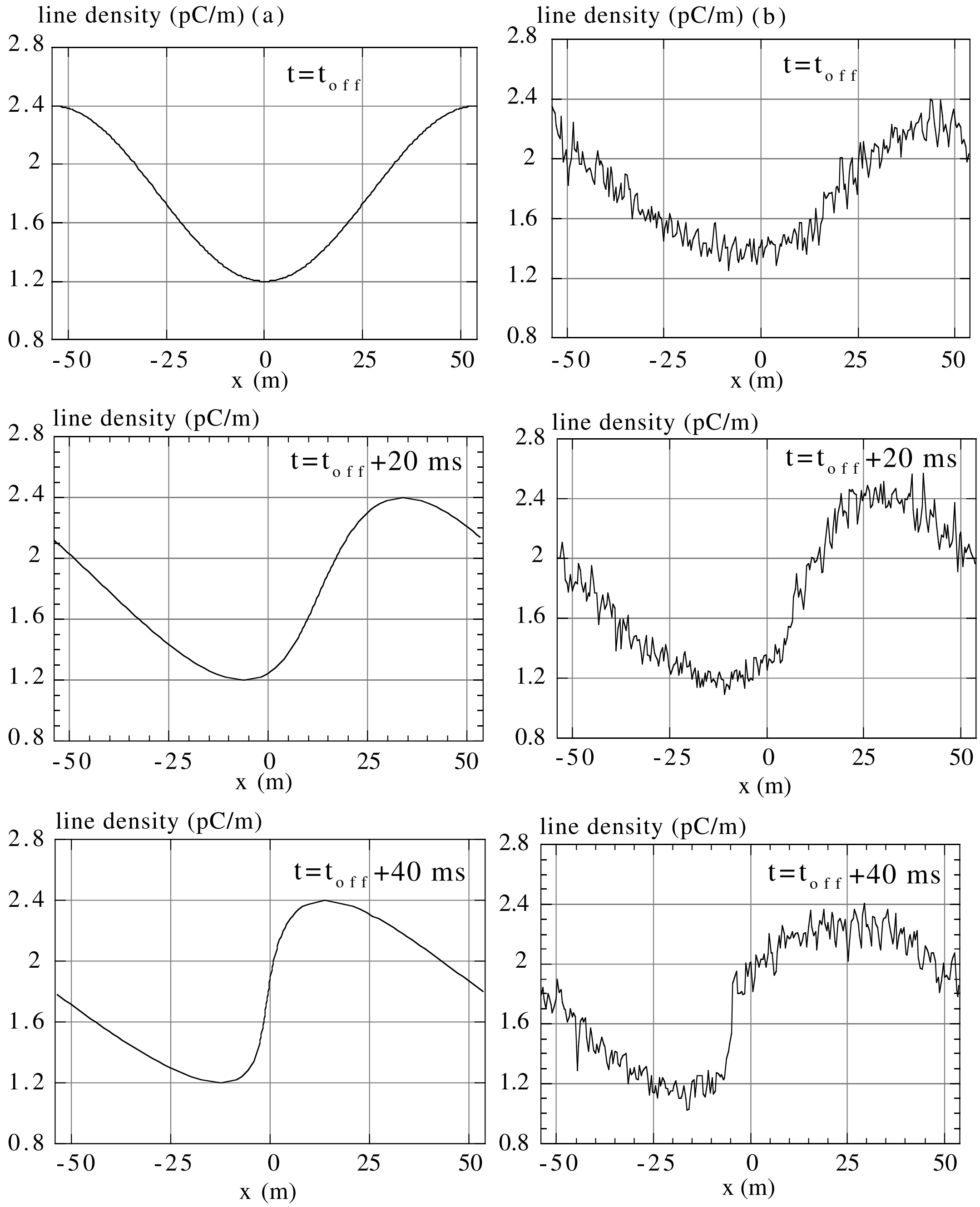

Figure 5.8: $\lambda(x, t)$ at different times for a beam interacting with the space charge impedance alone: analytical solution from the cold fluid model (a); numerical solution from PATRIC code (b).

Thus the line charge density remains constant on C. It then follows that $c_s(\Lambda)$ remains constant on C, and therefore the curve C must be a straight line in (x, t) plane with slope $c_s(\Lambda(x, t = 0))$ only depending on the initial conditions (see, for example, Ref. [57]).
Let us assume as initial condition for the charge line density profile $\Lambda(x, t = 0) = \Lambda_0 + \Lambda_1 \cos(k_0 x)$. The solution of Eq. (5.39) is given by

$$\Lambda(x, t) = \Lambda_0 + \Lambda_1 \cos\left[k_0(x + c_s(\Lambda(x, t))t)\right] \ . \tag{5.40}$$

The expression (5.40) describes implicitly a traveling wave with propagation velocities $c_s = c_s(\Lambda)$ depending on the value of Λ at a given point: the velocities of different elements of the profile are different. Since $c_s' = \mathrm{d}c_s/\mathrm{d}\Lambda > 0$, a crest in the charge density moves quicker to the left than a valley. Furthermore, the peak of the crest comes to be faster than any other region along the ring. This results in a stretching of the crest and hence steepening sets in (Figs. 5.8a). The time instant at which $\partial\Lambda/\partial x$ becomes infinite is given by $t_{\mathrm{break}} = \sqrt{(\Lambda_0 - \Lambda_1)/\Lambda_0}(2\Lambda_0/3\Lambda_1 k_0 v_s)$. Thus, for an arbitrarily small density perturbation or in the limit of vanishing beam current, $t_{\mathrm{break}} \to \infty$ and the steepening cannot be observed. The predictions of the cold fluid model are compared to the simulated density profiles resulting from PATRIC code (Figs. 5.8b). The slow wave keeps moving backward and, within about 40 ms, gets steep on the left side with no further increasing of its amplitude. Subsequently, the analytical solution (5.40) would ultimately break into a triple-valued function and our description would consequently get not physically meaningful any longer: the fluid model is inadequate when there are high spatial gradients, because kinetic effects become very important even for extremely cold beams.

The role of space charge and of the nonlinear convective terms in the formation of steepening is fundamental. Steepening is due to the resonance generation of higher order harmonics, that is, of shorter wavelength harmonics. The fundamental harmonic drives higher order harmonics through the nonlinear convective terms. Since the dispersion relation with a purely capacitive impedance is linear, the higher order harmonics as well as the fundamental one are characteristic modes of the system and, hence, constantly resonant with the driving fundamental mode: thus, the harmonic amplitudes grow in time. When kinetic effects are taken into account, higher order harmonics go off resonance before $t = t_{break}$, their growth saturates and a wave with a sharp descent forms. The importance of the broad-band impedance nature of space charge in the steepening phenomenon has been recently proven by simulating the evolution of a beam in which the space charge impedance had been substituted by a reactive impedance concentrated on one single harmonic number: no wave steepening was observed throughout over 1 s simulation time [60]. When the cavity is tuned close to the beam revolution frequency, the machine impedance for the fundamental mode is not purely capacitive anymore, but it has a real part, which in the limit case $\Delta f = 0$ is equal to R_s. For higher order modes the machine impedance stays almost purely capacitive because the cavity has a narrow band impedance and the space charge is intense. The dispersion relation is almost linear with respect to the longitudinal mode number, as in the limiting case $|\Delta f| \to \infty$. As a consequence, the resistive part of the impedance drives the exponential growth of the fundamental mode, and the convective terms drive the growth of higher harmonics through the resonant wave-wave process. The instability driven by the resistive part of the impedance produces perturbations in the line charge density so intense that steepening appears after few e-folding times.

5.5 Final remarks

In conclusion, longitudinal instability experiments far from the stability boundary performed for applications in high-current particle accelerators have clearly demonstrated growth of the slow wave, steepening, generation of higher harmonics and saturation. The theoretical analysis of the unstable evolution based on the fluid model explains and predicts the beam dynamics - the more successfully, the farther we are from the stability boundary - not only in the linear phase of the evolution (by adding a corrective term to the space charge impedance taking into account the effects of the longitudinal kinetic pressure), but also later, when the unstable mode amplitude has grown so large that strong nonlinear effects appear. If the beam is space charge dominated, the dispersion relation for the waves is almost linear, higher order harmonics driven by the unstable mode through

the convective terms stay resonant with it and wave steepening is produced within few e-folding times. Nonlinear saturation of the instability growth occurs because most of the particles end up trapped in the potential well of the wave; hence, this phenomenon cannot be predicted starting from a fluid description of the beam evolution.
In future work a challenging application of the longitudinal fluid model could be to allow identification of solitary waves, which have been theoretically predicted for high currents particle beams in linear accelerators [56, 61].

Chapter 6

Long term evolution of the longitudinal instability

As observed in Chap. 4, any coasting beam longitudinal instability causes degradation of the beam quality, and its effects do not simply disappear after the early nonlinear phases but stay remarkable in the beam structure still for a long time. The study of the long term development of the longitudinal instability is highly challenging and quite hard to deal with, because all the related phenomena are strongly nonlinear and cannot be studied within the standard methods of the perturbative analysis. As we have already seen in the previous chapter, some times well-established techniques coming from plasma physics might be employed to gain a deeper insight into the nonlinear stage of the evolution. Although many aspects of this dynamics are still mostly unknown and presently under study, we will report in this chapter about the first steps taken into this direction. Analytical models are still missing, but the use of numerical tools, together with a good diagnostics on their results, can show us the features of the long term dynamics and, consequently, the way that is to be followed for an analytical understanding. The long time character of the collective phenomena in which we are interested pose high demands on the numerical integration method. That's why, besides the PATRIC code, which has been anyway upgraded in order to account for electron and laser cooling and for intra-beam scattering, the direct "noise-free" integration of the Fokker-Planck equation on a grid in the longitudinal space has been developed as a new investigation tool [60]. This has successfully helped simulate the long time behavior of experimental observables like the momentum spread or the self-bunching amplitudes.
The effects of electron cooling and space charge are especially pointed out in the forthcoming sections.

6.1 The Fokker-Planck equation and the numerical schemes for its resolution

The beam longitudinal dynamics is satisfactorily described by the Vlasov equation as long as we decide to neglect effects coming from artificial cooling (electron or laser cooling) or from ion-ion collisions that cause diffusion (the so-called IBS, Intra-Beam Scattering). In fact, the results obtained from the Vlasov theory are reliable, provided that all the studied phenomena evolve on a time scale which is small with respect to the cooling and to the diffusion times due to external actions or to collisions. But this limitation of the kinetic description can be easily removed by simply adding to the RHS of the Vlasov equation (2.50) a Fokker-Planck term that can account both for electron cooling - modeled as a

pure friction force acting on the ions - and for IBS [42, 60]. For laser cooling, too, it is still possible to demonstrate that a first derivative Fokker-Planck term is required in order to take its effects into account [62]; nevertheless, hereafter we are not going into the details of the laser cooling global effects on the beam longitudinal dynamics (see next chapter), but we limit ourselves to discussing the effects of electron cooling and high space charge, as they both were present in the measurements described throughout this work.
By adding a RHS different from zero to the Vlasov equation (2.50) according to the prescriptions of the general kinetic theory for plasmas [42, 63, 64], we get

$$\frac{\partial f}{\partial t} + u\frac{\partial f}{\partial x} - \frac{q}{m^*}\frac{\phi(x,t)}{2\pi r_0}\frac{\partial f}{\partial u} = \frac{\partial}{\partial u}\left(\frac{F_{\mathrm{e-cool}}}{m^*}f\right) + D\frac{\partial^2 f}{\partial u^2} \,, \tag{6.1}$$

with the electron cooling force $F_{\mathrm{el-cool}}$ and the diffusion term coefficient D. In its simplest form, $F_{\mathrm{el-cool}}$ is given by

$$F_{\mathrm{e-cool}} = -m^*\beta_f u \tag{6.2}$$

with the friction coefficient or cooling rate β_f. The diffusion coefficient to be used in a given simulation can be easily calculated if we know both the cooling rate and the equilibrium momentum spread. As a matter of fact, we know that, when the beam reaches an equilibrium state due to the balance between electron cooling and IBS, the beam velocity (and momentum) distribution is Gaussian, and has a spread that is linked to the cooling and diffusion parameters by the relation:

$$\sigma_u^2 = \frac{1}{2\pi r_0}\int_{-\infty}^{\infty} u^2 f_0(u)\,\mathrm{d}u = \frac{D_0}{\beta_f} \tag{6.3}$$

Being diffusion a process related to the frequency of the ion-ion collisions, it is quite intuitive that it is strongly influenced by the distribution of the beam in the ordinary space. Actually, the diffusion coefficient scales like the beam density, so that it is easy to re-evaluate it throughout a simulation process, as the beam undergoes changes in its configuration due to collective instabilities, cooling, and space charge.
As we have already widely discussed in Chapter 3, a linear model can be set up starting from the kinetic theory (the model can even be improved by taking into account the electron cooling term in the Fokker-Planck equation (6.1), and developing a perturbative approach from that more complete equation), but its shortcoming is that it can just provide us the initial rise time of the instability. In order to make reliable predictions of inherently nonlinear experimental observables like the final momentum spread and the self-bunching amplitudes during an instability, we need to go beyond the linear theory and numerically integrate the Fokker-Planck equation together with the self-consistent electric fields.
The first numerical integration scheme that we have already used, is the particle-in-cell method (on which PATRIC is based): it makes use of a set of macro-particles randomly loaded in the (r, θ, z) coordinates and pushes them at each time step according to the external as well as to the calculated self-induced fields (see Chapter 5). It is worth mentioning here that actually the contributions of electron cooling and intra-beam scattering have been added, too, following the approach given in Ref. [65]:

$$u^{t+\Delta t} - u^t = \frac{q}{m^*}E_{\mathrm{tot}}^{t+\Delta t/2}\Delta t - \beta_f u + \sqrt{3D\Delta t}R_1 \,. \tag{6.4}$$

In this equation, β_f and D are respectively the electron cooling rate and the diffusion coefficient (which might be sensibly depending upon the beam density, and thus on time t), and R_1 is only a random number uniformly distributed between -1 and 1. The granularity

noise inherent to the PIC scheme has the undesired effect of artificially heating the beam (though this effect can be minimized by choosing a higher number of simulation particles, or through a smoothing routine operating on the electric self-fields profile). On the other side, one can take advantage of this noise caused by the fine structure of the system, and predict the Schottky noise spectrum, which is one of the most important observables. Anyhow, the problem remains that the long term evolution might be wrongly predicted because of artificial heating effects that become significant as the simulation time increases. A more elegant, but also more elaborate way to solve the Vlasov-Fokker-Planck equation is the direct integration on a grid in longitudinal phase space (x, u). This approach is 'noise-free', if we disregard the computer noise for the moment. The direct integration has the advantage of equally good resolution everywhere on the grid, whereas in the PIC code it may happen that there are not enough macro-particles in a certain phase space region to resolve a kinetic phenomenon (see for example [66]). In the followed integration scheme the full time step is split in several steps. First the Vlasov part is evolved by means of the well know time splitting scheme described in [67]. Let Δt be the simulation time step, then the splitting scheme for the Vlasov part is:
Step 1.

$$f^*(x, u, t + \Delta t) = f(x - u\Delta t/2, u, t) \tag{6.5}$$

Step 2.

$$f^{**}(x, u, t + \Delta t) = f^*(x, u + \frac{\eta}{\gamma_0 m} E^* \Delta t, t + \Delta t)$$

Step 3.

$$f(x, u, t + \Delta t) = f^{**}(x - u\Delta t/2, u, t)$$

The interpolation is done by means of cubic splines. The space charge field and the beam loading field are updated using the fast Fourier transformed Λ and the equation

$$E_n^* = \frac{v_0}{2\pi r_0} Z_n \Lambda_n^* \tag{6.6}$$

In the case of the Vlasov equation, that means in the 'collision-free' case, $f(x, u, t + \Delta t)$ is the final distribution function. For the Vlasov-Fokker-Planck equation we still have correct f for the friction and diffusion terms. Let f_j^t be the distribution function resulting from the Vlasov step at a grid point $u_j = j\Delta u$ along the velocity axis. The final distribution function $f_j^{t+\Delta t}$ is calculated by using the time implicit scheme. This completes the time step.

$$\begin{aligned} f_j^{t+\Delta t} = f_j^t &+ \frac{\Delta t}{2m^* \Delta u} \left(F_{\text{e-cool}}^{j+1} f_{j+1}^{t+\Delta t} - F_{\text{e-cool}}^{j-1} f_{j-1}^{t+\Delta t} \right) \\ &+ \frac{\Delta t D}{(\Delta u)^2} \left(f_{j+1}^{t+\Delta t} - 2 f_j^{t+\Delta t} + f_{j-1}^{t+\Delta t} \right) \end{aligned} \tag{6.7}$$

6.2 Long time beam dynamics

Simulations based on the method of the direct integration on a phase space grid have been carried out to have a clearer insight in the long term evolution of the beam used in the ESR experiments. In the above equation (6.6), two contributions to the total impedance have been considered,

$$Z_n = Z_{\text{cav}} + Z_{\text{sc}} = \frac{R_s}{1 + \mathrm{i}Q(n\omega_0/\omega_r - \omega_r/n\omega_0)} - \frac{\mathrm{i}ngZ_0}{2\beta_0\gamma_0^2} \,. \tag{6.8}$$

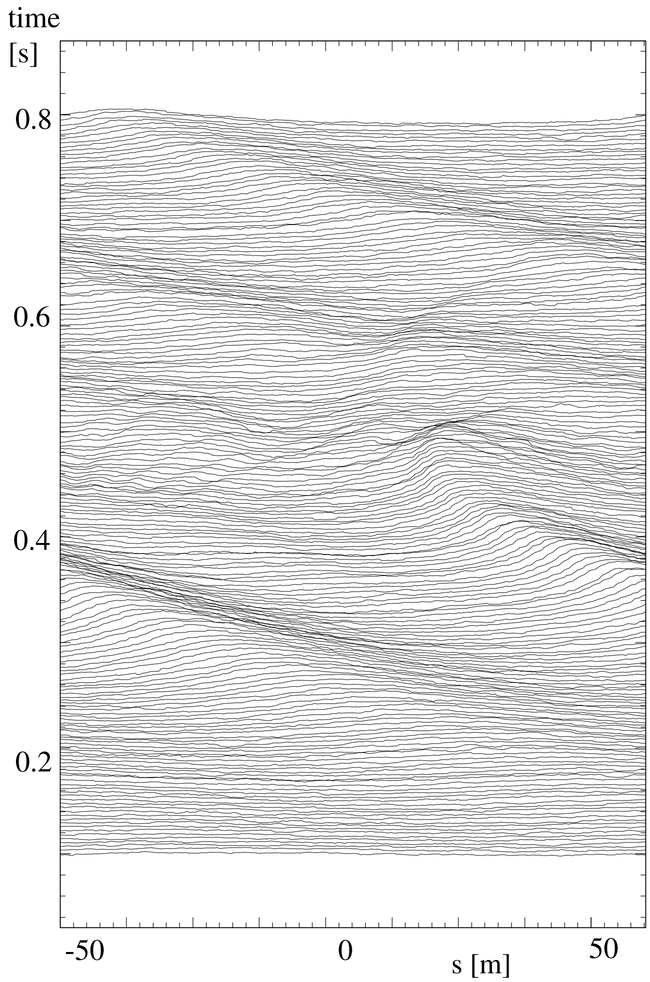

Figure 6.1: Exponential growth and nonlinear saturation phase of the longitudinal instability of the cooled coasting beam in the ESR driven by the RF cavity on the first harmonic. The plot shows subsequent time traces from bottom to top over 0.8 ms (each trace is the line density profile along the ring).

We remark here that the ESR beam, cooled down to a momentum spread of about $1.1 \cdot 10^{-5}$ (a factor 1.8 below the threshold momentum spread for instability for a fully resistive cavity impedance), was then driven unstable by tuning the cavity eigenfrequency near to the revolution frequency. In Fig. 6.1 we can observe the measured exponential growth and steepening and decay of the slow wave accompanied by smaller wave length structures. The decay of the first wave is followed by the excitation of a second wave resulting in a persistent coherent signal on the beam.

In the previous chapters, it was already shown that the measured instability growth times and current profiles up to the first wave steepening are in good agreement with the particle-in-cell PATRIC simulations. For these simulations, in which the interest was mainly concentrated on the initial phase of the instability, the effect of the electron cooling could be neglected due to the large cooling time relative to the instability growth times. Now we employ the direct integration method and focus on the long time behavior observed in

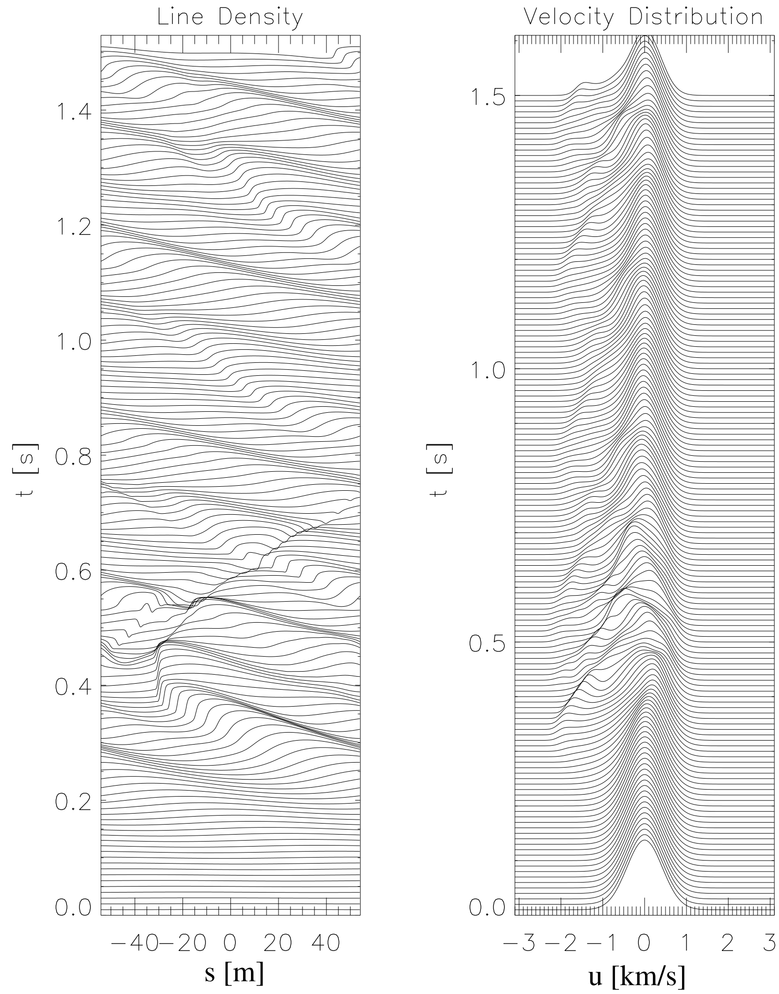

Figure 6.2: Time evolution of the line density and velocity distribution obtained from the simulations.

the experiment. In the simulations we start from the initial conditions in the experiment, assuming a Gaussian distribution function. We ignore the residual RF voltage present in the experiment. Therefore, the instability rise times will be slightly lower than in the experiment, at least for those working points very near to the condition of perfect tuning of the cavity eigenfrequency on the beam first harmonic. The cooling time chosen is 400 ms, which is much longer than the instability rise time (about 40 ms). The measured initial equilibrium momentum spread together with the known cooling time gives us the approximate IBS diffusion coefficient D, which will be used throughout the whole subsequent simulation cycle. It is very interesting to look now at Fig. 6.2, and compare it with the waterfall picture in Fig. 6.1. The similarity exhibited by the two evolutions is impressive: not only in the linear phase and in the early nonlinear stage, but even later on the simulation shows a persistent coherent signal on the beam in excellent agreement with the experimental observation. The velocity distribution does not converge to a stationary function either, but shows remaining fluctuations with a characteristic low-velocity 'foot'.

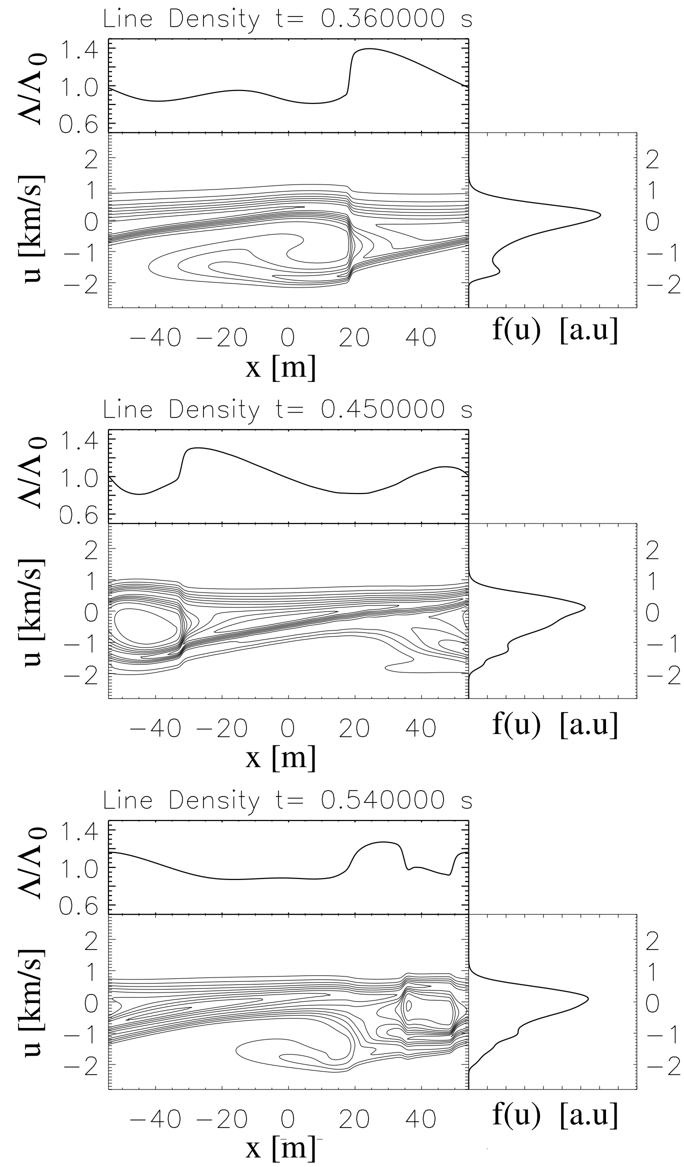

Figure 6.3: Contour plot of the distribution function together with the corresponding line density and velocity distribution obtained from the simulation.

6.2.1 Influence of space charge and electron cooling in the phase space structure of the beam

The simulation enables us to look at the detailed structure of the distribution function in longitudinal phase space. In Fig. 6.3 snap shots of the distribution function together with the line charge density Λ (divided by the initial coasting beam value Λ_0) and the velocity distribution are shown. First the slow wave steepens and decays by trapping particles in the self-excited potential. The resulting hole structure has a life time of several 100 ms before it starts to smooth out due to IBS. During this period the 'hole' causes localized line density dilutions. The excited hole structure can be regarded as a collective mode, similar to a traveling BGK wave [68] caused by non-linear Landau damping [69] in ideal plasmas. In contrast to Ref. [70] we find that due to the presence of the resistive impedance a

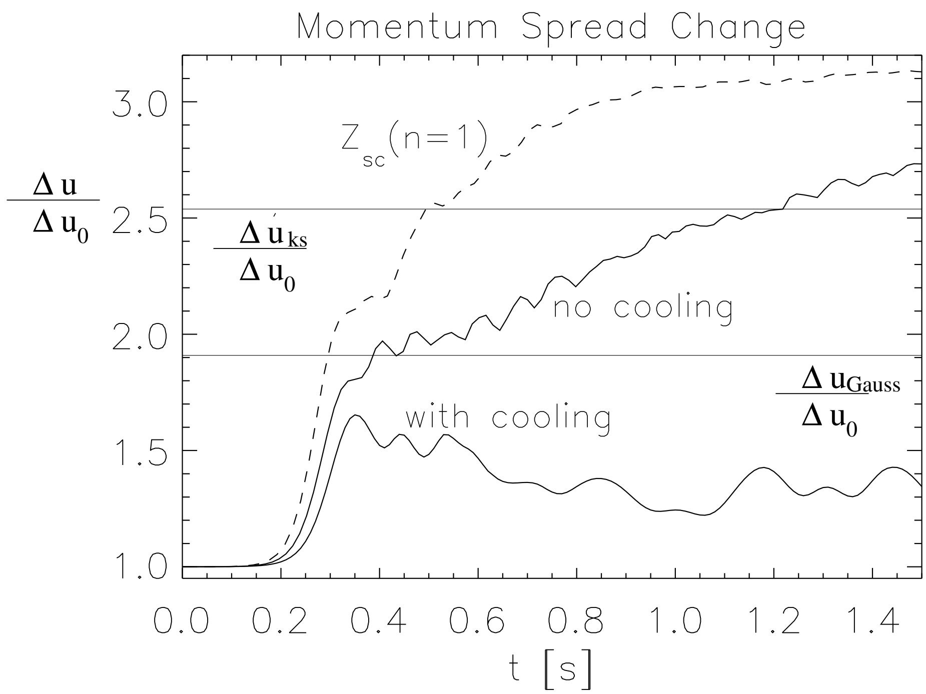

Figure 6.4: Normalized velocity spread change obtained from the simulation with and without cooling and space charge. The lower horizontal line is the threshold velocity spread for a Gaussian velocity distribution and the upper line the threshold velocity spread following from the Keil-Schnell criterion.

---

pure stationary BGK solution cannot be reached, even in the absence of IBS. The holes cause local current perturbations that continue to interact with the resistive impedance. Consequently, after the first saturation stage a second hole structure is excited (see Fig. 6.3). This hole formation continues in a cascade.

In Fig. 6.4 the resulting rms momentum spread evolution is shown (with cooling). The fluctuations of the momentum spread are caused by the continuous generation of holes in connection with the cooling force. Although the cooling rate is much lower than the instability growth rate, the saturated momentum spread fluctuates about a level which is well below the instability threshold momentum spread predicted by the linear theory for a Gaussian velocity distribution. The operating point after the saturation of the instability lies well outside the stability boundary. This 'non-linear stabilization' is due to the presence of the electron cooling. Momentum spread growth is caused by particle trapping, which is a non-linear phenomenon at finite self-bunching amplitude. The threshold momentum spread is found by equating the rise time of the instability and the cooling time. However, care must be taken since the rise time at a finite self-bunching amplitude is much lower than during the initial linear stage. Therefore the momentum spread can saturate much below the threshold value predicted by linear theory. To demonstrate the effect of cooling we switch off cooling and diffusion in the simulation. The resulting momentum spread (shown in Fig. 6.4) first seems to saturate about the threshold momentum spread, but then starts increasing continuously with a nearly linearly slope.

This continuous momentum spread growth is due to the subsequent generation of new long-lived holes structures. Fig. 6.5 shows the generation of a second 'hole' accompanied

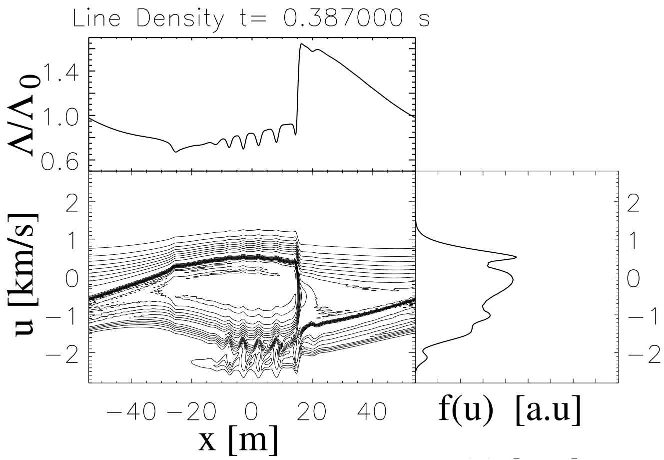

Figure 6.5: Contour plot of the phase space distribution function together with the corresponding line density and velocity distribution obtained from the simulation without cooling and diffusion.

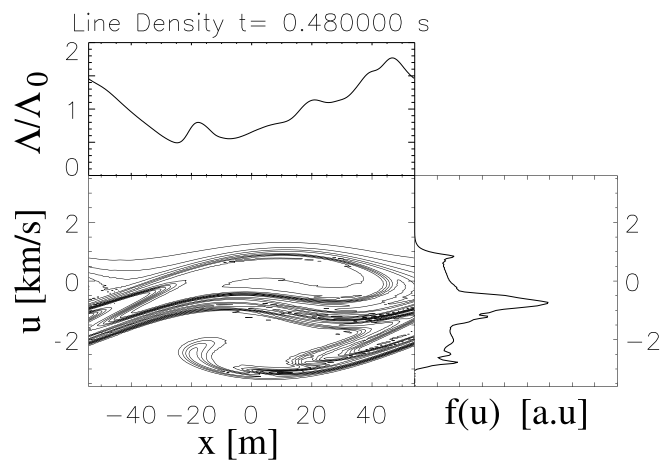

Figure 6.6: Contour plot of the phase space distribution function together with the corresponding line density and velocity distribution obtained from the simulation with space charge artificially "switched off".

by short wavelength structures, caused by space charge induced instabilities at higher harmonics. Without cooling and diffusion the wave steepening is more pronounced and higher order harmonics are stronger populated. It is noted that without cooling the momentum spread increase is accompanied by a decrease of the mean beam velocity.

In order to point out the effect of space charge on the time evolution of the instability we consider the same initial operating point, but with a imaginary impedance acting at harmonic $n = 1$ only. Thereby the space charge induced coupling of different harmonics is switched off artificially. The resulting momentum spread (see Fig. 6.4), without cooling and IBS, rapidly saturates at a level above the threshold momentum spread following from the Keil-Schnell stability criterion [9]. This is the well known 'overshoot' behavior described in several former works [71, 72]. In Fig. 6.6 a snap-shot of the distribution function can be seen showing how without space charge the self-bunching amplitudes during the exponential growth phase are much larger and no wave steepening occurs. In contrast to the evolution including space charge the effect of the instability is more destructive and no long-lived hole structures are observed. The instability causes the rapid filamentation of the distribution function and within 900 ms a saturated, uniform line density results.

In summary we find a strongly modified time evolution of the instability for space charge dominated beams in storage rings. With space charge the evolution is dominated by long-lived hole structures and the 'overshoot' behavior of the momentum spread is suppressed. Electron cooling can limit the momentum spread to values below the threshold value.

Chapter 7

Stability of intense laser cooled coasting beams

In the framework of the heavy ion fusion driver study [2] and possible high current storage and buncher rings for different applications, new interest arises on the issue of producing intense beams with very low momentum spread by using unconventional techniques. Applying laser cooling on an ion beam could certainly help for this purpose [73, 74], provided that, first, the cooling scheme is shown to be effective, and moreover it does not give rise to possible instabilities as the process goes on. New laser cooling experiments are planned to be carried out at the ESR (Experimental Storage Ring in GSI-Darmstadt), in order to study this option from the experimental point of view. The idea is to cool a very intense C^{+3} beam (number of particles reaching up to 10^{10}), $E_{kin} = 120$ MeV/U, by using a suitable laser that overlaps the beam all along the longest of the straight sections of the ESR (about 34 m). A preliminary investigation is useful to predict how the interaction between the intense ion beam and laser light affects the beam dynamics. Neglecting collisions and self-fields, we know that the beam could be ideally cooled down to the Doppler limit [74]. Therefore, only a more accurate analysis of laser cooling together with the effects of self-induced fields and diffusion coming from intra-beam scattering, is able to show how far the efficiency of the cooling process is maintained as we take into consideration more realistic situations.

In order to set up a consistent model for a beam that undergoes laser cooling, we first introduce the effects of laser light into a kinetic description of the ion beam evolution. The starting point is the expression of the radiation-pressure force acting on the ions as they propagate collinear to a laser beam, whose frequency fulfills the Doppler resonance condition [74]. In this way, the beam's longitudinal distribution function is found to satisfy a kinetic equation, which can be analytically developed through a perturbative analysis, or just numerically solved with the scheme already used for the Fokker-Planck equation [60]. The laser force as well as the diffusional term that models intra-beam scattering are also added to the forces that act on each single macro-particle in the particle-in-cell code PATRIC. Both Vlasov and PATRIC simulations are used to validate the predictions of the perturbative quasi-linear approach to the kinetic equation and to estimate the efficiency of laser cooling for the planned ESR experiment.

7.1 Kinetic modeling of a laser cooled beam

The resonant interaction of an ion beam with laser light can be used for achieving longitudinal and transverse phase-space cooling. Since the mechanism of laser cooling is such

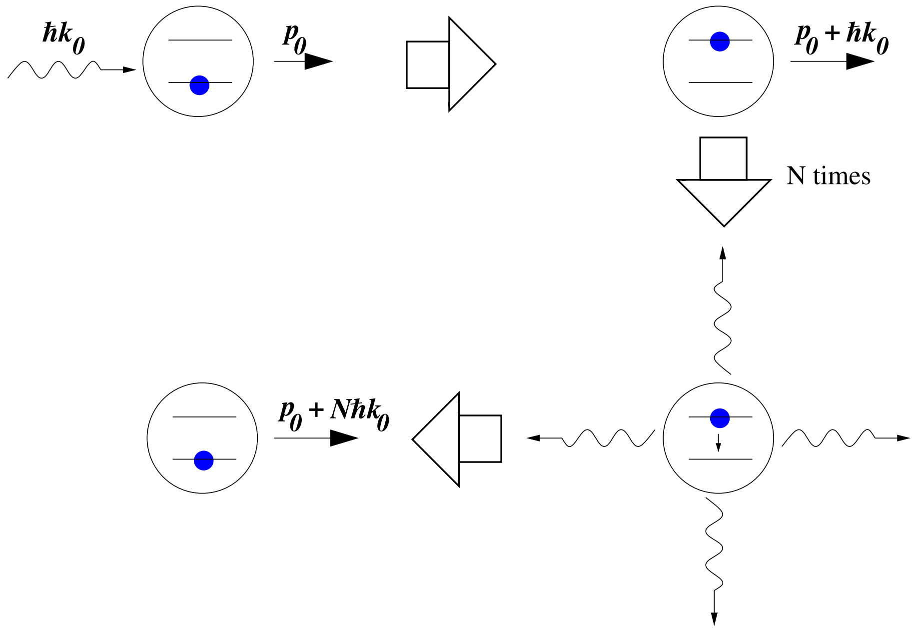

Figure 7.1: The principle of laser cooling. When a photon is spontaneously emitted by the excited ion, the ion again recoils, but the average momentum transfer after many spontaneous emissions is negligible, because the angular distribution of the emission is symmetric.

that longitudinal cooling alone can be ideally realized in absence of any interchange between the degrees of freedom of the particles in the beam[1], transverse cooling might occur only if the machine in which the beam circulates is able to properly couple transverse and longitudinal motions of the beam particles [75, 76]. In the following we are going to take into consideration the only longitudinal effect of a laser light acting on an ion beam all along an appositely designed section of a circular machine. As the interaction beam-laser has no cooling effects in itself, different and opportune schemes must be employed in order that the whole process actually results in damping of the longitudinal phase space.

Let us start now with some fundamental considerations concerning laser cooling of a coasting or bunched beam by means of the spontaneous force. As we know, the compression of the phase space density for a given particle ensemble, i.e. its cooling, requires the presence of a "dissipative force". Such a force might be originated by the dynamical effects felt by an ion as it undergoes a sequence of photon absorption-reemission cycles. In order that this can result into a net force acting on the ion in the desired direction, the reemission processes must be spontaneous. As a matter of fact, if the resonant condition between the transition frequency of the ion (assumed to be an ideal 2 level system, where only transitions between two well-defined states are possible) and the Doppler shifted frequency of the laser radiation is met, the photon is absorbed and transfers to the ion the momentum $\hbar\frac{2\pi}{\lambda_{opt}}$ – λ_{opt} being the wavelength of the electromagnetic wave in the ion rest frame – in the direction of the light propagation; then the ion spontaneously re-emits the photon in some unprecised direction within the solid angle 4π all around it, and thus might lose

[1]In reality, anisotropy between the degrees of freedom of the particles in an accelerator or storage ring, always relaxes towards a situation where the temperatures are equal in all directions, due to the Coulomb collisions

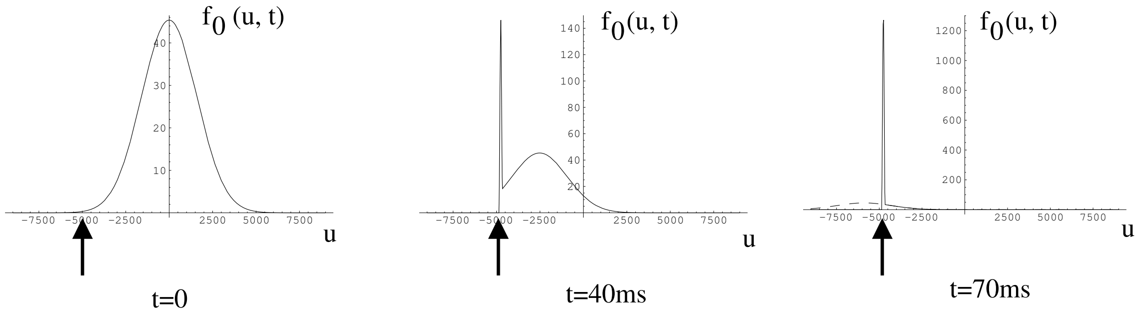

Figure 7.2: Laser cooling with a constant auxiliary force: the whole ion distribution is shifted towards the resonance with the laser, and as a result the ions are swept and confined in the neighborhood of the stable point u^*.

some of the gained momentum or even gain some more. But since the recoil momentum change connected to a sequence of absorption-reemission cycles averages to zero, the net effect on the ion after undergoing many of these cycles will simply be that it stays with the overall gained momentum (Fig. 7.1). If we consider a laser light propagating in the same direction as the ion beam, it is easy to convince oneself that the resonance condition that needs to be fulfilled is

$$\omega_{opt} = \omega_{\rm las}\gamma\,(1 \pm \beta)\ , \tag{7.1}$$

where the sign $\pm$ at the RHS depends upon whether the laser is co-propagating (-) or counter-propagating (+) with the beam. Here we can define the function $\Delta(\beta) = \omega_{\rm las}\gamma\,(1-\beta) - \omega_{\rm opt}$, which represents the deviation from the resonance condition for an ion of given velocity interacting with a co-propagating laser beam. The maximum rate at which the momentum can be transferred within such absorption-spontaneous-emission cycles in a closed two level system is given by the inverse of twice the life-time, i.e., half the spontaneous decay rate Γ of the ionic transition. If the absorption time were sharply depending on the condition (7.1), then the only particles having a β such as to fulfill that relation could interact with the laser, and hence be accelerated or decelerated by a force $\hbar\frac{\pi\Gamma}{\lambda_{\rm opt}}$. But taking into account the Lorentzian line shape of the transition - the absorption rate of the ions does not depend on β according to δ_Δ but following a Lorentzian profile - we get the more correct formula for the laser cooling force [74]

$$F_{\rm LC}(\beta) = \hbar\frac{\pi\Gamma}{\lambda_{\rm opt}}\frac{S}{1+S+\left[\dfrac{2\Delta(\beta)}{\Gamma}\right]^2}\ , \tag{7.2}$$

with S being the ratio between laser intensity I and its saturation intensity $I_{\rm sat}$. By acting on the ions of a coasting beam through the force (7.2), the laser burns only a narrow hole into the velocity distribution and piles up the shifted ions at a slightly higher velocity. This means that the laser force does not cool the beam longitudinally, unless we build up a mechanism that successively shifts ions toward the resonance condition. In order to achieve this, either the complete velocity distribution is slowly decelerated, as shown in Fig. 7.2, or the laser is progressively tuned towards higher frequencies. In both cases the effect may be described by a total force acting on each beam ion, which is the sum of the laser force plus a constant, or linearly depending on β, decelerating force:

$$F_{\|}(\beta) = F_{\rm aux}(\beta) + F_{\rm LC}(\beta)\ . \tag{7.3}$$

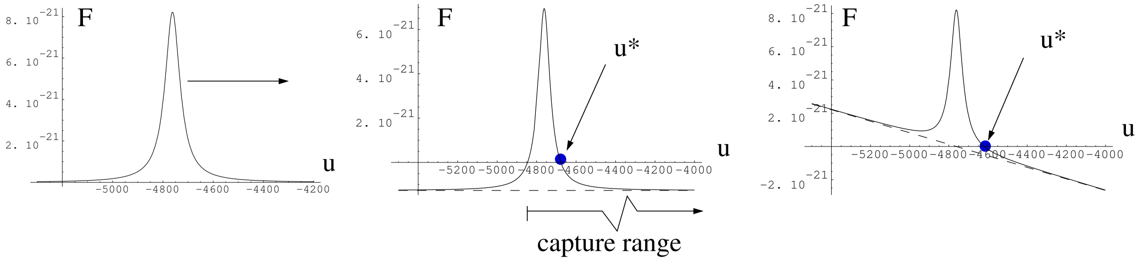

Figure 7.3: Possible cooling schemes with different auxiliary forces: (a) laser frequency chirping, (b) constant auxiliary force, (c) linear auxiliary force.

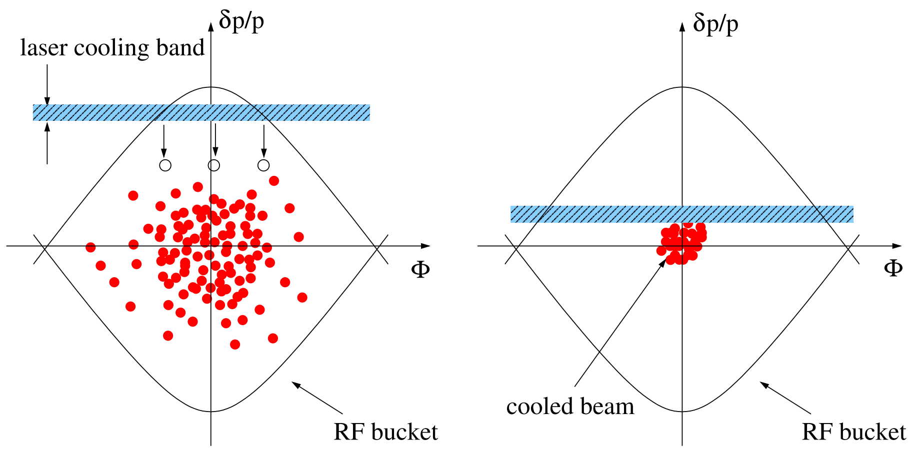

Figure 7.4: Principle of laser cooling of a bunched beam. The scanning time of the laser over the bunch must be much longer than one synchrotron period, such that all the ions can be successively pushed towards the inner core of the bunch.

It is straightforward to see that this force (7.3) has a stable point (Fig. 7.3) such that

$$F_{\|}(\beta^*) = 0\ , \qquad \left.\frac{\partial F_{\|}}{\partial \beta}\right|_{\beta^*} < 0\ , \tag{7.4}$$

which means that after the cooling process all the particles will be gathered around $v^* = \beta^*$c in a much narrower velocity span than the one in which they were spread before (actually the final spread strongly depends upon the strength of ion-ion collisions, and/or other heating mechanisms coming from the use of the laser itself [74]).

In order to cool a bunched beam, one can still use a single laser that must be initially tuned to a frequency fulfilling the resonance condition with the outermost particles in the bucket, and then shifted down to the center of the bunch, as shown in Fig. 7.4. The laser frequency must be changed slowly enough that it can sweep all the ions from the encountered synchrotron trajectories towards inner trajectories. In this way phase space compression might be easily achieved and the bunch gets globally cooled. Actually, preliminary studies based on computer simulations have clearly shown that this snow-plough technique is not strictly necessary. The laser might be tuned near the center of the bunch from the very beginning (Fig. 7.5); it will anyway sweep all the particles from the outermost trajectories to the inner ones, simply because their synchrotron motions drive

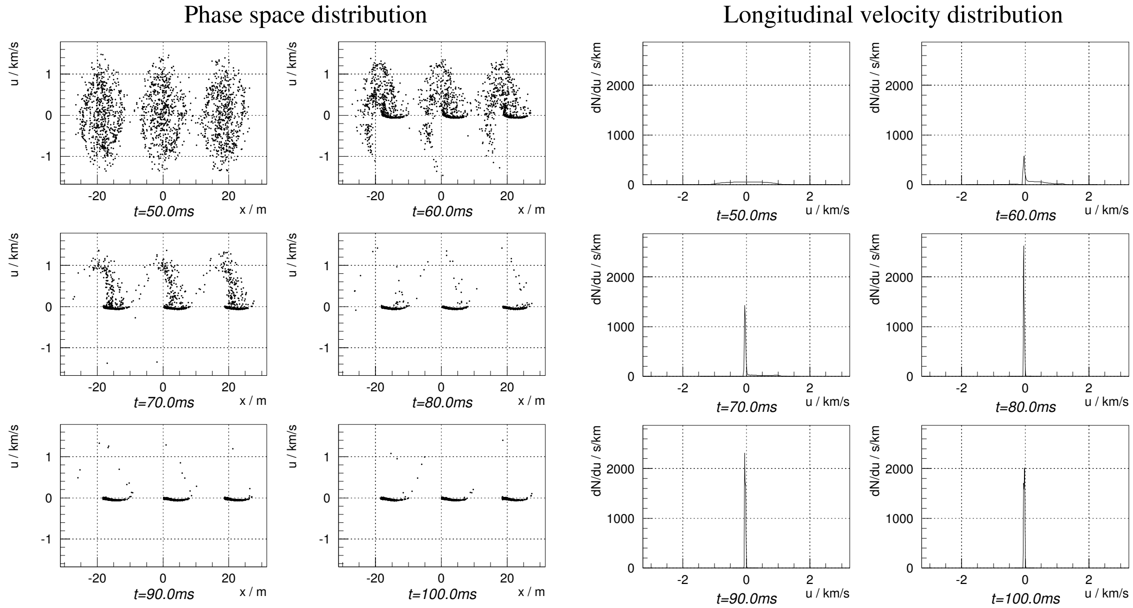

Figure 7.5: PATRIC simulation of laser cooling for a bunched beam (with a sinusoidal RF-field on the third harmonic). Here the laser frequency has been kept fixed, such that only the particles having a 2 Hz difference in their revolution frequencies with respect to the nominal one interact with the laser and are induced to the inner synchrotron trajectories.

them into resonance with the laser at some point (in a coasting beam one cannot profit from that, since the particles coast freely and have fixed velocities, not oscillating around the average value). In Figs. 7.6 and 7.7, one can observe the efficiency of this method, by comparing the details of the initial and the final states.

In storage rings, laser beam and ion beam are merged only within a fraction η_L of the ring circumference. If the velocity change of the ions in a single passage through the laser field is small compared to the natural line-width of the optical transition and the time for such a single passage is anyway long enough for reaching stationary optical excitation conditions, then we can substitute the real laser force, which is concentrated in the section s_0 to $s_0 + \eta_L 2\pi r_0$, with the ring-averaged force continually acting on the ions without committing a significant error:

$$\langle F_{\mathrm{LC}} \rangle = \eta_L F_{\mathrm{LC}} \; . \tag{7.5}$$

In order to derive the kinetic equation describing the beam longitudinal dynamics, we start from the equations of motion of the single particle, considering that the forces acting on the ion are both the self-induced and the laser cooling ones:

$$\begin{cases} \dfrac{\mathrm{d}\theta}{\mathrm{d}t} = \omega \\ \dfrac{\mathrm{d}W}{\mathrm{d}t} = qrE(\theta, r, t)\omega + \eta_L F_{\|}(\omega)\omega r \end{cases} . \tag{7.6}$$

In these equations θ is the azimuthal coordinate along the ring, ω and W the angular frequency of the ion and its energy, q is the ion charge, r the radius of the ion orbit and $E(\theta, r, t)$ the beam self-induced electric field acting back on the ion. The first assumption

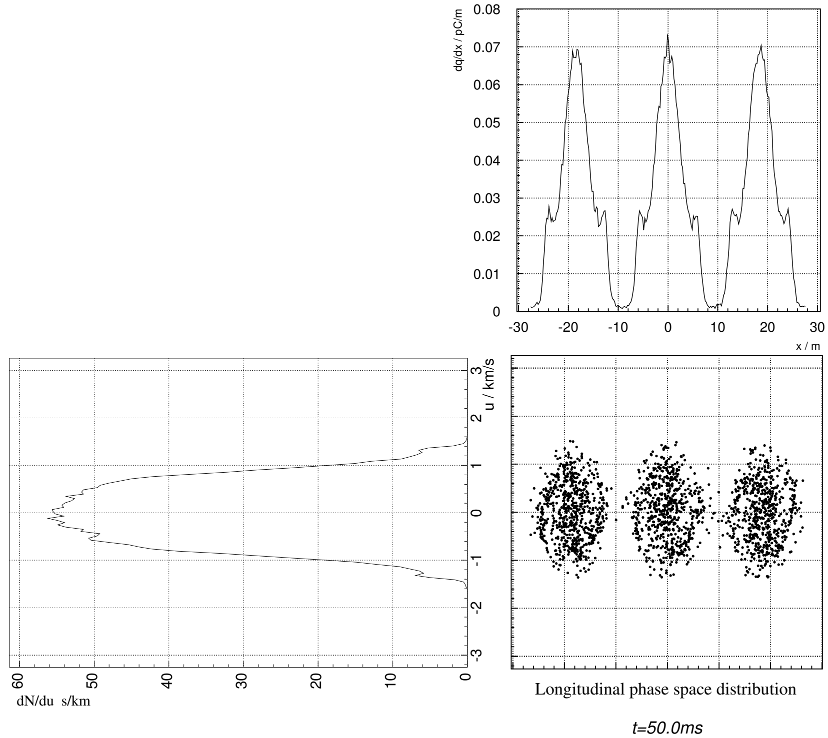

Figure 7.6: Beam distribution in the phase space before cooling starts.

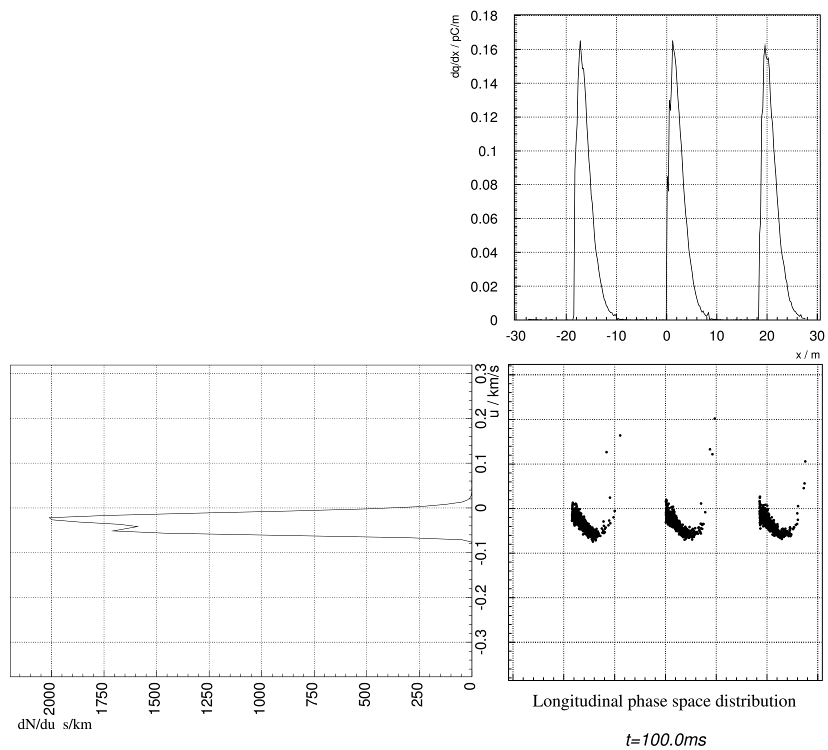

Figure 7.7: Beam distribution in the phase space after some 50 ms of laser cooling with unchanged frequency.

is that the self-induced voltage $V(\theta,t) = 2\pi r E(\theta,r,t)$ does not depend on r (cfr. Chapter 3). At this point, we can change the variables by defining

$$x_1 \stackrel{\text{def}}{=} \theta \quad , \quad x_2 \stackrel{\text{def}}{=} 2\pi \int_{W_0}^{W_0+\Delta W} \frac{\mathrm{d}W}{\omega(W)}, \tag{7.7}$$

and in this way we obtain that Eqs. (7.6) become:

$$\begin{cases} \dot{x_1} = \omega(x_2) \\ \\ \dot{x_2} = qV(x_1,t) + \eta_L F_{\|}(x_2) 2\pi r(x_2) \end{cases} . \tag{7.8}$$

Note that the orbit radius r depends on x_2 since particles having different energies perform slightly different orbits; this mechanism affects of course also the dependence on energy of the angular frequency ω, as it is clear from the presence of the slip factor η in the relation between these two quantities. As possible approximations, one might assume the orbit radius independent of the ion energy, or alternatively a linear relation:

$$r(x_2) \simeq r_0 + \left.\frac{\partial r}{\partial x_2}\right|_{x_2=0} x_2 \ .$$

After defining the two vectorial fields

$$\underline{x} \stackrel{\text{def}}{=} \begin{pmatrix} x_1 \\ \\ x_2 \end{pmatrix} \quad \underline{v} \stackrel{\text{def}}{=} \begin{pmatrix} \dot{x_1} \\ \\ \dot{x_2} \end{pmatrix},$$

it is straightforward to recognize that

$$\nabla_{\underline{x}} \cdot \underline{v} = \eta_L \left(\frac{\mathrm{d}F_{\|}}{\mathrm{d}x_2} r + F_{\|} \frac{\mathrm{d}r}{\mathrm{d}x_2} \right),$$

hence the condition for the Vlasov equation to be valid is not verified. In any case, if we introduce a particle distribution function in longitudinal phase space $f(x_1,x_2,t)$ and we use the conservation of the number of particles along a characteristic trajectory of the system (in this problem each single ion does not undergo mechanisms like collisions, which would cause instantaneous changes of the motion state)

$$\frac{\mathrm{d}}{\mathrm{d}t} \int_{\Omega} f(x_1,x_2,t)\, \mathrm{d}x_1 \mathrm{d}x_2 = 0, \tag{7.9}$$

then we can develop further this relation, put it into local form, and finally find the relation that $f(x_1,x_2,t)$ must fulfill:

$$\int_{\Omega} \frac{\partial f}{\partial t}\, \mathrm{d}x_1 \mathrm{d}x_2 + \iint_{\partial\Omega} f \underline{v} \cdot \hat{n}\, \mathrm{d}S = 0$$

$$\frac{\partial f}{\partial t} + \underline{v} \cdot \nabla_{\underline{x}} f + f \nabla_{\underline{x}} \cdot \underline{v} = 0 \ . \tag{7.10}$$

Expanding each term in (7.10), we finally obtain:

$$\frac{\partial f}{\partial t} + \omega(x_2) \frac{\partial f}{\partial x_1} + 2\pi \left[\frac{qV(x_1,t)}{2\pi} + \eta_L F_{\|}(x_2) r(x_2) \right] \frac{\partial f}{\partial x_2} +$$

$$+ \eta_L f(x_1,x_2,t) \left(\frac{\mathrm{d}F_{\|}}{\mathrm{d}x_2} r(x_2) + F_{\|}(x_2) \frac{\mathrm{d}r}{\mathrm{d}x_2} \right) = 0 \ . \tag{7.11}$$

After performing a double change of variables - $x_1 = \theta$ stays unchanged while x_2 is changed into ΔW first and finally into $\Delta\omega = \omega - \omega_0$, the equation will write

$$\frac{\partial f}{\partial t} + (\omega_0 + \Delta\omega)\frac{\partial f}{\partial \theta} + \omega_0\kappa_0\left[\frac{qV(\theta,t)}{2\pi} + \eta_L F_{\|}(\Delta\omega)(r_0 + \xi\Delta\omega)\right]\frac{\partial f}{\partial \Delta\omega} +$$

$$+\eta_L f(\theta,\Delta\omega,t)\omega_0\kappa_0\left[\frac{\mathrm{d}F_{\|}}{\mathrm{d}\Delta\omega}(r_0 + \xi\Delta\omega) + F_{\|}(\Delta\omega)\xi\right] = 0\ , \tag{7.12}$$

$f(\theta, \Delta\omega, t)$ being the new distribution function in this modified longitudinal phase space, $k_0 \stackrel{\text{def}}{=} -\eta\frac{\omega_0}{\beta_0^2 W_0}$ and $\xi \stackrel{\text{def}}{=} \frac{m\alpha r_0\gamma_0}{k_0 p_0^2}$. The last two passages that need to be carried out in order to get this Fokker-Planck equation - for dissipative forces, not for collisional phenomena - in the form we can use it for further analytical or numerical development, require its setting into the new variables s-u first (with $s \stackrel{\text{def}}{=} r_0\theta$ and $u \stackrel{\text{def}}{=} r_0\Delta\omega$), and then transform into our usual co-moving frame (with the beam) by means of the definition of the new space variable $x = s - vt$. The equation becomes so

$$\frac{\partial f}{\partial t} + u\frac{\partial f}{\partial x} + v_0 k_0\left[\frac{qV(x,t)}{2\pi} + \eta_L F_{\|}\left(r_0 + \frac{\xi}{r_0}u\right)\right]\frac{\partial f}{\partial u} +$$

$$+\eta_L f(x,u,t) v_0 k_0\left[\frac{\mathrm{d}F_{\|}}{\mathrm{d}u}\left(r_0 + \frac{\xi}{r_0}u\right) + F_{\|}(u)\frac{\xi}{r_0}\right] = 0, \tag{7.13}$$

and it might be well approximated if we assume $r(u) \simeq r_0$:

$$\frac{\partial f}{\partial t} + u\frac{\partial f}{\partial x} + \frac{qE(x,t)}{m^*}\frac{\partial f}{\partial u} + \eta_L\frac{\partial}{\partial u}\left(f\frac{F_{\|}}{m^*}\right) = 0\ . \tag{7.14}$$

In the last equation m^* represents the effective ion mass already elsewhere defined (Chapter 3).

For a linear analysis of the Eq. (7.14) we assume that the beam longitudinal distribution can be written as the sum of a slowly varying component - which is the equilibrium distribution as it is changed by the action of the laser cooling - and a perturbation on a certain harmonic:

$$f(x,u,t) = f_0(u,t) + f_n(u)\exp[-\mathrm{i}(kx - \omega\, t)] + f_{-n}(u)\exp[\mathrm{i}(kx - \omega\, t)] \tag{7.15}$$

It is clear that as long as we suppose that the spectrum of $f_0(u,t)$ does not significantly overlap with the lines at $\pm\omega$, we lose important information about the beam dynamics since we are not able to study properly the transition between stability and instability. In fact, as the beam gets cooled and its working point moves toward the instability region, there will be a time interval during which the instability that would appear is slow or of the order of the velocity compression operated by the laser. This is absolutely not taken into account when we make the assumption that the component $f_0(u,t)$ of the beam distribution function is slowly varying with respect to the remaining alternative part (no matter if ω has got a very small value). Accordingly, as a matter of fact, as long as the beam is in its stability region, the alternative components are constantly damped and the beam experiences only a reduction of its momentum spread through the action of the laser cooling. Then, as soon as the beam working point on the impedance plane crosses the stability boundary and causes an unstable motion to be excited, then all that we will observe from this moment on will be the development of the instability because in any case it will be faster than the action of the laser cooling going on. Anyhow, plugging the ansatz (7.15) into Eq. (7.14) and then separating its slowly changing part from the rapid one, we finally obtain:

$$\begin{cases} \dfrac{\partial f_0}{\partial t} + \eta_L \dfrac{\partial}{\partial u}\left(f_0 \dfrac{F_\parallel}{m^*}\right) = 0 \\ \left[\mathrm{i}\omega - \mathrm{i}uk + \eta_L \dfrac{\mathrm{d}}{\mathrm{d}u}\left(F_\parallel m^*\right)\right] f_n \exp[-\mathrm{i}(kx - \omega\, t)] = -\dfrac{q\partial f_0/\partial u}{2\pi r_0 m^*} \dot{Z}_{\mathrm{tot}}(n\omega_0) I_n \end{cases} . \tag{7.16}$$

Now, taking into account the periodicity in x of our structure - the wave number of the perturbation k can be written as n/r_0 because the wavelength $\lambda = 2\pi/k$ must be a multiple of the ring circumference - and that the perturbation on the n-th harmonic of the beam current is (approximately) related to f by means of

$$I_{\pm n} \simeq v_0 \int f_{\pm n}\, \mathrm{d}u \cdot \exp[\mp \mathrm{i}(kx - \omega\, t)], \tag{7.17}$$

it is quite straightforward to find out that the second equation of the set (7.16) yields the following dispersion relation

$$1 = -\mathrm{i}\frac{q^2 v_0 \dot{Z}_{\mathrm{tot}}(n\omega_0)}{2\pi m^* n} \int \frac{\partial f_0/\partial u}{u - \dfrac{\omega r_0}{n} + \mathrm{i}\eta_L \dfrac{r_0}{n}\dfrac{\mathrm{d}}{\mathrm{d}u}\left(\dfrac{F_\parallel}{m^*}\right)}\, \mathrm{d}u\ , \tag{7.18}$$

whose solution gives the frequencies associated to different perturbation wavelengths (harmonic numbers n) and if they are stable or unstable, too. The $f_0(u,t)$ that appears in this relation should be of course that function which satisfies the first of the (7.16): but, as its changes are in any case slow, one can assume that the f_0 keeps changing because of laser cooling effects according to this equation as long as the beam doesn't enter the instability region defined by (7.18), and then the instability appears and the structure of the beam is altered so that the perturbative analysis does not hold any longer after a while.
It is useful to note now that the dispersion relation which we have obtained with this analysis is slightly different from the one that is usually solved for a beam that is not under the action of a cooling force (it is similar anyway to the one that corresponds to an electron cooled beam, and it would reduce to that if we simply exchanged the laser cooling force $F_\parallel(u)$ with a friction force just proportional to the velocity u). This means that the cooling does have an effect on the stability properties of the beam, as well, and we can expect a sensible variation in the stability boundary with respect to the uncooled case. The electron cooling has been proven to enlarge the stability region by opening the stability boundary towards its upper part [46]. In order to find out how the laser cooling force changes the stability boundary, a numerical solution of (7.18) for a given set of parameters is needed. Care must be taken that the beam velocity distribution function which has to be put into this equation is the one that results from the action of the laser force plus decelerating force and so it does not stay Gaussian around $u = 0$ like in the electron cooling case, but starts bump-in-tail and then gets different shapes which might change the structure of the stability boundary much more than the extra term at the denominator of the integrand. In other words, due to the snow plough effect of the cooling force, the beam might turn unstable at any moment of the laser-sweeping process, making ineffective the cooling action itself.
This evolution is studied next in great detail, and then also the results from numerical simulations with the PATRIC code are shown. The main advantage that we get from the use of the code is that it allows observing the beam dynamics under the effect of both cooling forces and self-induced fields, and thus provides us a complete picture of the process which has been so far analytically modeled just up to the linear phase.

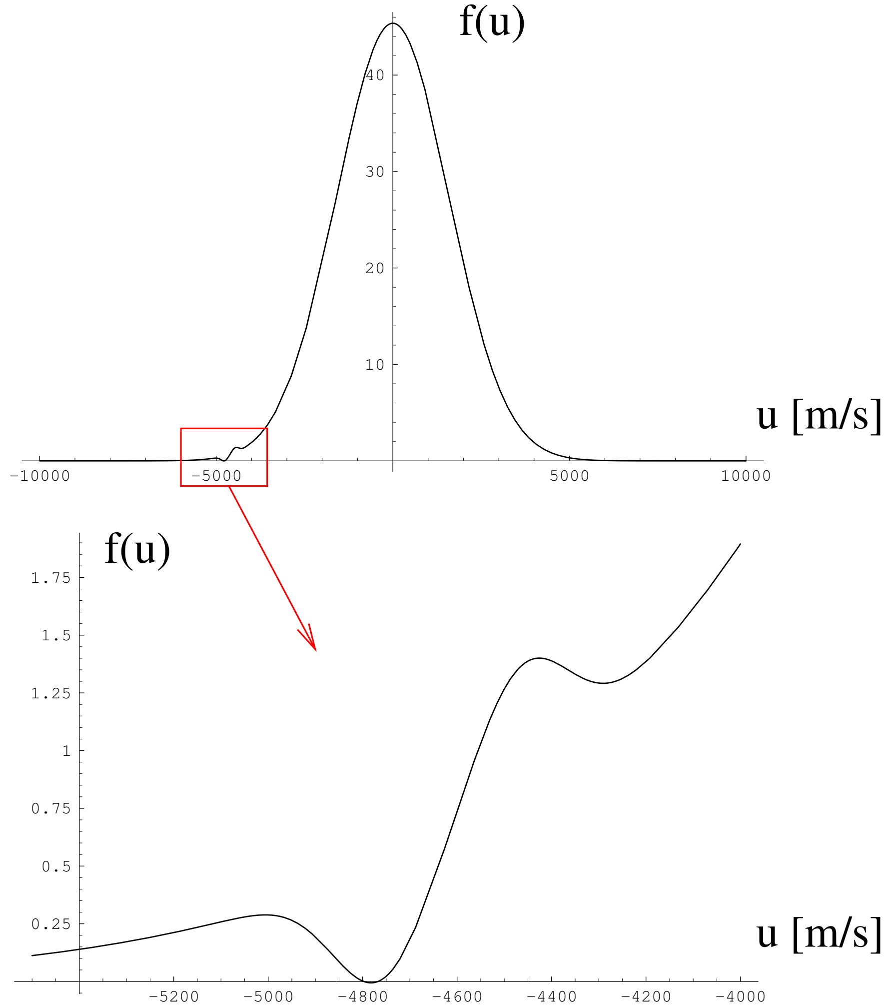

Figure 7.8: Bump-in-tail distribution function, as it results from the action of the laser on a displaced frequency. The details of the depleted zone are zoomed in.

7.1.1 Solution of the "laser corrected" dispersion relation

Eq. (7.18), together with the expressions of the components of the global laser cooling force (7.2)-(7.3), is to be numerically integrated in order to predict the stability properties of a laser cooled coasting beam (here is assumed that the beam intensity does not affect the way beam and laser interact, but can only determine the strength of the self-produced fields). On one side, we need some numerical values to plug into our relation, and for that we will refer to the parameters belonging to an experiment carried out at the Heidelberg TSR (Test Speicherring) [74], which will be listed in the following; on the other side, we must use a beam distribution function along the longitudinal velocities axis, which is consistent with the presence of the laser tuned at some frequency resonant with the particles far apart in the lower tail of this distribution.

Following what is contained in Ref. [74], we assume to have a beam of 10^7 Be^+ ions, circulating at 4% of the speed of the light ($E_{\rm kin} = 0.8$ MeV/U) with an initial momentum

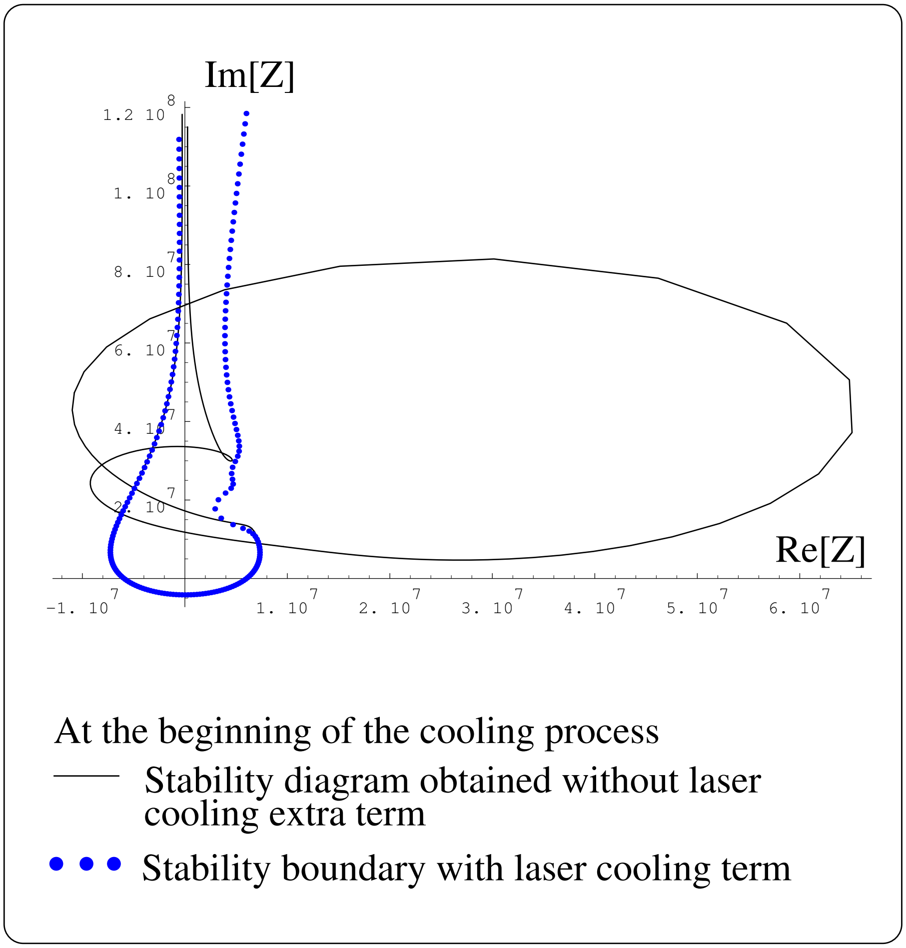

Figure 7.9: Stability boundaries for a distribution function like the one shown in the previous figure, with and without the contribution of the laser cooling extra term in the dispersion integral.

spread of about 10^{-4} without electron pre-cooling. The wave length corresponding to the optical transition for this kind of ions is $\lambda_{\rm opt} = 313$ nm, and the spontaneous emission rate of the excited upper level is $\Gamma = 1.15 \times 10^8$ s^{-1}. Since the experiments were carried out at the TSR, the machine average radius is $r_0 = 8.82$ m, whereas the beam-laser interaction fraction is given by $\eta_L = 0.09$. For the experiments reported in the mentioned paper, a laser with saturation parameter $S = 3$ and a constant auxiliary force $F_{\rm aux} = -7.9$ meV/m were employed.

As beam distribution function in the longitudinal phase plane, we choose to start from a bump-in-tail distribution (Fig. 7.8), as it occurs after the laser has already swept all the particles off the resonant velocity, and has accumulated them slightly ahead of it. As a matter of fact, the laser takes only few tenths of a millisecond to push the ions from the interaction region, whereas the auxiliary force shifts the whole distribution backwards on a time scale of tens up to a hundred milliseconds. The bump-in-tail distribution can be therefore regarded as a temporarily stationary configuration of the beam, on which instabilities having few milliseconds e-folding time can develop. At any rate, for our immediate theoretical understanding we need not take that into account, as our first goal will be to find out the stability properties of a distribution function as the one shown in

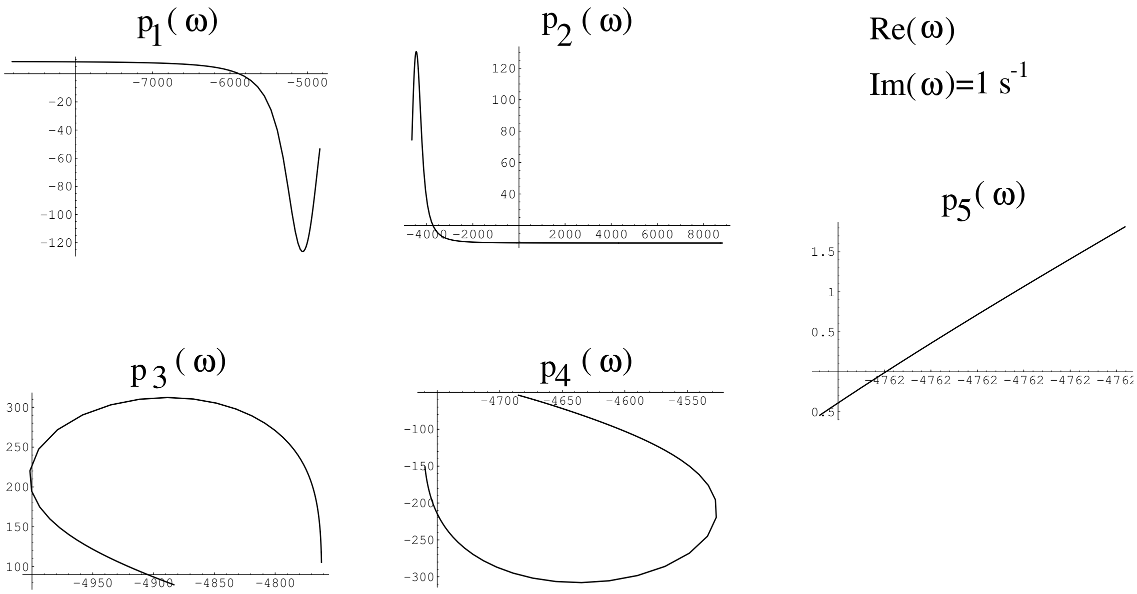

Figure 7.10: Paths of the poles of the integrand function in the complex plane, as the imaginary part of ω is kept constant at a very low value (1), and Re(ω) is made to span from -1000 to 1000.

Fig. 7.8 when one does not neglect the laser force – which has the main role of building and maintaining such a distribution function, indeed – in the study of the dynamics. If we considered, in fact, such a velocity distribution function, and we evaluated its stability boundary in the complex plane ($n = 1$, $\mathrm{Im}(\omega) = 0$) with the ordinary dispersion relation reported in Chapter 3, Eq. (2.59), we would simply obtain the strongly deformed "onion" with a side loop on the right side, as shown in Fig. 7.9 (full line). Stability would be lost throughout a big slice of the internal region, and this is perfectly understandable from the kinetic point of view. An interval of slow wave phase velocities cannot profit from Landau damping because of the lack of particles in the "bumped" region: for this phase velocities, the slow wave will be always unstable, no matter how small is the resistive part of the impedance acting on the beam. The practical effect of such an instability would be to develop an electric field that would very soon refill the dip, and let the beam evolve towards a stable situation thanks to the re-gained regular velocity distribution. It is evident that, if the laser is instead acting on the beam, the stability of the bumped distribution function is expected to be enhanced, since the ions which would diffuse to fill the hole due to the self-induced fields, will actually keep being pushed back by the action of the laser. The stability diagram that one obtains by using the corrected dispersion relation (7.18) is shown in Fig. 7.9 as a sequence of thick points. The expected stabilizing effect of the laser is visible throughout the whole region of resistive impedances. For the computation of this stability diagram in Fig. 7.9, special care has been needed, because the function in the dispersion integral has five poles that must be calculated for each real ω (because we are searching for the stability boundary, $\mathrm{Im}(\omega) = 0$ - in reality we set $\mathrm{Im}(\omega) = 1$ in our computation) by solving the nonlinear equation:

$$u - \omega\frac{r_0}{n} + \mathrm{i}\frac{r_0}{n}\frac{\mathrm{d}F_{LC}/\mathrm{d}u}{m^*} = 0\,. \tag{7.19}$$

The algorithm used for doing that has consisted first in figuring out the five roots for $\omega = -1000$ with the method of the function mapping (it is a complex equation, in fact), and then using them as initial values for the subsequent numerical evaluations of the roots as $\mathrm{Re}(\omega)$ was varied little by little up to 1000. The paths of the poles in the complex plane as $\mathrm{Re}(\omega)$ was brought from -1000 to 1000 are shown in Fig. 7.10. The main difference with respect to the ordinary case is that now the imaginary part of the poles also changes when the real part of ω alone changes. This was not the case when the equation for the poles was purely:

$$u - \omega \frac{r_0}{n} = 0 \,, \tag{7.20}$$

because then, once the value of the imaginary part of ω had been fixed, also the imaginary part of the pole was automatically fixed at the same value (see Fig. 7.11). As we can draw out from Fig. 7.10, there are two poles that reverse their sign as $\mathrm{Re}(\omega)$ spans in $(-1000, 1000)$, $p_1(\omega)$ and $p_5(\omega)$. As we can see after calculating the residues in both these points, the contribution coming from the quasi-stationary pole $p_5(\omega)$ is negligible, whereas the contribution of $p_1(\omega)$ plays a key role. By evaluating $p_1(\omega)$ for $\mathrm{Im}(\omega) >> 0$ (very unstable case - all the poles that give a contribution in this case should be always taken into account), one sees that p_1 has an imaginary part definite positive, which means that its contribution must be always accounted for, even after it crosses the real axis and goes down for some values of ω. The physical meaning of this pole crossing the real axis for some values of the slow wave frequency shift is not so clear as the Landau damping becoming dominant for the pole crossing the real axis in the ordinary case. Anyway, this is very likely to be associated with a particle-wave-laser interaction effect, as in the case without laser cooling Landau damping, which is a pure particle-wave interaction, sets in as the imaginary part of the pole reverses its sign (the real part of the pole changes sign, indeed, if we refer to the formalism presented in Chapter 3). A deeper interpretation of this phenomenon is presently still subject of study and further investigation.

Fig. 7.12a shows the beam velocity distribution after some 30 ms cooling, and the corresponding stability boundaries in both cases where we neglect the contribution of the laser extra term in the dispersion relation and when it is taken into account, too. There is clearly an enlargement of the stability region when the corrected dispersion relation is solved; due to the steep structure of the distribution function in Fig. 7.12a the stable region would normally shrink down to the almost invisible (in the considered scale) zone around the origin of the impedances (Fig. 7.12b).

The meaning of these considerations is evident: thanks to the laser continuously acting on the beam during cooling, high space charge impedances and even quite large resistive impedances become tolerable, and they should not be expected to drive the beam unstable because of two-stream, or similar, phenomena. The destabilizing effect which would be produced by the distortion of the beam velocity distribution function is in fact compensated by the laser that keeps on pushing ions away from the region with the dip.
Numerical check of these analytical conclusions is necessary, and reported in the following section. But before, in the next subsection, we shall briefly discuss as a starting point, the way laser cooling has been introduced into our simulation tools (PATRIC and Fokker-Planck solver).

7.1.2 Numerical approach

Our particle-in-cell code PATRIC is a general tool to study the longitudinal dynamics of space charge dominated beams under the influence of the ring environment modeled

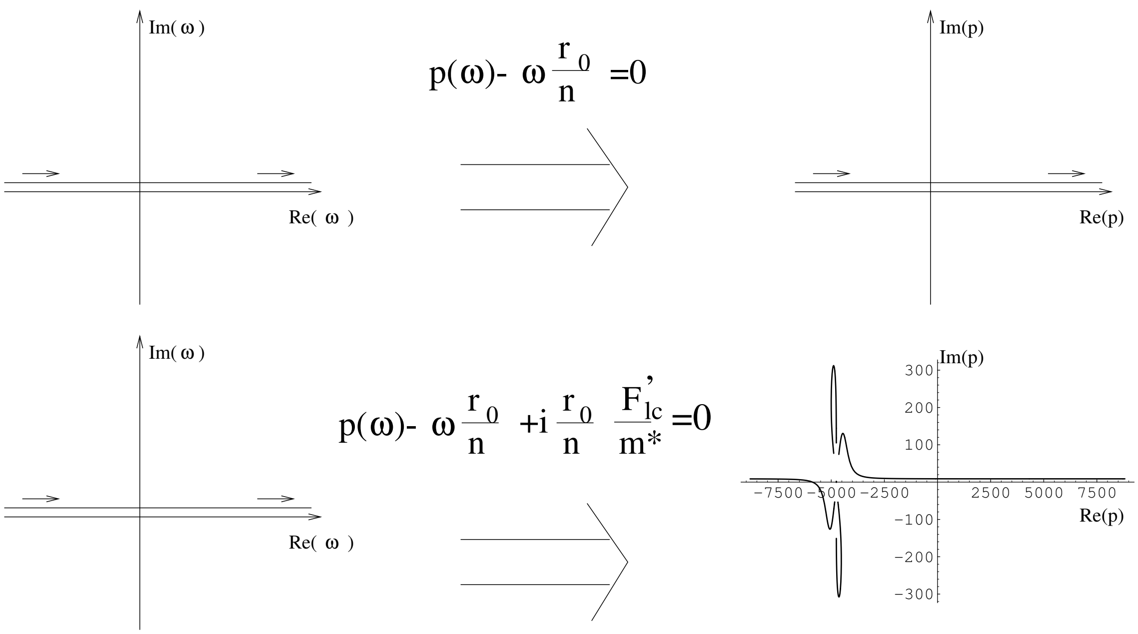

Figure 7.11: Comparison between the simple path of the sole pole present in the ordinary dispersion relation, and the paths of the five poles present in the dispersion relation inclusive of the laser cooling contribution, too.

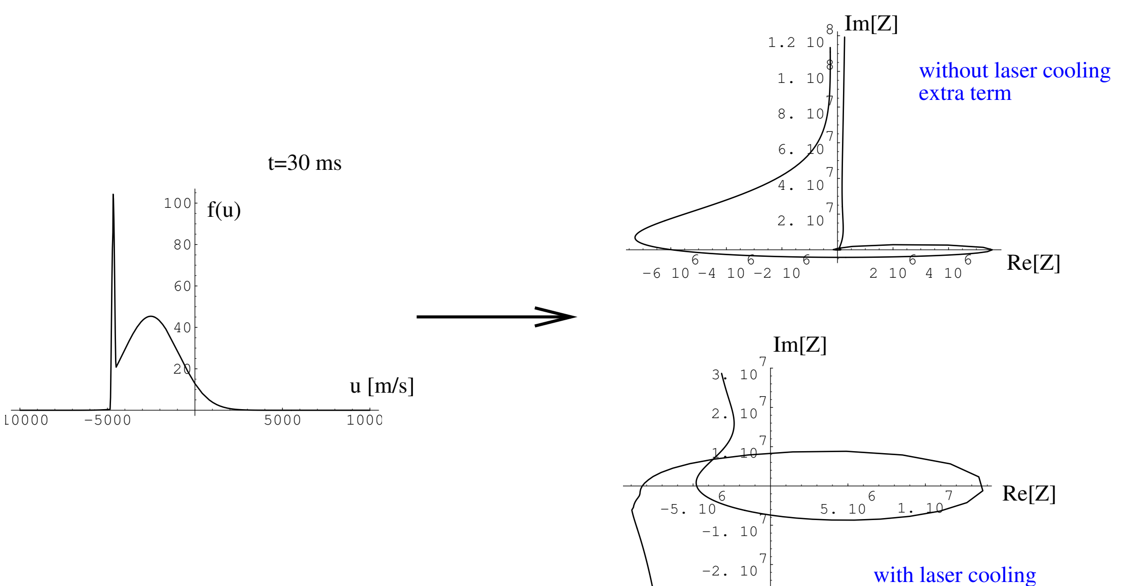

Figure 7.12: Beam velocity distribution after 30 ms cooling, and corresponding stability boundaries with and without laser cooling extra term.

through a general impedance $\dot{Z}_{\rm tot}(\omega)$ and arbitrary external RF fields. The beam is represented by a number of macro-particles interacting via space charge and the ring impedances (Section 5.1). External forces can be easily added when updating the macro-particles velocities after one time step; intra-beam scattering (IBS) is also taken into account following Ref. [65]. For the longitudinal motion one updates the velocity according to:

$$u^{t+\Delta t} - u^t = \frac{q}{m^*} E_{\rm long}^{t+\Delta t/2} \Delta t + \frac{F_\parallel}{m^*} \Delta t + \sqrt{3D\Delta t} R \, , \tag{7.21}$$

where D is the diffusion constant, R represents a random number uniformly distributed between -1 and 1, and $F_\parallel$ is the laser cooling force (radiation pressure force plus auxiliary force).

Another way to solve Eq. (7.14) along with a Fokker-Planck term taking into account of collisions, is direct integration on a grid in longitudinal phase space (x, u) (cfr. previous chapter).
Over one time step, first the Vlasov part must be evolved by means of the time splitting scheme, and secondly, the distribution function f coming from the 'collision-free' part is to be corrected for the cooling and diffusion terms. Let f_j^t be the distribution function resulting from the Vlasov step at a grid point $u_j = j\Delta u$ along the velocity axis. The final distribution function $f_j^{t+\Delta t}$ is calculated by using the time implicit scheme. This completes the time step.

$$\begin{aligned} f_j^{t+\Delta t} &= f_j^t + \frac{\Delta t}{2m^*\Delta u} \left(F_{\parallel j+1} f_{j+1}^{t+\Delta t} - F_{\parallel j-1} f_{j-1}^{t+\Delta t} \right) \\ &+ \frac{\Delta t D}{(\Delta u)^2} \left(f_{j+1}^{t+\Delta t} - 2 f_j^{t+\Delta t} + f_{j-1}^{t+\Delta t} \right) \end{aligned} \tag{7.22}$$

7.2 Simulated evolution of a laser cooled coasting beam

In this section we will mainly use the tools previously discussed for a couple of applications.
First, the stability properties of a laser cooled beam at the very beginning of the cooling process, which are to be read in the diagrams of Fig. 7.13, can be easily checked running a beam simulation over a reasonably long time (few hundreds of ms) for points A, B, C and D. These points in the impedance plane have been reached by having an adequately detuned cavity act back on the beam. Simulating the beam evolution in these cases, we observe that the beam keeps stable for points B, C and D. On the other hand, when the working point is chosen to be A, an initial perturbation grows unstable over a 100ms time. In the cases when the beam was stable, one could observe that the velocity distribution stays bump-in-tail all over the simulation time: this confirms that no "diffusive" instability appears, which would eventually develop a stabilizing tail, as quasi-linear theory foresees [63]. This is not surprising, in fact, because (7.18) also accounts for the action of the laser force, which can permanently counterbalance every diffusive mechanism over the dip.

Secondly, we can use the parameters of the experiment planned at the ESR (see in the introductory section of this chapter) and simulate with them two different laser cooling schemes: (a) constant auxiliary force and (b) linear force, which could be provided by the electron cooler (Fig. 7.14). Fig. 7.15 shows how the beam momentum spread shrinks with the cooling. Apparently both schemes, neglecting the effects of intra-beam scattering, eventually lead to a one order of magnitude reduction in the spread. The fact that a final

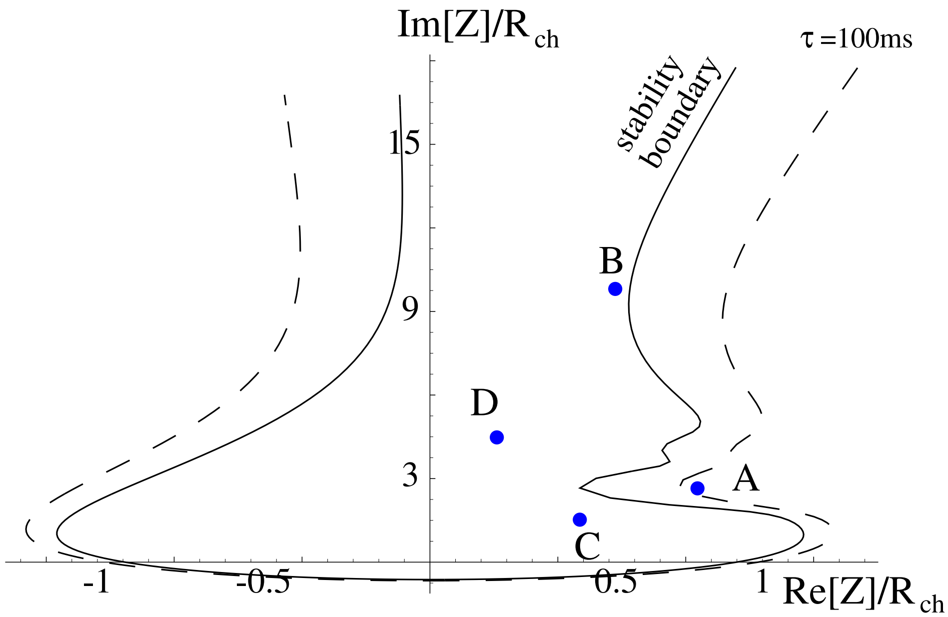

Figure 7.13: Stability boundary and one unstable curve (instability rise time is 100ms) for a Gaussian beam with a laser acting on the particles with $u = -3\sigma_V$. A, B, C and D represent the working points that have been simulated.

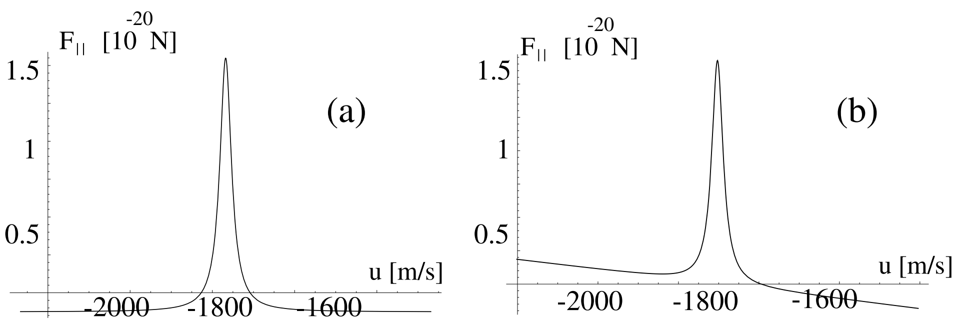

Figure 7.14: External longitudinal forces acting on the ions: (a) laser force plus constant decelerating force and (b) laser force plus friction force.

cooled beam configuration is reached in both cases, means that, in spite of the high beam intensity, no space charge induced instabilities are able to destroy the cooling process before. The only differences are in the cooling time, which is far shorter when the linear force is employed, and in the particles in the tail of the distribution, which would be lost in the constant force scheme, as they lie outside its capture range, but would be gathered instead with the other system. If we switch on diffusion due to ion-ion collisions, we soon realize that the cooling scheme (a) becomes ineffective (it can nevertheless be successfully employed if the band of the laser force is artificially broadened [77]), whereas system (b) still works but only stops to a reduction of a factor about 1.6 in the spread (Fig. 7.16). Fig. 7.17 shows the velocity distribution functions as they eventually appear after 85ms cooling. A two fluids structure of the beam, made up of a cooled part and a hot

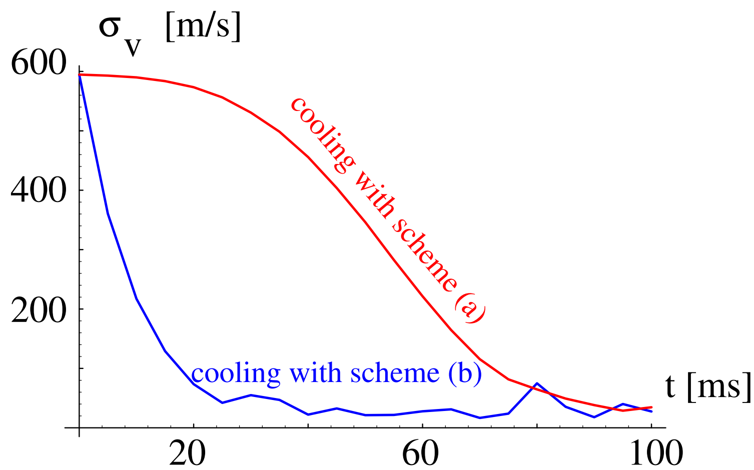

Figure 7.15: Absolute velocity spread vs. time for the cooling schemes (a) and (b).

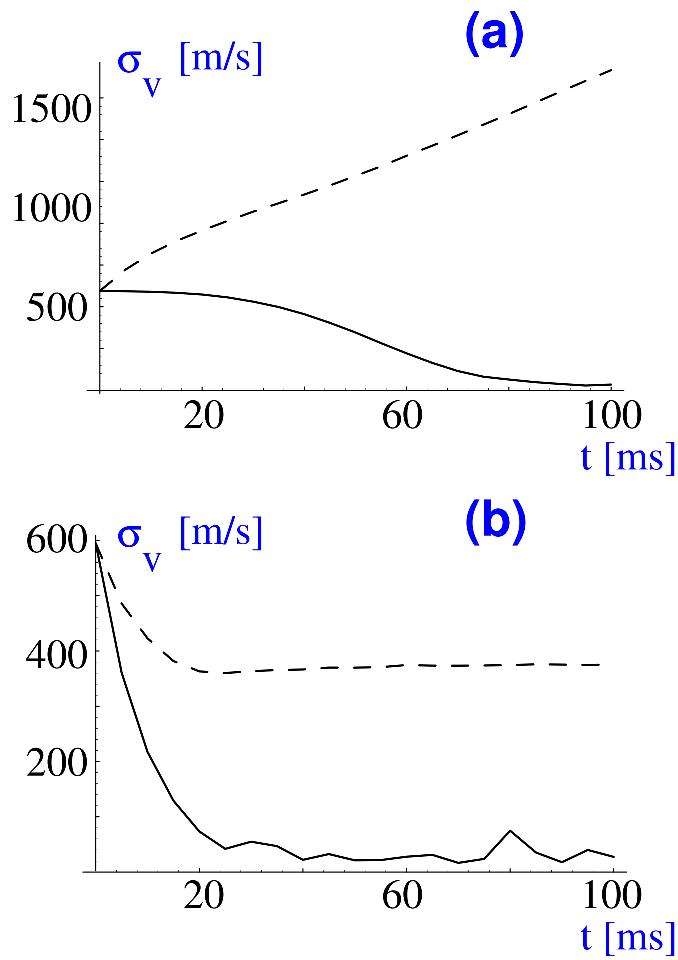

Figure 7.16: Absolute velocity spread vs. time considering IBS (dashed line), or not (full line). The above picture refers to the cooling scheme (a), and the one below to the cooling scheme (b).

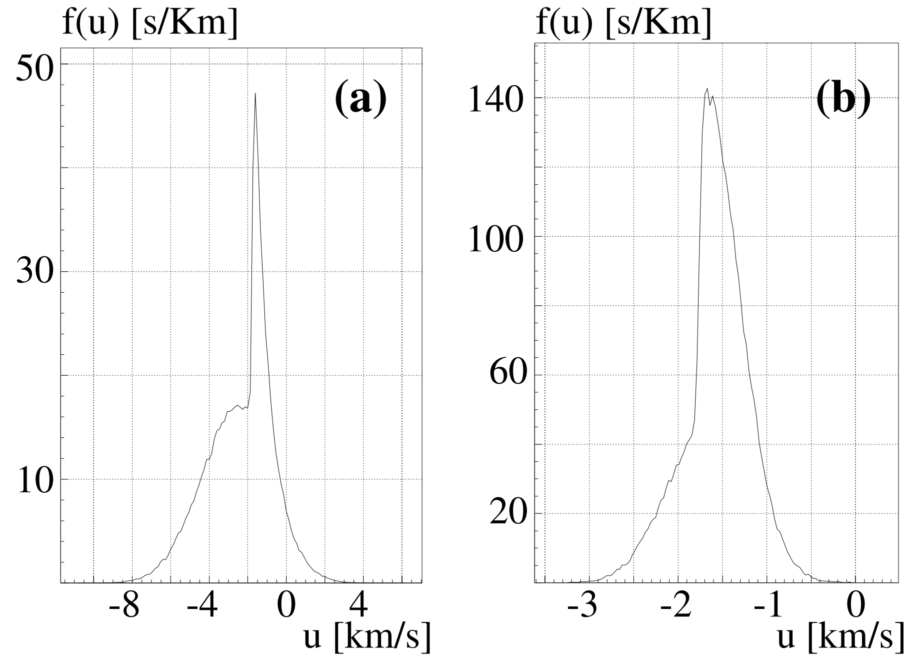

Figure 7.17: Velocity distribution functions of the beam after 85ms of laser action.

background due to IBS, is evidenced in both cases: this was to be expected, in agreement with earlier experimental observations at the Heidelberg TSR [78].

In conclusion, simulations of the beam evolution using a PIC scheme and/or numerical integration of (7.14), validate the perturbative theory on one side, and are able to describe laser cooling for intense ion beams, where space charge and IBS cannot be neglected, on the other side. When no significant resistive impedance acts on the beam, no two-stream instability occurs as the beam undergoes cooling, and a crucial role is played by diffusion due to IBS, which strongly limits the cooling efficiency.
Simulations of laser cooling on bunched beams are planned as future work, with special attention to square-well buckets, which have been proposed to study ordering phenomena in cold ion beams [78]. Using the PATRIC code can significantly help interpret the properties of the Schottky spectrum of such a beam.

Conclusions and outlook

Altogether the measurements carried out at the ESR have greatly helped to gain a far deeper understanding in the dynamics of an intense coasting beam subject to longitudinal instability. The experimental evidence has turned out to be not only a necessary tool to test the validity of the linear theory of the longitudinal instability for a space charge dominated beam below transition energy, but also a most valuable starting point for modeling the beam evolution as it goes nonlinear. Computer simulations have been also proven to be able to reproduce the beam dynamics in a very satisfactory way, and this has confirmed their power of prediction and legitimated their importance in the design of high-current machines and heavy ion fusion drivers. The diagnostics capabilities of beam simulations are essential for the comprehension of the physical content of all phenomena related to the longitudinal instability, since they allow the knowledge of the detail of the beam phase space distribution at each step during an unstable evolution driven under perfectly controlled conditions.

Within this PhD thesis the RF-cavity driven longitudinal instability excited at the ESR has been described and interpreted in detail. For this purpose, the perturbative theory of longitudinal instabilities has been revised, and further on a fluid model has been developed and applied in order to explain some early nonlinear phenomena occurring in the unstable dynamics.
The longitudinal beam signal in the ESR was monitored over 1 s after having tuned the RF-cavity close to the beam revolution frequency. In this way the coupling impedance acting on the beam could be varied within a span of controlled values. It was possible then to reconstruct the resulting self-induced beam modulation signals with a very high time resolution in the off-line analysis. A very good accord has been shown to exist between the theoretical predictions and the recorded signals. A sinusoidal modulation on the beam first harmonic was observed to grow exponentially in the first phase – as the small-amplitude analytical theory predicts – then steepening and saturating, and eventually giving rise to a residual coherent signal on the beam. The shape of these signals agrees with the results from the particle-in-cell simulations with the PATRIC code. The instability showed rise times that, far away from the stability boundary, have been estimated to be smaller than those predicted by the ordinary linear theory. As suggested from the simulations carried out with the particle tracking code, these shorter rise times have turned out to be due to the finite cavity gap voltage needed for the eigenfrequency regulation system. The problem of the off-frequency voltage oscillating in the RF-cavity, which in certain conditions can enhance the unstable effect of the cavity alone, has been subsequently also analytically approached: the modulation of the phase space structure of the beam induced by the external voltage has been demonstrated, and the loss of Landau damping due to this structure, as the amplitude of the modulation grows much bigger than the beam velocity spread (i.e., for very low values of the cavity detuning), has been suggested as possible

mechanism that may lead to a quicker instability.
The nonlinear evolution of a longitudinal instability is of interest, too, because:

- there is no beam loss on one side, and thus the conditions under which the longitudinal instability saturates and eventually leads the beam to a different dynamical equilibrium can be used for diagnostics purposes (e.g., to extrapolate beam parameters like the momentum spread, or the longitudinal coupling impedance seen by the beam) as well as for predicting whether the requirements on the beam quality can be still met in spite of the unstable motion, or the instability must be by all means avoided.

- on the other side, the physics of the nonlinear evolution is connected to a great variety of plasma phenomena that can be uniquely observed and studied in detail under these special conditions.

We have shown in this work that the theoretical analysis of the unstable evolution based on the fluid model explains and predicts the beam dynamics - the more successfully, the farther we are from the stability boundary - not only in the linear phase of the evolution (by adding a corrective term to the space charge impedance taking into account the effects of the longitudinal kinetic pressure), but also when the unstable mode amplitude has grown so large that strong nonlinear effects appear. The role of space charge and of the nonlinear convective terms in the formation of steepening has been recognized to be fundamental. Steepening is due to the resonant generation of higher order harmonics, that is, of shorter wavelength harmonics. The fundamental harmonic drives higher order harmonics through the nonlinear convective terms. Since the dispersion relation with a purely capacitive impedance is linear, the higher order harmonics as well as the fundamental one are characteristic modes of the system and, hence, constantly resonant with the driving fundamental mode: thus, the harmonic amplitudes grow in time. When kinetic effects are taken into account, higher order harmonics go off resonance at some point, their growth saturates and a wave with a sharp descent forms. The importance of space charge in the steepening phenomenon has been also pointed out by simulating the evolution of a beam in which the space charge impedance had been substituted by a reactive impedance concentrated on one single harmonic number: no wave steepening was observed throughout over 1 sec simulation time and besides, no saturation in the momentum spread growth occurred, as the overshoot theory would have predicted. When the cavity is tuned close to the beam revolution frequency, the machine impedance for the fundamental mode is not purely capacitive anymore, but it has a non-vanishing real part. For higher order modes the machine impedance stays almost purely capacitive because the cavity has a narrow band impedance and the space charge is intense. The dispersion relation is almost linear with respect to the longitudinal mode number, and as a consequence, the resistive part of the impedance drives the exponential growth of the fundamental mode, whereas the convective terms drive the growth of higher harmonics through the resonant wave-wave process. The instability driven by the resistive part of the impedance produces perturbations in the line charge density so intense that steepening appears after few e-folding times. Nonlinear saturation of the instability growth occurs because most of the particles end up trapped in the potential well of the wave; hence, this phenomenon (wave-particle) cannot be predicted starting from a fluid description of the beam evolution.
Subsequently, the influence of electron cooling and laser cooling on the beam stability have been considered. For an electron cooled beam such that the electron cooling time is far bigger than the growth time of an expected instability, it has been shown that the

electron cooling does not significantly affect the linear phase of the instability evolution, but instead becomes fundamental in the understanding of the following stages. The momentum spread saturates at a level which is even below the Keil-Schnell threshold, and a strongly coherent structure remains on the beam – similarly to what was observed in the ESR measurements, where the beam was kept electron cooled throughout the instability development – not showing any relaxation towards a situation where possible impedance effects are kinetically suppressed. The situation of a laser cooled beam is addressed differently, because there most concerns come from the deformation of the beam's longitudinal distribution function induced by the process and its possible causing a high-current beam to go unstable. With the aid of a Fokker-Planck modified equation to take into account the laser cooling force, we have found out that kinetic effects arise to stabilize the beam as its two-stream structure would make it more sensitive to high space charge impedances. Beam simulations have also given as a result that a very intense beam that undergoes laser cooling is not subject to two-stream instabilities before the end of the cooling process. In this case, it is intra-beam scattering that mostly limits the performance of the cooling.

Many extensions of the present work are possible as future challenges. Still dealing with coasting beams, the effects of the broad band impedance in producing microwave instabilities can be considered as next step. This requires the implementation in the beam simulation codes of the beam interaction with very high frequency impedances having bands which stretch out on many harmonics of the beam revolution frequency; moreover, it triggers the search for new analytical models that might explain the beam evolution in such cases. In particular, as broad band impedances are centered around the cut-off frequency of the beam pipe, where the space charge impedance also drops to zero, it appears that, at least in a well defined frequency interval still below the cut-off, the fluid model can be applied and a solution is likely to be found in the framework of the Korteweg-de Vries equation (known from plasma physics). Microwave instabilities are in any case an issue that needs to be investigated, because beams having a very high phase space density become specially sensitive to them.
Furthermore, the fluid model might be extended so as to take into account electron cooling through a friction term. The main point is to check whether this would be enough to predict the features of the dynamical equilibrium that is reached after a longitudinal instability in an electron cooled coasting beam, or not. Also the identification of possible solitary waves in certain working conditions could be allowed by a fluid description, and the possibility of finding such a solution in proximity of the pipe cut-off frequency seems not to be a long way off the study of the effects of the broad-band impedance about which we have discussed not far above.
The study of the evolution of finite amplitude perturbations can be of help in order to extract information about beam and/or machine parameters. The rate of the nonlinear Landau damping, as well as its saturating at a finite value, can both be used for this purpose. Actually, an ESR beam time dedicated to this question is foreseen in the next future. Different scopes of these new measurements are planned to be an investigation on the phase space dilution due to longitudinal instability (there would be tried to get information about the evolution of the momentum spread by making use of the integrated Schottky spectrum around a harmonic which is a long way apart from the the unstable one) and measurement of the longitudinal diffusion constant due to intra-beam scattering.

Concerning bunched beams, work has to be done to study space charge effects when laser cooling is applied, and to correctly interpret the Schottky spectra of beams confined in square-well buckets. This is because recently square-well buckets have been proposed to study ordering phenomena in cold ion beams. Both analytical work and PATRIC simulations can be utilized for the Schottky analysis on laser cooled bunched beams. It is highly desirable to get a better understanding of these spectra, since they are the physical observables of which we dispose, and much information is likely to be contained therein. New beam measurements are planned to take place at the Heidelberg TSR (in the Max Planck Institut) in order to investigate the issues of laser cooling applied to high-current bunched beams. In view of that, efforts are presently being put on adequately modeling the process in all its aspects. Preliminary work with this regard has been already presented in Chapter 7 of this thesis, but a comparison with experimental data becomes now indispensable to confirm these theoretical results and stimulate new developments.

Sintesi del lavoro e dei risultati

La fattibilità di strutture in grado di realizzare la fusione nucleare a confinamento inerziale tramite bombardamento indiretto del target con ioni pesanti è strettamente connessa a monte con la progettazione di macchine acceleratrici e guidanti (per fasci di ioni) estremamente complicate e con requisiti molto stringenti sulle modalità di funzionamento. Nell'ambito di tale studio di fisica realizzabilità, l'approfondimento di molteplici aspetti di dinamica del fascio in strutture acceleranti e guidanti diventa necessario per poter essere in grado di depositare sul target la potenza richiesta per innescare l'ignizione. Allo scopo di minimizzare il numero di canali in cui i fasci di ioni vengono preventivamente portati al livello di energia necessario perché possano poi essere convogliati sul pellet, un requisito generale per i drivers finalizzati alla fusione inerziale è che ciascun canale sia in grado di trasportare con perdite minime (sia di fascio che di qualità di fascio, affinché la focalizzazione sul pellet possa avvenire nel rispetto dei parametri) fasci di ioni ad alta densità nello spazio delle fasi. Il raggiungimento di densità molto spinte è però teoricamente limitato da effetti di carica spaziale, i quali inevitabilmente, se trascurati nella fase di progettazione, portano a perdite di particelle o degradazione della qualità del fascio. Un'analisi accurata di tali effetti si affronta generalmente distinguendo i problemi che nascono dal moto trasverso degli ioni nel fascio (tune shift indotto da carica spaziale, instabilità coerenti di fascio di tipo dipolare o multipolare, etc.), e quelli che sono invece associati al moto longitudinale (instabilità coerenti longitudinali, interazione fascio-cavità, effetti del cooling etc.). In particolare, le instabilità coerenti di fascio, trasverse e longitudinali, sono l'indesiderata conseguenza delle interazioni fra particelle appartenenti ad un medesimo fascio, e delle stesse con i campi elettromagnetici indotti dal passaggio del fascio nelle strutture circostanti.
Ciò premesso, si comprende dunque che l'interesse verso le instabilità coerenti si coniuga naturalmente con le tematiche classiche di studio del Dipartimento d'Ingegneria Elettrica dell'Università "Federico II" di Napoli, in quanto legato da un lato al progetto HIDIF per la formazione di un gruppo di studio Europeo sulla fusione inerziale come motivazione di base, e consistente dall'altro nel dover affrontare una serie di problematiche non lineari su sistemi elettromagnetici complessi in cui campi e sorgenti di campo sono continuamente soggetti a mutua azione.
Il contributo dato alla comprensione e all'interpretazione di questo tipo di fenomenologie si è sviluppato in maniera naturale dall'impiego delle già note teorie perturbative lineari per studiare le proprietà di stabilità di un fascio nell'anello di accumulazione presente al GSI-Darmstadt (ESR, Experimentier-SpeicherRing) fino alla realizzazione di misure per dimostrare la validità delle prevalutazioni teoriche e alla modellizzazione teorica di dinamiche instabili o di fasci di ioni in condizioni particolari di funzionamento (per es., sotto l'effetto del laser cooling). La rivisitazione della teoria delle instabilità coerenti di fascio ha infatti consentito la determinazione dei parametri richiesti per indurre un'instabilità longitudinale su un fascio nell'ESR e raccogliere così dati sperimentali sull'evoluzione lineare e non lineare di tale fascio. L'esperimento suddetto è stato realizzato nel Febbraio

1997 e le osservazioni sono state pienamente all'altezza delle aspettative. I dati raccolti con tali misure hanno poi fornito lo stimolo per una più adeguata descrizione del fenomeno in modo da poter prevedere anche parte dell'evoluzione non lineare. Nel seguito, misure ed interpretazione delle misure saranno spiegate in maggiore dettaglio in quanto materiale su cui verte l'intero contenuto della tesi di dottorato.

Le instabilità longitudinali di fasci continui orbitanti in macchine circolari si manifestano come un processo di self-bunching che può essere facilmente rilevato per mezzo di una misura ed un monitoraggio continuo lungo un opportuno intervallo temporale della modulazione della corrente di fascio. Tale corrente, avente inizialmente la caratteristica di corrente continua a parte il rumore Schottky dovuto alla sua effettiva natura discreta, diventa poi sinuosoidale con ampiezza esponenzialmente crescente per un certo intervallo di tempo (con un periodo spaziale che è proprio un sottomultiplo della circonferenza dell'anello, in dipendenza del numero armonico su cui l'instabilità si sviluppa), fino a saturarsi infine, e a manifestare peculiarità nell'evoluzione quali la formazione di un'onda d'urto o la presenza permanente di un'oscillazione residua anche dopo che il processo instabile è giunto a saturazione. I tempi di salita dell'instabilità previsti dalla teoria lineare basata sullo sviluppo perturbativo dell'equazione di Vlasov sono stati valutati per diverse condizioni di funzionamento e messi a confronto con quelli estrapolati dai dati sperimentali rilevati nelle stesse condizioni. L'accordo trovato tra teoria lineare ed esperimento è stato molto soddisfacente, e leggere discrepanze osservate in corrispondenza di alcuni punti di misura sono state ampiamente giustificate a causa della presenza di un campo elettrico esterno in cavità necessario per il sistema di regolazione della frequenza di risonanza – il cui effetto non è considerato invece nella teoria. In effetti, simulazioni mirate al calcolatore eseguite col codice a macro-particelle PATRIC sono state utilizzate per introdurre tale campo esterno, e mostrare come il suo effetto sui tempi di salita delle instabilità potesse proprio riprodurre le osservazioni sperimentali. Il problema di un campo esterno in cavità è stato anche separatamente affrontato dal punto di vista teorico: la dinamica osservata con le simulazioni è stata riprodotta, mentre una perdita di Landau damping dovuta al nuovo tipo di distribuzione nello spazio delle fasi è emersa come ragione più plausibile per giustificare la riduzione dei tempi di salita dell'instabilità quando la cavità era quasi perfettamente accordata. In seguito, l'osservazione della formazione di un fronte d'urto nella fase successiva a quella di crescita esponenziale dell'onda di corrente (osservazione fatta sia direttamente nelle misure che nelle simulazioni PATRIC) ha stimolato la ricerca di una spiegazione del fenomeno basata sull'impiego di un modello fluido comprensivo dei termini non lineari convettivi, e chiuso con l'ipotesi di processo adiabatico (flusso di calore nullo). La risoluzione numerica delle equazioni di tale modello ha riprodotto fedelmente l'evoluzione della corrente di fascio sia nella fase lineare che nel successivo svilupparsi di una marcato "wave steepening". Altre fenomenologie associate alla tarda fase di instabilità – gli effetti di carica spaziale e dell'electron-cooling di fascio sulla saturazione dell'onda instabile o la dinamica sul lungo periodo dell'allargamento dello spread in velocità – sono state studiate usando un integratore numerico dell'equazione di Fokker-Planck, che possiede l'indiscusso vantaggio di un minore rumore grazie all'assenza della granularità che caratterizza invece un codice a macro-particelle come il PATRIC. Come si è evidanziato da tale analisi, l'overshoot previsto per la crescita del momentum spread è seriamente limitato dal cooling, e non ha luogo se c'è una rilevante carica spaziale.

L'ultima parte di questo lavoro di dottorato riguarda l'effetto della tecnica del laser cooling su opportuni fasci di ioni con un elevato numero di particelle. Prendendo spunto dagli esperimenti svolti al TSR di Heidelberg negli ultimi 5 anni, l'effetto di un laser sulla dinamica longitudinale di un fascio è stato prima di tutto studiato in generale dal punto di vista di modellizzazione teorica, e poi introdotto nei codici correntemente usati per la simulazione di fasci (PATRIC e Fokker-Planck solver). Il risultato è che con questi mezzi, molte informazioni si possono ricavare circa il laser cooling di fasci molto intensi, poiché in essi la dinamica del cooling è per la prima volta affiancata all'azione dei campi autogenerati. In questo modo si è certi di non finire per trascurare effetti che potrebbero rivelarsi dominanti quando si considerano fasci molto intensi sottoposti a raffreddamento laser. L'analisi contenuta in questa tesi mostra che le Instabilità di tipo "two-stream", che si sarebbero potute aspettare come conseguenza della deformazione cui è soggetta la funzione di distribuzione del fascio quando il raffreddamento laser è applicato, sono invece bilanciate dall'azione cinetica del laser stesso come si evidenzia dai diagrammi di stabilità corretti. Fasci intensi possono verosimilmente essere raffreddati mediante uso di un laser opportuno, e l'unico fattore che diventa determinante nel limitare le prestazioni dell'operazione è la diffusione indotta da intra-beam scattering.

List of Figures

Bibliography

[1] *Heavy Ion Ignition Facility* Proposal for a European Study Group, GSI-95-03, Report ISSN 0171-4546 (1995).

[2] I. Hofmann, Fus. Engin. and Design **33**, 32 (1996).

[3] R. Bock, Proceedings EPS Conference on Large Facilities in Physics, Lausanne, Sept. 12-14, 1994, (1995), p.348.

[4] I. Hofmann and G. Plass *Overview of the HIDIF Scenario* HIDIF Report 1998, GSI-98-06 (1998).

[5] L. J. Laslett, V. K. Neil and A. M. Sessler, Rev. Sci. Instrum. **32**, 276 (1961).

[6] A. G. Ruggiero and V. G. Vaccaro, CERN Report No. CERN-ISR-TH/68-33 (1968).

[7] L. Palumbo, V. G. Vaccaro and M. Zobov, in **CAS**, *Cern Accelerator School: Fifth Advanced Accelerator Physics Course*, edited by S. Turner (CERN, Geneve, 1995) p. 331.

[8] B. Zotter and P. Bramham, IEEE Trans. Nucl. Sci. **NS-20**, 830 (1973).

[9] J. E. Keil and E. Messerschmid, Nucl. Instrum. Methods Phys. Res. **128**, 203 (1975).

[10] R. L. Martin, I. S. K. Gardner, C. W. Planner and G. H. Rees, Nucl. Instr. Methods Phys. Res. A **278**, 151 (1989).

[11] I. Hofmann, Proc. 1991 Part. Acc. Confer. (PAC), San Francisco, (1991) p. 2492.

[12] J. G. Wang, H. Suk and M. Reiser, Phys. Rev. Lett. **79**, 1042 (1997).

[13] G. Kraft, *First Patient Treatment with Heavy Ions at GSI*, Proc. 6^{th} Europ. Part. Acc. Conf. (EPAC), Stockholm, (1998), p. 212.

[14] H. Geissel *et al.*, Nucl. Instr. Methods Phys. Res. B **70**, 286 (1992).

[15] K. Blasche and B. Franzke, *Status Report on SIS-ESR*, Proc. 6^{th} Europ. Part. Acc. Conference (EPAC), London, (World Scientific, Singapore, 1994), p. 133.

[16] B. Franzke, Nucl. Instr. Methods Phys. Res. B 24/25, 18 (1987).

[17] B. Franzke *et al.*, *Heavy ion beam accumulation, cooling and experiments at the ESR* in Proc. 1993 Part. Acc. Conf. (PAC), Washington D.C., (IEEE, Piscataway, NY, 1993) p. 1465.

[18] B. Schlitt, *Schottky Mass Spectrometry at the Heavy Ion Storage Ring ESR*, Dissertation GSI-97-01, September 1997.

[19] N. Angert *et al.*, *Electron Cooling on the ESR at GSI* in Proc. Europ. Part. Acc. Conf. (EPAC), Rome, ed. S. Tazzari (World Scientific, Singapore, 1988), p. 1436.

[20] F. Nolden, *Zur stochastischen Vorkühlung am ESR*, PhD Thesis, Technische Universität München, 1996.

[21] F. Bosch and B. Schlitt, Phys. Bl. **53**, 27 (1997).

[22] A. Gruber, W. Bourgeois, B. Franzke, A Kritzer and C. Treffert, Nucl. Instr. Methods. Phys. Res. A **282**, 87 (1989).

[23] Uwe Schaaf, *Schottky-Diagnose und BTF-Messungen an gekühlten Strahlen im Schwerionen-Speicherring ESR*, Dissertation Universität Frankfurt, GSI **91–22** (GSI Darmstadt, 1991).

[24] I. Hofmann, Nucl. Instr. Methods Phys. Res. A **278**, 271 (1988).

[25] B. Y. Sharkov *et al.*, Nucl. Instr. Methods Phys. Res. A **415**, 21 (1998).

[26] R. Bangerter, Nuovo Cimento **106 A**, 1445 (1993).

[27] I. Hofmann, R. C. Bär, O. Boine-Frankenhein and G. Rumolo, in Proceedings of the *Workshop on Space Charge Physics in High Intensity Hadron Rings*, Shelter Island, N. Y., 1998, edited by A. U. Luccio and W. T. Weng (AIP, New York, 1998), p. 15.

[28] I. Hofmann, *Inertial Fusion with Heavy Ions*, Advances of Accelerator Physics in Technologies, H. Schopper, ed., World Scientific Publishing Co.

[29] G. Rumolo, I. Hofmann, G. Miano and U. Oeftiger, Nucl. Instrum. Methods Phys. Res. A **415**, 411, (1998).

[30] G. Rumolo, U. Oeftiger, I. Hofmann, R. C. Bär, K. Beckert and M. Steck, Nucl. Instrum. Methods Phys. Res. A **415**, 363, (1998).

[31] M. Reiser, *Theory and design of charged particle beams*, (John Wiley & Sons, New York, 1994).

[32] S. Chattopadhyay, *Some Fundamental Aspects Of Fluctuations and Coherence in Charged Particle Beams in Storage Rings*, CERN **84**–11 (1984)

[33] J. Borer, *Information from the Beam Response to a Longitudinal and Transverse Excitation*, IEEE, Vol. NS-26, No. 3, June 1979.

[34] D. Boussard, *Schottky Noise and Beam Transfer Function Diagnostics*, CERN Accelerator School, Advanced Accelerator Physics Course Proceedings, CERN **95–06** (1995)

[35] G. Kalisch, *Erzeugung und Untersuchung gepulster Schwerionen-Strahlen höchster Phasenraumdichte im Experimentier-Speicherring der GSI*, Thesis Darmastadt, GSI-94-05, January 1994, ISSN 0171-4546.

[36] U. Oeftiger, *Measurement of beam properties and beam environment in LEAR and COSY using RF excitation methods*, Thesis Jülich, Jül-2977, October 1994, ISSN 0944-2952.

[37] J.-L. Laclare *Coasting beam longitudinal and transverse coherent instabilities*, Proc. CAS, General Accelerator Physics, Vol. 1. CERN **94**-01 (1994).

[38] G. Rumolo, *Theory of trnasverse instabilities of coasting beams in accelerator rings. Applications to the SIS* GSI-Interner Bericht, GSI-HSB-98-1, February 1998.

[39] L.D. Landau, J. Phys. USSR **10**, 25 (1946)

[40] H. Wollnik, Nucl. Instrum. Methods Phys. Res., B **26**, 267 (1987).

[41] L. D. Landau and E. M. Lifsits, *Fisica cinetica*, Editori riuniti Edizioni Mir, 1984.

[42] N. A. Krall and A. W. Trivelpiece, *Principles of plasma physics*, San Francisco Press, Inc. 1986.

[43] E. Keil and W. Schnell, *Concerning Longitudinal Stability in the ISR*, CERN ISR 69-48 (TH-RF), 1969.

[44] E. Conte, *Teoria dei segnali*, Notes from the lectures, 1993.

[45] M. Steck *et al.*, *Performance of the ESR Electron Cooling System*, GSI Scientific report, 1991.

[46] S. Cocher and I. Hofmann, Part. Accel. **34**, 1990.

[47] U. Blell, to be published in the Proceedings of the Particle Accelerator Conference, May 12-16 1997, Vancouver, Canada.

[48] I. Hofmann, Z. Naturforsch. **87a**, 939 (1982).

[49] I. Hofmann and I. Bozsik, *Multi-Dimensional Computer Simulation of Intense Beams*, Proceedings of the Symposium on Accelerator Aspects of Heavy Ion Fusion, Darmstadt, March 29 - April 2 1982, GSI-82-8.

[50] R. W. Hockney and J. W. Eastwood, *Computer Simulation Using Particles* IOP Publishing Ltd 1988.

[51] C.K. Birdsall, A.B. Langdon, *Plasma Physics via Computer Simulation*, Institute of Physics Publishing, Bristol and Philadelphia, 1991.

[52] U. Schumann and R. Sweet, *A Direct Method for the Solution of Poisson's Equation with Neumann Boundary Conditions on a Staggered Grid of Arbitrary Size*, Computational Physics Vol. 20, Feb. 1976.

[53] A. Hofmann, *Beam Instabilities*, Proceedings of the 5th Advanced Accelerator Physics Course, Edited by S. Turner, Vol. 1, 1995.

[54] S. M. Lund and R. C. Davidson, Phys. Plasmas **5**, 3028 (1998).

[55] H. Wiedemann, *Particle Accelerator Physics II*, (Springer, 1995).

[56] J. Bisognano, in Proceedings of *EPAC 96*, Sitges, (Barcelona), 1996, edited by S. Meyers *et al.*, Vol. 1, (Institute of Phyisics Publishing, Bristol and Philadelhia, 1996) p. 328.

[57] G. B. Whitham, *Linear and nonlinear waves*, (John Wiley & Sons, New York, 1974).

[58] A. A. Galeev and R. S. Sagdeev, *Nonlinear plasma theory in Reviews of Plasma Physics* edited by Acad. M. A. Leontovich, (New York: Consultants Bureau, 1979), Vol 7.

[59] V. L. Galinsky, V.I. Shevchenko, S. K. Ride and M. Baine, J. Geophys. Res., **102**, 22365, (1997).

[60] O. Boine-Frankenheim, I. Hofmann and G. Rumolo, Phys. Rev. Lett. **82**, 3256 (1999).

[61] J. Bisognano, I. Haber, L. Smith, and A. Sterlieb, IEEE Trans. Nucl. Sci., **NS-28**, 2512, (1981).

[62] G. Rumolo, O. Boine-Frankenheim, I. Hofmann, and G. Miano, *Theory and simulations of intense laser cooled coasting beams*, accepted for publication in Nucl. Instr. Methods Phys. Res. A, (1999).

[63] R. C. Davidson, *Methods in Nonlinear Plasma Theory* (Academic Press, New York, 1972.

[64] T. H. Stix, *Waves in Plasmas* AIP Press, Springer-Verlag New York, Inc. 1992.

[65] P. W. Rambo and R. J. Procassini, Phys. Plasmas **2**, 3130 (1995).

[66] O. Boine-Frankenheim and J. D'Avanzo, Phys. Plasmas **3**, 792 (1996).

[67] S. G. Chen and G. Knorr, J. Comput. Phys. **22**, 330 (1976).

[68] I. B. Bernstein *et al*, Phys. Rev. **108**, 546 (1957).

[69] G. Manfredi, Phys. Rev. Lett. **79**, 2815 (1997).

[70] H. Schamel, Phys. Rev. Lett. **79**, 2811 (1997).

[71] Y. Chin and K. Yokoya, Phys. Rev. D **28**, 2141 (1983).

[72] S. Bogacz and K.-Y. Ng, Phys. Rev. D **36**, 1538 (1987).

[73] J. S. Hangst *et al.*, Phys. Rev. Lett. **67**, 1238 (1991).

[74] W. Petrich *et al.*, Phys. Rev. A **48**, 2127 (1993).

[75] H. Okamoto, A. M. Sessler, and D. Moehl, Phys. Rev. Lett. **72**, 3977 (1994).

[76] H. Okamoto, Phys. Rev. E **50**, 4982 (1994).

[77] S. N. Atutov *et al.*, Phys. Rev. Lett. **80**, 2129 (1998).

[78] M. Weidemüller *et al*, in Proc. Int. Conf. on *Trapped Charged Particles and Fundamental Physics, Monterey, CA/USA, 1998*, edited by D. Dubin and D. Schneider (AIP Conf. Proc. 457, 1999) p. 194.

Acknowledgements

In first place, I would like to thank the persons that gave me the unique opportunity to do this PhD work: Profs. Giovanni Miano and Vittorio G. Vaccaro from Napoli, and Prof. Dr. Ingo Hofmann from GSI. My Italian Professor Giovanni Miano patiently guided my first steps into plasma physics and beam physics, and he has been an excellent supervisor, giving me support, encouragement and help every time I needed throughout my whole PhD time. Prof. Vittorio G. Vaccaro estabilished the contact to GSI and has been constantly interested in the progresses of my work and in my future plans. Prof. Ingo Hofmann kindly accepted me in his group in GSI, and did his best to get me integrated in the group's activity: discussions with him have always been fruitful for subsequent work and developments.
Then I would like to thank my colleague Dr. Oliver Boine-Frankenheim, who has largely contributed to deepen my understanding of nonlinear phenomena in unstable beams and has been following closely my work on laser cooling of high-current ion beams.
A very special place in my thanksgivings I have to reserve for my former colleague Dr. Uwe Oeftiger, who has indeed a significant part in this work as promoter and "leader" of the ESR measurements on longitudinal instabilities: hereby I want to express my unconditional gratitude to him, because he was among the colleagues my reference point, available and helpful especially as I was becoming familiar with the GSI environment and with my subject of study. Beside that, he still remains up to now a very close and understanding friend.
For the numerous advises and consultations especially connected with software problems, LaTeX and Linux questions as well as C-programming for convenient data analysis, I also would like to thank Dr. Ralph Bär. His friendship and support have been of great value in this period.
For the friendly environment and for their help and explanations I would like to thank all the other members of the High Current Beam Physics group: Phys. Lorenzo Bongini, Dr. Giuliano Franchetti, Dr. Rainer Hasse, Dr. R. W. Müller, Dr. Peter Spiller.
Of course, for the time I spent in the University of Napoli, I also would like to thank the whole *Dipartimento di Ingegneria Elettrica* for the availability in the discussions, the cooperation and the pleasant atmosphere, and in particular: Dr. Massimiliano de Magistris, Ing. Antonio Maffucci, Dr. Lorenza Corti, Dr. Ciro Visone, Ing. Daniele Davino, Prof. Luciano De Menna, Prof. Luigi Verolino, and Dr. Claudio Serpico.
Dipartimento di Scienze Fisiche dell'Universitá "Federico II" di Napoli and *INFN, Sezione di Napoli* partially sustained the first part of my stay at the GSI laboratories, and therefore I am very grateful to them, because they allowed me to undertake this project.
In the field of free time and inter-cultural exchanges, I would like to thank all my friends and all the interesting people that I have been lucky to meet during the period of my stay in Germany. Special thanks I would keep for Britta and Ruxandra, who got me patiently into the secrets of the German and Romanian languages, respectively.
Thanks to Magda for her unconditional support.

Very many thanks to Lars, who had to give up part of his German character to better match my chaotic behavior. But he also managed to influence me to believe in a more "organized" view of life.
Thanks to Spela, Frederic, Oana, Emily and Samit.
My sincere gratefulness and affection go to all my Italian friends, who have stayed such in spite of the distance. Special thanks I owe to Lisa, Antonio and Stefano, who were able to drag me beyond any point I could have come to by myself. Their influence has no doubt greatly contributed to determine many features of my personality.
I finally express my absolute thankfulness to my family, who always supported my choices materially and psychologically. To them and to the deep bond that connects us, the whole of my work is dedicated.